Measurement of the Inclusive Forward-Backward $t\bar{t}$ Production Asymmetry and its Rapidity Dependence $dA_{fb}/d(\Delta y)$

by

Glenn Loyd Strycker

A dissertation submitted in partial fulfillment
of the requirements for the degree of
Doctor of Philosophy
(Physics)
in The University of Michigan
2010

Doctoral Committee:

Professor Dante E. Amidei, Chair
Professor James W. Allen
Professor Ronald G. Larson
Professor Rudolf P. Thun
Assistant Professor Aaron T. Pierce

This work is dedicated to my Grandpa,
Stanley J. Strycker, Ph.D.

Thank you for the example and encouragement you have been
to me throughout my life, especially over these past 7 years.

Acknowledgments

First and foremost, I would like to thank my advisor, Prof. Dante Amidei, without whom I would not be completing my PhD. It is his vision that began this measurement in the Michigan group some years ago, and it is Dan's excitement and enthusiasm that has kept it going strong. Dan is unlike any other advisor or boss for whom I've ever worked. He is always encouraging, knows when to push and when to allow a student to work on his or her own. I cannot be more thankful for his advice, scientific leadership, research intuition, and friendship. Thank you, Dan!

Thanks go to all of the professors on my thesis dissertation committee – Jim Allen, Ron Larson, Rudi Thun, and Aaron Pierce. I truly appreciate you all for taking the time to read my thesis, attempting to understand it, and offering suggestions and corrections.

I also would like to especially thank Tom Schwarz, whose own thesis research and computer code are the basis of my own thesis research. Tom not only did much of the groundwork for this analysis, but also advised and assisted with the current result. Additionally, Tom's leadership as the CDF Top Group convener has been outstanding, and his questions and critiques of this analysis have always been very helpful and made our analysis work better. He has been a great help and also a good friend.

Thank you, Clark, for all of your help and for our friendship! Clark Cully was my roommate for the first two years of graduate school and also was primarily responsible for getting me involved with Dan's CDF research group. Additionally, Clark was my "social coordinator" during grad school and introduced me to many of my early friends. We also spent time playing Halo, which was a nice break from our classwork our first year. Thank you, Clark, for helping make grad school a more enjoyable experience.

I'd like to thank the rest of the Michigan CDF group, Dave Mietlicki, Alexei

Varganov, Tom Wright, Andrew Eppig, and Monica Tecchio, for all of their contributions to this analysis as well as their service work for CDF. I've been so impressed by the quality of these people and their willingness to help. Their expertise with the CDF diskpool systems, Monte Carlo production, triggers, and other service areas certainly helped me with my work. I also enjoyed the fun personalities of everyone, and enjoyed working with all of you!

I could not have done this analysis without the helpful support of Charles Plager, Tom Junk, Kevin Lannon, Hyun Su, Tom Schwarz, and others who have worked on perfecting the CDF top group code package used for event selection, event reconstruction, ntuples, and other "behind-the-scenes" work. These physics conventions and CDF analysis code packages are really based on "generations" of professors, research scientists, post-docs, and graduate students, to all of whom I am deeply indebted.

Thanks to all of my teachers and professors through the years, especially R. Kitson, W. Kitson, Mitch Wayne, Grant Matthews, Ikaros Bigi, and Alejandro Garcia. You helped inspire me to learn physics and pursue advanced studies. I would not have pursued a PhD in physics without your encouragement and dedication to teaching.

Finally, I'd like to thank friends and family who did not have a direct involvement with this research, but did have a direct impact in my life. These wonderful people gave me much needed encouragement and advice all of my life, especially during my graduate studies. Sometimes the best thing was just having someone to listen to my troubles and tell me everything I was going through was normal!

Thank you to my friends at the University of Michigan for their friendship and support, especially Clark Cully, Tim Goodman and Nick Licata, friends in the Physics department, and John MacKay, Dave Constantine, Matt Schwantes, Stephen Crabtree, David Lemmerhirt, Darryl Hondorp, and my other friends at the Michigan chapter of Graduate Christian Fellowship.

Thanks to Jason Slaunwhite, John Paul Chou, Jennifer Gimmell, and all of the friends I've made at Fermilab.

I'd like to thank Todd and Laura Rutledge, who have been very special

friends both at Michigan and in Chicago.

Thank you, Dad and Mom, Paul, Beth, Stan, Grandpa and Grandma Strycker, Grandma Bennett, Uncle Steve and Aunt Sharon, and all of my relatives, for your guidance, encouragement, and support!

Paul and Ben, I just want to tell you both, "Good luck. We're all counting on you." Seriously, though, I wish you the best as you finish your own thesis research projects. Hang in there, you'll graduate soon – look at me, it can actually happen!

I would also like to thank my aunt, Linda Bennett, whose encouragement helped interest me in science at a young age. Over the years, Aunt Linda purchased various science books as gifts for me, one of which was Stephen Hawking's classic, "A Brief History of Time". We also made multiple visits to the Chicago Museum of Science and Industry together when I was a child. These books, trips, and discussions were key in sparking my early interest in physics. Thank you, Aunt Linda!

Thank you everyone – friends, family, and colleagues who have been supportive of my PhD studies. It's been a long 7 years, but I'm finally done!

Table of Contents

List of Tables

Table

List of Figures

Figure

List of Abbreviations

Abbreviation

BSM	Beyond the Standard Model
CDF	Collider Detector at Fermilab
CKM	Cabibbo Kobayashi Maskawa
CERN	European Organization for Nuclear Research
CEM	Central Electromagnetic Calorimeter
CES	Central Electromagnetic Showermax system
CMX	Central Muon Extension Detector
CMP	Central Muon Upgrade Detector
CMU	Central Muon Detector
CMUP	Central Muon Detector and Central Muon Upgrade Detector
COT	Central Outer Tracker
CP	Charge Parity (Symmetry)
CPT	Charge Parity Time (Symmetry)
DAQ	Data AcQuisition system
eV, keV, MeV, GeV, TeV	Metric units of energy in electron-volts
FSR	Final State (Gluon) Radiation
FNAL	Fermi National Accelerator Laboratory (Fermilab)
HEP	High Energy Physics
ISR	Initial State (Gluon) Radiation
JES	Jet Energy Scale
LHC	Large Hadron Collider

Linac . . . . . Linear Accelerator

LO . . . . . Leading Order

MC . . . . . Monte Carlo

MCFM . . . . . Monte Carlo for FeMtobarn processes

MET . . . . . Missing Transverse Energy, $\not\!\!E_T$

MURA . . . . . Midwestern Universities Research Association

NLO . . . . . Next to Leading Order

PDF . . . . . Parton Distribution Function

PE . . . . . Pseudo Experiments

PEM . . . . . Plug Electromagnetic Calorimeter

PES . . . . . Plug Electromagnetic Showermax system

PRL . . . . . Physical Review Letters

QED . . . . . Quantum Electrodynamics

QCD . . . . . Quantum Chromodynamics

QFT . . . . . Quantum Field Theory

RMS . . . . . Root-Mean-Square width

SM . . . . . Standard Model

SVD . . . . . Singular Value Decomposition

Abstract

Measurement of the Inclusive Forward-Backward $t\bar{t}$ Production Asymmetry and its Rapidity Dependence $dA_{fb}/d(\Delta y)$

by

Glenn Loyd Strycker

Chair: Dante E. Amidei

Early measurements of a large forward-background asymmetry at the CDF [1, 2, 3, 4] and DØ [5, 6] experiments at Fermilab have generated much recent interest, but were hampered by large uncertainties. We present here a new measurement of the parton level forward-backward asymmetry of pair-produced top quarks, using a high-statistics sample with much improved precision. We study the rapidity (see Equation 2.1 for a definition), y_{top}, of the top quark production angle with respect to the incoming parton momentum in both the lab and $t\bar{t}$ rest frames. We find the parton-level forward-backward asymmetries to be

$$A_{fb}^{p\bar{p}} = 0.150 \pm 0.050^{stat} \pm 0.024^{syst}$$
$$A_{fb}^{t\bar{t}} = 0.158 \pm 0.072^{stat} \pm 0.024^{syst}$$

These results should be compared with the small $p\bar{p}$ frame charge asymmetry expected in QCD at NLO, $A_{fb} = 0.050 \pm 0.015$ [7, 8, 9, 10]. Additionally, we introduce a measurement of the A_{fb} rapidity dependence $\frac{dA_{fb}}{d(\Delta y)}$. We find this to be

$$A_{fb}^{t\bar{t}}(|\Delta y| < 1.0) = 0.026 \pm 0.104^{stat} \pm 0.012^{syst}$$
$$A_{fb}^{t\bar{t}}(|\Delta y| > 1.0) = 0.611 \pm 0.210^{stat} \pm 0.246^{syst}$$

which we compare with model predictions 0.039 ± 0.006 and 0.123 ± 0.018 for the inner and outer rapidities, respectively.

Chapter 1.

Introduction

"It is the glory of God to conceal a thing;
But the glory of kings is to search out a matter."
— Proverbs 25:2

1.1 Natural Philosophy

Throughout history, man has endeavored to understand the universe around him. At times, these interests have been motivated by our desire to manipulate our surroundings and develop technology, while at other times, the motivation is purely philosophical or even religious, as we attempt to satisfy our basic curiosities. Despite the increasing complexity of modern science compared with the simple science experiments in Galileo's day, these goals and motivations remain the same today. We continue to ask questions regarding our existence and purpose in this Universe because we wish to understand the phenomena we observe, use our knowledge to improve life, and explain the meaning of our existence to ourselves and future generations.

In order to trust that the knowledge we obtain is *true*, natural philosophers began using the scientific method as a paradigm for observing the world and explaining it in an unbiased way. By forming models and hypotheses, recording data, and comparing actual observations with predictions, scientists gain increased confidence that their models used to explain the universe around us are true.

1.2 Early Particle Physics

Physics research has led scientists to form many models in order to simplify their explanations of observed phenomena. One such theory is that all matter is made up of small, fundamental pieces called particles. While several ancient cultures hypothesized this, it was Democritus who in 450 B.C. first called these particles atoms (atomos), which means "uncuttable", or "indivisible" [12]. Little progress was made on these theories until Robert Boyle published a theory in 1661 arguing that matter was made up of atoms, as opposed to the "classical" elements (Earth, Air, Fire, Water). During the 17th-19th century, chemists and other scientists made much progress in this new field of chemistry, with John Dalton proposing in 1803 that matter could be explained in terms of *molecules*, composite particles made up of atoms.

In the late 1800s, several experiments with cathode rays (Johann Wilhelm Hittorf) and radioactivity (Herni Becquerel) led physicists and chemists to believe that atoms alone were not enough to explain all of nature. The modern era of particle physics began in 1896, when J. J. Thomson performed experiments showing that cathode rays were particles (electrons) as opposed to atoms, molecules, or waves[1] [12]. Ernest Rutherford discovered that the radioactivity of certain elements was caused by emitted particles, dubbed *alpha* and *beta*. These particles were later identified as helium nuclei ($^4_2\mathrm{He}^{2+}$) and electrons (e^-), respectively. By 1965, many particles thought to be fundamental were discovered (e, p, n, pions, neutrinos, etc.), so many that scientists began to wonder if a simpler theory existed that could explain these particles as composites of yet smaller pieces.

Many techniques were developed to track the position, charge, and momentum of particles produced by radioactive decay and cosmic rays, and eventually more advanced techniques were developed to accelerate known particles to higher energies in order to study collisions. By colliding beams of energetic particles with fixed targets or opposing beams, physicists were able to discover new particles never before observed. However, these new particles did not fit easily in the known framework at the time. Scientists asked themselves: Why are there so many "fundamental" particles? Why do these particles have particular masses and other properties? And, what are the relationships between

[1] The wave nature of electrons was later discovered in electron diffraction experiments (c. 1929, Davisson, Germer, G. Thompson) – the particle-wave duality of the electron was one of the phenomena leading to the development of quantum mechanics).

different particles? Could it be that the particles in this "particle zoo" were really composites of yet more-fundamental particles?

1.3 Modern Experimental Particle Physics

In order to study sub-atomic particles, physicists developed special techniques for producing beams of particles to probe targets. One of the first techniques involved using radioactive elements as a source of alpha and beta rays (helium nuclei and electrons, respectively), which could be collimated into narrow beams by appropriately placed shielding. The resulting beam could then be aimed and scattered off of a fixed target (typically a thin piece of metallic foil). The resulting interaction products were detected by a florescent material that would flash light when a particle hit – Zinc Sulfide, in the case of Rutherford's experiment. Subsequent particle physics experiments used similar techniques of particle production and detection.

In order to observe the tightly-bound particles in a nucleus or other parent particle, a beam of incoming particles must have a high enough kinetic energy to penetrate into atoms and deeper into their constituent nuclei. Radioactive sources only produce particles up to about ~10 MeV (only ~5 MeV for alpha), so other sources must be used to get higher energies. One possible answer is to use an oscillating electric field (essentially a radio-wave) to accelerate charged particles to high energies. This was done by Ernest Lawrence at U. C. Berkeley, who from 1929-1931 used a 9-inch cyclotron to accelerate a positively-charge hydrogen nucleus (H_2^+) at fixed targets. The cyclotron was limited in energy due to its design, and was only capable of producing a ~1 MeV beam. However, advances in cyclotrons and other similar accelerators (synchrocyclotrons, betatrons, synchrotrons, etc.) now make it possible to generate beam energies at the TeV scale. Chapter 2 will explain how Fermilab's Tevatron accelerator, used for producing the data in this dissertation, accelerates protons and antiprotons to ~1 TeV.

Targets have also advanced greatly since the early days of particle physics. Fixed-target experiments aim the high-energy accelerated particle beam at a stationary target. By conservation of energy and momentum, the sum of the product particles from a collision must move with total momenta sum close to that of the initial beam momentum. However, this means that the center-of-mass of the system (the beam and target) will move with respect to the lab

frame. This results in much of the beam energy "wasted" in the interaction (that is, this kinetic energy is not available for producing new particles). To improve the efficiency of interactions, many experiments now use an opposing beam as the "target". This allows the center-of-momentum frame of the system to be roughly at rest with respect to the lab frame, so the products of the interactions are also produced at kinetic energies closer to rest. However, this improvement in efficiency comes at a cost: beam-on-beam experiments require tightly-focused beams and careful alignment in order to produce collisions. In fact, because these beams have lower densities than solid foil targets, a beam-on-beam experiment will not produce as many collisions as a fixed-target experiment. This results in a lower total "luminosity" for beam-on-beam experiments, but this is considered to be acceptable, given that the interaction energy is higher for such experiments.

Detector technology has seen many improvements since the ZnS detector used by Rutherford. Early improvements began with the cloud chamber (c. 1911) and bubble chambers (c. 1953). These chambers were filled with a low-pressure gas that would ionize as charged particles passed through it, causing visible tracks to appear, which could then be photographed [13]. Wire chambers (c. 1968) incorporate the use of high-voltage wires to produce electric fields within a volume of gas. Charged particles traveling through the chamber ionize the gas, and these ions travel to nearby wires, producing a measurable current. By tracking which wires are "hit", physicists can infer the path of a charged particle. The Central Outer Tracker (COT) at the Collider Detector at Fermilab (CDF) is explained in Section 2.3.3 and is an example of a wire chamber. Silicon microstrip detectors are the most recent improvement for measuring the path of charged particles. The silicon system at CDF is described in Section 2.3.2.

In order to measure the energy and momentum of both charged and neutral particles and photons, experiments additionally use detectors called "calorimeters". These devices use layers of dense material that cause incoming particles or photons to "shower" less energetic charged particles as the fast particle travels through. This showering also slows down the particle, so that after traveling through a certain distance the particle would stop, a process called "attenuation". The dense material is divided into layers, so that by counting the number of layers through which the original particle passed an energy measurement is made. This is done by sandwiching a less-dense layer between

each dense layer of absorbing material. The less-dense layer is chosen to be of a material that samples the intensity of showering particles. In the CDF calorimeters, this material is a semi-transparent piece of scintillating plastic, meaning that it emits light when charged particles pass through it. This light is sent to photomultiplier tubes that detect even small numbers of photons, accurately measuring the response of each scintillating layer. By counting the number of layers that glow in each calorimeter stack, the number of absorbing layers that the original particle passed through is also known, therefore the energy is determined. The calorimetry systems at CDF are explained further in Section 2.3.5.

1.4 The Standard Model

In the mid-1960s, several theories began to develop that together explained almost all known particle physics. Each of these theories used quantum field theory (QFT) to explain specific force interactions between particles. Quantum Electrodynamics (QED) used photons to explain the electromagnetic force between all charged particles. In 1967, Steven Weinberg and Abdus Salam proposed a theory that unified this force with the "weak force", the mechanism responsible for radioactive decay (they later shared the 1979 Nobel Prize in Physics with S. L. Glashow for this theory of electroweak unification). The strong force was then explained by a similar field theory, which was named Quantum Chromodynamics (QCD). Taken together, these theories are called the Standard Model. This model was highly successful at explaining the composition and interactions of the known particles at the time. These theories divide the fundamental particles into several important groups: quarks, leptons, and force-carrying bosons. These fundamental particles and their composites successfully explain the entire particle zoo. Perhaps more importantly, when these theories were developed they predicted the existence of particles that had not yet been observed (such as the top quark) – much like Mendeleev's Periodical Table of the Elements originally had gaps that predicted "new" elements. Verifying the existence of these predicted particles has given much weight to this model. Ultimately, the Standard Model has proved to be one of the most successful models in physics.

A table of the Standard Model particles is seen in Figure 1.1. The leptons are fermions (particles that exhibit spin $\frac{1}{2}$) and the massive leptons (e, μ, τ) have a charge of $\pm\frac{1}{2}$. Muons (μ) and tau (τ) particles basically behave like

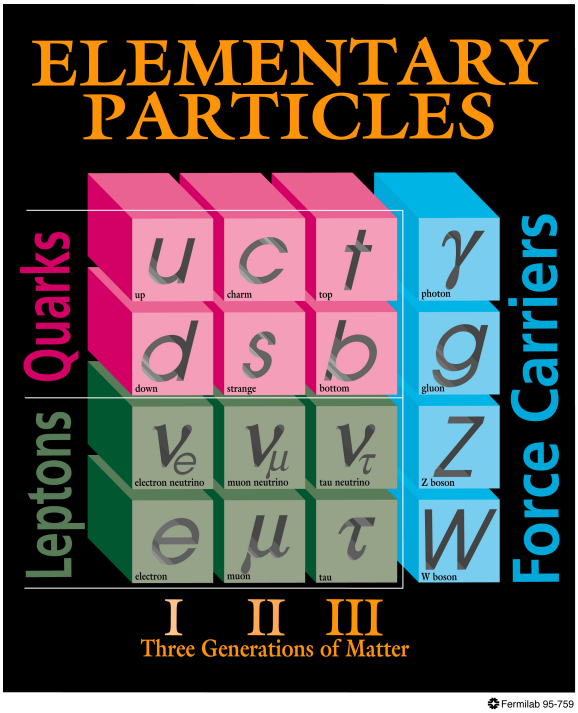

Figure 1.1: The Standard Model Particles (image courtesy of FNAL)

heavier versions of the electron. Much like heavy, radioactive elements in the periodical table, the muon and tau are able to decay via the weak force into the lighter electron. The electron, being the lightest lepton, is stable, so this is what we find "normally" in nature. Muons and taus can be observed in cosmic ray experiments as well as at particle accelerator experiments such as CDF at Fermilab.

For each massive lepton is a corresponding neutrino (ν_e, ν_μ, ν_τ), also in the lepton family. Neutrinos have a very small mass, but no charge. Because they only interact via the weak force, the cross-section of interaction for neutrinos is *very* low. Many neutrinos pass through the Earth each second ($\sim 6\times10^4/\mathrm{m}^2\mathrm{s}$), and only a small fraction interact with matter. Neutrinos can be directly detected by observing their interaction with electrons. Large underground experiments, such as Super-Kamiokande in Japan, use water or another liquid medium as a source of electrons. When a neutrino scatters off of an electron, it sometimes imparts enough energy to knock the electron out of its orbit. This electron has sufficient velocity to produce Cerenkov radiation as it passes through the water in the detector. By measuring this radiation with sensitive photo multipliers, the neutrinos can be inferred. At CDF, DØ, and other par-

ticle collider experiments, neutrinos must be inferred in a collision event by measuring missing momentum. That is, because energy and momentum must be conserved in physics interactions, a neutrino in an event will show up as a missing piece when all of the energies and momenta of the outgoing particles are added up.

Quarks make up composite particles such as protons and neutrons, the constituents of atoms. In general, composite particles made of quarks are known as hadrons. QCD theory postulates that quarks have a charge known as "color", analogous to electric charge but operating in the strong force. Color charge prevents "bare" quarks from existing freely on their own, a property known as "confinement".

In fact, composite particles, such as the proton, have their total momentum distributed among their various "partons", the quarks and gluons that compose protons and neutrons (gluons are spring-like force-carrying particles that hold quarks together, as explained below). Each quark in a proton carries only an average of 1/6 the total momentum *on average*, but at any given instant a quark may have more or less momentum. This means that hadron colliders such as the Tevatron cannot tune the particle collisions perfectly. Each proton/antiproton collision is actually a parton collision – quark/antiquark, gluon/gluon, or some combination of quark/gluon collision. The distribution of interaction energy for parton collisions has an average 1/6 of the proton/antiproton energy $\sqrt{\hat{s}}$. Because one parton may have more momentum than the other parton in the collision, the center-of-mass frame of the interaction may move with respect to the lab frame, the $p\bar{p}$ center-of-mass frame. This is why the $q\bar{q}$ frame is inaccessible to measurement, and why we can only study the $t\bar{t}$ and lab frames. We explain this further in Section 1.8.

Force-carrying bosons constitute the final group of particles in the Standard Model. These include the photon, responsible for light and all electromagnetic radiation, as well as the electromagnetic force; the $W^{\pm}$ and Z bosons, responsible for weak force that is involved in radioactive decays and nuclear processes; the gluon, which mediates the strong force that holds quarks together in hadrons; and the yet to be observed Higgs Boson, which has been predicted in order to explain the rest masses of the other Standard Model particles.

High Energy Particle Physics studies the interaction of all "matter" and

Particle	type	fermion or boson	fundamental or hadron (composite)
u,d,s,c,b,t	quarks	fermion	fundamental
e, μ, τ	leptons	fermion	fundamental
W, Z, γ	forces	boson	fundamental
π	pion	boson	hadron meson ($u\bar{d}$, $d\bar{d} - u\bar{u}$, $d\bar{u}$)
K^0, K^+, K^-	kaon	boson	hadron meson ($d\bar{s}/s\bar{d}$, $u\bar{s}$, $s\bar{u}$)
J/Psi	J/Psi	boson	hadron meson ($c\bar{c}$)
p, n	nucleon	fermion	hadron baryon (uud, udd)

Table 1.1: Short sample of various fundamental and composite particles

"force-carrying" particles. By measuring particle properties (their mass, spin, charge, cross-section, etc.) and comparing experimental data with the Standard Model predictions, physicists find evidence to confirm or challenge the Standard Model. A few questions already exist: why are there exactly 3 "generations" of leptons (e, μ, τ) and quarks (ud, sc, bt)? Why are the masses so different between these generations of particles (the top quark is thousands of times heaver than the up and down quarks). In fact, is there an explanation for the rest mass of any particle? These questions have led theorists to make new models that extend or modify the Standard Model. Theories predicting such new physics are called "Beyond the Standard Model" (BSM). These theories provide physicists with motivation for deciding which particles and properties to investigate. That is, any property that can be measured with precision offers either confirmation of the Standard Model or evidence for BSM theories. The work done in this dissertation is one such test – we measure the forward-backward asymmetry of top quark production and compare with predictions from the Standard Model. Theorists may then use these values to constrain possible parameters of exotic BSM physics models, such as axigluons, which we discuss in Section 1.7.

Table 1.1 shows a summary of the various categories of fundamental and composite particle names, as some particles have multiple distinctions (e.g. all nucleons are fermions, but not all fermions are nucleons). Figure 1.2 shows a diagram connecting each possible Standard Model interaction between particle types. For example, leptons interact with photons (electromagnetic force), and the W and Z bosons (the weak force), but do not interact *directly* with quarks or gluons. Leptons do scatter off quarks, however, because quarks interact with photons and W and Z bosons, too. This leads to the construction of Feynman diagrams, which are schematics of particle physics processes. These diagrams actually represent cross-section calculations, as each branch, loop, and vertex

represents part of an equation summing over all possible incoming and outgoing particle momenta and energy. Calculations of Feynman diagrams are beyond the scope of this dissertation, but we will present various Feynman diagrams throughout this dissertation in order to show various processes.

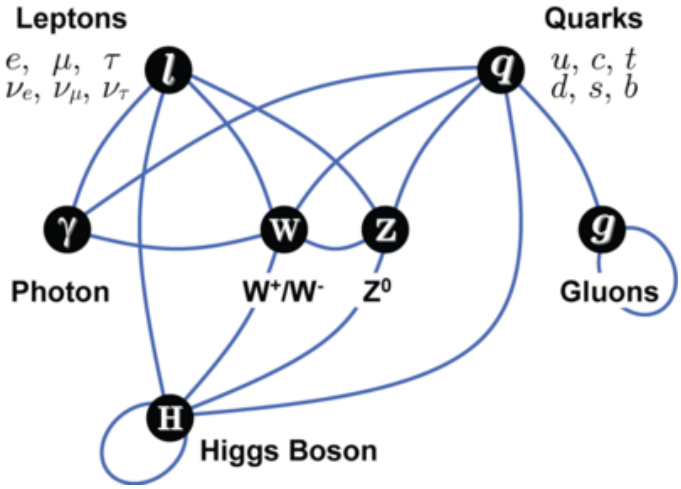

Figure 1.2: Standard Model particle interactions
(Wikimedia Commons public domain image)

1.5 The Top Quark

The top quark is the most recently discovered fundamental SM particle, first observed at CDF in 1995 [14]. Weighing ~$173.3 \pm 1.1 \mathrm{GeV/c^2}$ [19], it is the heaviest of the quarks by a factor of ~40x over the bottom quark mass of 4.20 $\mathrm{GeV/c^2}$, and over 50000x the mass of the up quark (1.5-3.3 $\mathrm{MeV/c^2}$). Figure 1.3 shows the relative masses of the Standard Model quarks. It has roughly the same mass as a tungsten nucleus – however, being a fundamental particle, it is thought to be a "point" particle, having an effective "size" of zero. Because it is more difficult to produce $t\bar{t}$ pairs in accelerator collisions than other products, there are relatively few top events available to study, making the properties of the top quark less well known than other fundamental fermions. Being so massive, the top quark decays at a rate so fast that it does not have time to "hadronize" (form composite hadron particles) before decaying, as the other quarks do. This makes it attractive for studying spin correlations and other previously inaccessible measurements.

At the Tevatron, the majority of top quarks are produced in matter/anti-

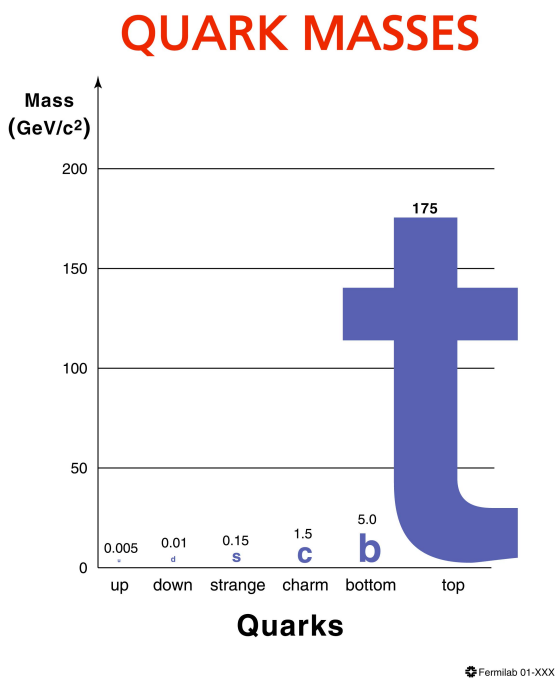

Figure 1.3: The relative quark masses (image courtesy of FNAL)

matter pairs through the process of quark-antiquark annihilation from the proton beam collision. We write this process as $p\bar{p} \rightarrow t\bar{t}$, and it produces roughly 85% of our $t\bar{t}$ events. Because protons and anti-protons are actually composites of quarks and gluons, it is also possible to make $t\bar{t}$ pairs through "gluon-fusion", written as $gg \rightarrow t\bar{t}$. This process accounts for the remaining 15% of $t\bar{t}$ production.

1.6 Top Decays

As explained above, the top quark decays very rapidly – in fact, too quickly to be able to be directly observed. Instead, we must study the decay products of $t\bar{t}$ production and use conservation of energy and momentum to "reconstruct" the original top quark kinematics from the decay product kinematics. This is not an entirely trivial calculation, and we will spend some time in this section and Section 3.2 discussing how this is accomplished.

The top quark usually decays by emitting a $W^{\pm}$ boson to become a b-quark. That is, the particle decays through the process $t \rightarrow W^{+}+b$, and the anti-particle through $\bar{t} \rightarrow W^{-}+\bar{b}$. The b-quark produces a "jet" (a cone of particles) in the detector with a secondary (displaced) vertex, permitting us to "tag" this jet and distinguish it from a light-flavor jet. We explain this tagging

technique in Section 4.2.

$W^{\pm}$ bosons decay in several possible ways, classified as *leptonic* and *hadronic* decays. In leptonic decays, a W particle decays to a lepton and its corresponding neutrino. This can be written as $W \rightarrow l\nu$ in general, or $W \rightarrow e\nu_e$, $W \rightarrow \mu\nu_\mu$, and $W \rightarrow \tau\nu_\tau$ for specifying electrons, muons, or tau leptons as the decay products. For hadronic decays, the W becomes either an up/down pair ($u\bar{d}$ or $\bar{u}d$, depending on the charge of the W) or a charm/strange pair ($c\bar{s}$ or $\bar{c}s$). While charm/strange makes up a fraction of these hadronic decays, it turns out that we can treat these cases as up/down quarks in our event reconstruction (Section 3.2), since they are light quarks and not often "b-tagged" (discussed in Section 2.3.2).

Because we actually study $p\bar{p} \rightarrow t\bar{t}$ events, we have 2 W bosons (W^+ and W^-) that subsequently decay in each event. The possible combinations of W decay naturally classifies our $t\bar{t}$ events into 3 categories, or "decay channels": all-leptonic, all-hadronic, and semi-leptonic. Each channel has advantages and disadvantages for top physics analyses, particularly since each channel has different products used for reconstructing the original $t\bar{t}$ kinematics.

In the all-leptonic decay channel, also called the "dilepton" channel, both W bosons decay leptonically ($t\bar{t} \rightarrow W^+bW^-\bar{b} \rightarrow l^+\nu b l^-\bar{\nu}\bar{b}$). Because all of the hadrons in the decay are b-quarks, all jets in the event should be able to be b-tagged. Also, we have 2 well-measured leptons in the event. These factors result in a high signal-to-noise ratio, since it is harder for background processes to fake events in this channel compared with the other channels we will discuss. However, having two leptonically-decaying W bosons also results in 2 neutrinos in the decay products, making it difficult to reconstruct the original event. That is, since neutrinos cannot be directly observed at CDF, the event is "under-constrained" when we attempt to calculate the original top quark kinematics from the available event information. Additionally, the "branching ratio", the percent of the time that $t\bar{t}$ decays via this channel, is quite low (~12%). Thus, we do not use this channel for our analysis.

In the all-hadronic channel, both W bosons decay to quark-antiquark pairs ($t\bar{t} \rightarrow W^+bW^-\bar{b} \rightarrow u\bar{d}bu\bar{d}b\bar{b}$). This channel has an advantage over the all-leptonic channel in that it has no missing transverse energy (we use the notation $\not\!\!E_T$) from neutrinos. However, there are 6 total jets in the event, only 2 of which

are from b quarks. This makes event reconstruction rather difficult, since there is a high probability a jet will be mis-assigned. Also, because there are many possible ways for QCD events to have 6-jets with 2-tags (mistags), many QCD background events pass the selection cuts and overwhelm the signal, resulting in a low signal-to-background ratio. In order to get enough signal events to be statistically significant from the background, a different channel must be used.

A compromise between the previous channels is to use the semi-leptonic decay channel ($t\bar{t}\rightarrow W^+bW^-\bar{b}\rightarrow l^+\nu b\bar{u}d\bar{b}$ or $u\bar{d}bl^-\nu\bar{b}$). In these events, the W from one of the $t\bar{t}$ pair decays leptonically and the other decays hadronically, resulting in 4 jets (2 b quarks and an $u\bar{d}$ or $\bar{u}d$ pair) and only 1 neutrino. Because there is only one neutrino and not two, the kinematics of the neutrino can be inferred for semi-leptonic $t\bar{t}$ events. As we will discuss in Section 3.2, these events are "completely-reconstructable", meaning that the decay product kinematics over-constrains the fit for assigning jets to partons, which results in accurate inferences for top quark kinematics. See Figure 1.4 for a Feynman diagram of this decay channel. The branching fraction for this channel is also much higher than the dilepton channel, and the signal-to-background ratio is much better than the all-hadronic channel, making semi-leptonic decays the ideal channel for studying top physics. Additionally, because there is exactly 1 lepton whose charge is the same as the leptonically-decaying top or antitop quark, we can easily infer the charge of the top quarks. This is essential for our measurement of the top production asymmetry. All of these qualities lead us to choose to use only the semi-leptonic channel for our analysis.

The three channels, their decay productions, and their relative fraction of $t\bar{t}$ decays are summarized in Table 1.2 below.

Channel Name	Process	Relative Fraction
All-leptonic	$t\bar{t}\rightarrow W^+bW^-\bar{b}\rightarrow l^+\nu bl^-\bar{\nu}\bar{b}$	12%
All-hadronic	$t\bar{t}\rightarrow W^+bW^-\bar{b}\rightarrow u\bar{d}b\bar{u}d\bar{b}$	44%
Semi-leptonic	$t\bar{t}\rightarrow W^+bW^-\bar{b}\rightarrow l^+\nu b\bar{u}d\bar{b}$	44%

Table 1.2: $t\bar{t}$ decay channels

1.7 The Forward-Backward Asymmetry

Top quarks have measurable properties such as mass, charge, and spin, that are interesting, but the geometry of the $p\bar{p}$ collisions at the Tevatron offers

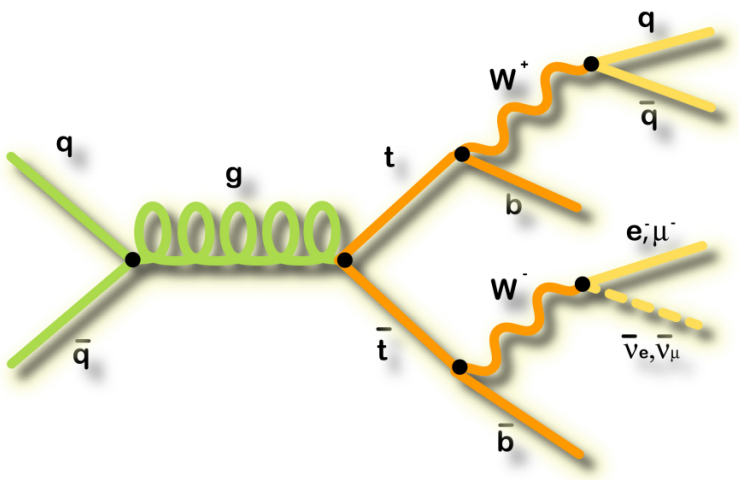

Figure 1.4: Semi-leptonic $t\bar{t}$ Feynman diagram

additional *production* properties for us to measure, such as production angle. This is an important property because it sheds light on the physics processes responsible for producing the top quark, namely the strong force. The Standard Model predicts a certain dependence of top production cross-section as a function of the production angle. Other theories predict a different dependence, as we will discuss in Section 4.3. Thus a careful study of the top quark production angle helps us validate or constrain the Standard Model and other theories.

We choose to measure the angle that the top quark momentum makes with respect to the proton beam direction. In the $t\bar{t}$ rest frame, this angle is called θ^*, and it appears in the following equation for the Leading-Order (LO) $t\bar{t}$ production differential cross section [21] (see Figure 1.5d for the Feynman diagram for this process):

$$\frac{d\sigma^{q\bar{q}\to t\bar{t}}}{d\cos(\hat{\theta})} = \frac{\alpha_s^2}{q^2}(1+\cos^2\theta^*) + (1-\beta^2)\sin^2\theta^* \tag{1.1}$$

In this equation, we see that the distribution of production angles $\cos(\theta^*)$ is completely categorized by measurable quantities. The strong force coupling constant α_s is found through measurements of the total top quark production cross section. q is the interaction energy of the parton collision, which is equal to our reconstructed quantity $M_{t\bar{t}}c^2$. β is the velocity of the top quark in terms of v/c, or using Special Relativity, $\beta = \sqrt{1-4m^2}$, where m is the boosted mass of the top quark $m = m_t/\sqrt{q^2/c^4}$. Note that for light particles, β approaches 1, so the $(1+\cos^2\theta^*)$ term of Equation 1.1 will dominate. Since measurements

of cross section and $M_{t\bar{t}}$ (and also top quark spin) have been made by other analyses, the angular dependence is the obvious measurement to make, which we perform in this dissertation.

For the leading order calculation above, we see that the angular quantity is symmetric – that is, all $\cos(\theta^*)$ and $\sin(\theta^*)$ terms are of even order. However, at Next-to-Leading-Order (NLO) and higher order calculations, QCD predicts odd terms in Equation 1.1. In fact, other theories beyond the Standard Model predict odd terms for the differential cross-section, too, as we will see below when we discuss Axigluons. Therefore, it becomes interesting to measure the distribution of production angles. By counting how many events are produced with a forward-moving top quark ($\cos(\theta^*) > 0$) and comparing to the number moving backwards ($\cos(\theta^*) < 0$), we can measure a possible forward-backward bias in top quark pair-production.

The $t\bar{t}$ forward-backward production asymmetry (abbreviated as A_{fb}) has gained the interest of the theoretical and experimental communities because of recent measured values higher than the Standard Model prediction, at CDF [1, 2, 3, 4] as well as the DØ experiment at Fermilab [5, 6] (see Section 1.10). Naturally, because of symmetry, Leading-Order (LO) QCD predicts the top quark production angle to be completely symmetric with respect to proton beam direction, which would result in $A_{fb} = 0$. However, at Next-to-Leading-Order (NLO), QCD predicts a small charge asymmetry, $A_{fb} = 0.050 \pm 0.015$ [7, 8, 9, 10], due to interference of initial-state radiation diagrams with final-state diagrams (Figure 1.5b and 1.5a) and the "box diagram" with Born processes (fig. 1.5c and 1.5d).

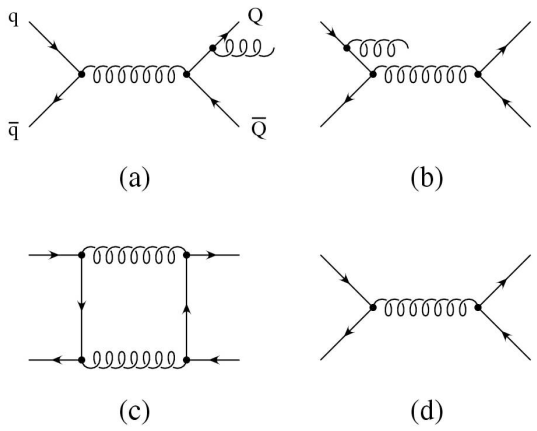

Figure 1.5: NLO and LO Feynman diagrams

New physics models exist that predict even larger possible A_{fb} values. "Axigluons" are involved in several such models. These hypothetical particles behave as gluons, but can interact with quarks axially as well as vectorially. Unlike gluons, axigluons could have a mass. A generic Lagrangian, used in Reference [11], predicts the following differential cross-section:

$$\begin{aligned}\frac{d\sigma^{q\bar{q}\to t\bar{t}}}{d\cos(\hat{\theta})} &= \alpha_s^2\frac{T_F C_F}{N_C}\frac{\pi\beta}{2\hat{s}}\{1+c^2+4m^2 \\ &+ \frac{2\hat{s}(\hat{s}-m_G^2)}{(\hat{s}-m_G^2)^2+m_G^2\Gamma_G^2}[g_V^q g_V^t(1+c^2+4m^2)+2g_A^q g_A^t c] \\ &+ \frac{\hat{s}^2}{(\hat{s}-m_G^2)^2+m_G^2\Gamma_G^2}[((g_V^q)^2+(g_A^q)^2)\times((g_V^t)^2(1+c^2+4m^2) \\ &+ (g_A^t)^2(1+c^2-4m^2))+8g_V^q g_A^q g_V^t g_A^t c]\} \qquad (1.2)\end{aligned}$$

The first term in this equation is the LO prediction, identical to Equation 1.1 above. α_s is the strong force coupling constant. $T_F = 1/2$, $C_F = 4/3$, and $N_C = 3$ are color factors used by Reference [11]. $\hat{s}$ is the interaction energy, m is the (relativistic) mass of the top quark $m = m_t/\sqrt{\hat{s}}$. β is the velocity of the top quark, where $\beta = \sqrt{1-4m^2}$. In this equation, c is a shorthand abbreviation for $\beta\cos(\theta^*)$. The additional terms involve the parameter constants g_V^q, g_V^t, g_A^q, and g_A^t, which are coupling parameters that explain how quarks might additionally couple axially and vectorially to the proposed axigluons. Variables associated with the axigluons include M_G, the mass of the axigluon, and Γ_G, the axigluon width. The first of these extra terms shows the interference between the Standard Model gluon and the axigluon model. The second term is a "pole" term, meaning that the cross-section of interaction will show a resonance as the interaction energy s approaches the axigluon mass m_G^2. Because no such resonance has been observed in the $M_{t\bar{t}}$ spectrum, this term must be small, which constrains possible values for the coupling parameters g_V^q, g_V^t, g_A^q, and g_A^t. Additionally, the cross section for $t\bar{t}$ production is close to that predicted by the Standard Model, so the cross section equation above must have only a small effect on the inclusive integrated cross section. These requirements are explained in Reference [11] and used to constrain the coupling parameter values for axigluons. Choosing different values for these coupling parameters can result in A_{fb} values larger than 0, as shown in Figure 1.6 (reproduced from Reference [11]). Measuring an A_{fb} consistent with the Standard Model would put constraints on the existence of axigluons with this form, or constraints on possible coupling parameters. Thus we see that measuring A_{fb} in data is important for studying both the Standard Model as well

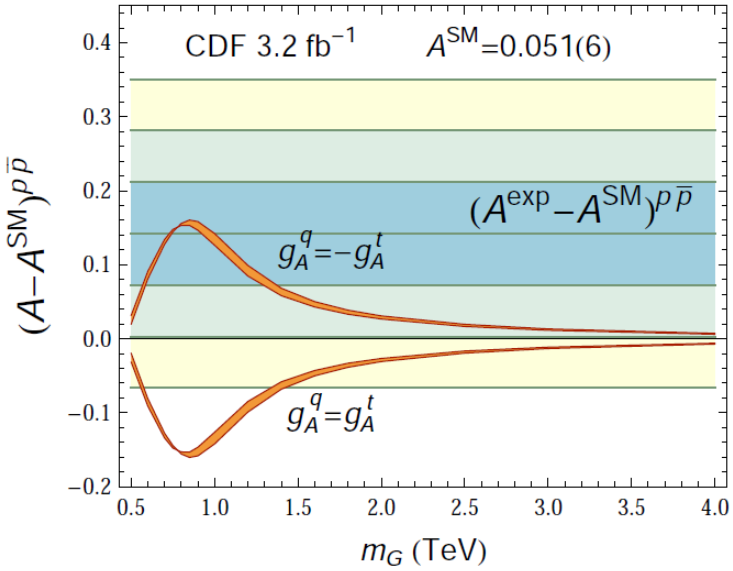

Figure 1.6: Contributions of Axigluons to A_{fb} as a function of the axigluon mass (reproduced from Reference [11])

as BSM theories.

We note that *both* of these extra terms have parts symmetric and anti-symmetric in c, meaning that this model predicts a forward-backward asymmetry for certain values of the coupling parameters. By measuring A_{fb} we can find out how consistent the Standard Model is with our data and compare with this new axigluon model, showing possible phase-space plots for the coupling parameters.

In this dissertation, we present new measurements of the $t\bar{t}$ production asymmetries. We use a dataset with an integrated luminosity of 5.3 fb^{-1}. We study the rapidity, y_t, related to the angle that the momentum of the produced top quark makes with respect to the incoming parton momentum. Additionally, we measure the Lorentz-invariant quantity $q\Delta y$, equivalent to $(y_t - y_{\bar{t}})$, in order to measure the asymmetry in the $t\bar{t}$ rest frame. We subtract backgrounds and perform a model-independent correction for acceptance and reconstruction dilutions in order to find the asymmetry at the parton level. Finally, we introduce a new measurement of the A_{fb} rapidity dependence $\frac{dA_{fb}}{d(\Delta y)}$. We compare all of these measurements with Standard Model predictions.

1.8 Asymmetry Variables

An integral *charge asymmetry* compares the number of top and anti-top quarks produced with momentum in a given direction. Using the rapidities of the quarks, we compare the number of top and antitop quarks produced in the proton direction:

$$\mathrm{A_C} = \frac{N_{\mathrm{t}}(\mathrm{y} > 0) - N_{\bar{\mathrm{t}}}(\mathrm{y} > 0)}{N_{\mathrm{t}}(\mathrm{y} > 0) + N_{\bar{\mathrm{t}}}(\mathrm{y} > 0)} \tag{1.3}$$

where $N_i(j)$ is the number of particle i observed along the direction j ($y > 0$ in this case). A non-zero value A_C implies a net top current in the proton direction.

In contrast, an integral *forward-backward asymmetry* compares the number of top quarks moving along or opposite a given direction. A convenient choice for opposite directions are the proton and anti-proton directions, thus

$$\mathrm{A_{fb}} = \frac{N_{\mathrm{t}}(\mathrm{y} > 0) - N_{\mathrm{t}}(\mathrm{y} < 0)}{N_{\mathrm{t}}(\mathrm{y} > 0) + N_{\mathrm{t}}(\mathrm{y} < 0)} \tag{1.4}$$

where $N_i(j)$ is as described above. If CP invariance is good, $N_{\bar{\mathrm{t}}}(\mathrm{y} > 0) = N_{\mathrm{t}}(\mathrm{y_t} < 0)$ and $\mathrm{A_C} = \mathrm{A_{fb}}$. Since the Tevatron system is CP-invariant, our analysis is built for $\mathrm{A_{fb}}$.

However, our definition of $\mathrm{A_{fb}}$ is not complete until the frame of reference is specified. Because the momenta of the partons in a collision may not have equal magnitudes (due to the parton-distribution-function, as explained in Section 1.4), the $\mathrm{q\bar{q}}$ frame may not be at rest with respect to the $\mathrm{p\bar{p}}$ lab rest frame. The $\mathrm{q\bar{q}}$ frame is hard to observe, since we are limited in measuring the total products of an interaction by the beam pipe and limited size of our detector. This makes the fundamental $\mathrm{q\bar{q}}$ frame inaccessible in both experiment and simulation, leaving only the $\mathrm{t\bar{t}}$ rest frame and $\mathrm{p\bar{p}}$ lab frame open to measurement. We will show in Section 3.2 that it is possible to measure the production angles in both of these frames.

1.8.1 $\mathrm{p\bar{p}}$ Frame

In the lab frame, we look at the angle between the top quark and the proton direction and measure the rapidity $\mathrm{y_t}$. However, because we are using semi-leptonic events for our data sample, top quarks decay leptonically in half of our events and hadronically in the other half. This makes it problematic to use the $\mathrm{y_t}$ distribution, since acceptances are different for $\mathrm{y_{had}}$ and $\mathrm{y_{lep}}$. To control

against this, for the $p\bar{p}$ frame measurement we will measure the rapidity of hadronically-decaying quark y_{had}, whether or not it was a top or anti-top: we know which quark (top or antitop) decayed hadronically by the charge of the lepton in the event, as shown in Table 1.3. This means that y_{had} is either y_t or $-y_{\bar{t}}$. We choose y_{had}, instead of y_{lep}, because the leptonically-decaying side has larger uncertainty due to the presence of a neutrino.

$\mathbf{q_l}$	$\mathbf{t_{lep}}$	$\mathbf{t_{had}}$
$+$	t	$\bar{t}$
$-$	$\bar{t}$	t

Table 1.3: The leptonic and hadronic systems in events with positive and negative leptons

Because top quarks and antitop quarks differ by their charge, a top quark moving forward is equivalent to an antitop quark moving backward. This is obviously true in the $t\bar{t}$ rest frame, since these quarks are produced back-to-back. However, if we assume CP-invariance (see Section 6.1) for the entire $p\bar{p}$ system, the lab-frame distributions are also mirror images of each other. That is, assuming CP-invariance allows us to multiply y_{had} by $-1{\cdot}q_{lepton}$, resulting in $-q{\cdot}y_{had} = y_t$, as can be seen in Table 1.3 above. This gives us an *equivalent top rapidity*. We use $-q_{lepton}$ so that a net top current in the proton direction will produce a positive asymmetry. We see that Equation 1.4 now becomes

$$A_{fb}^{p\bar{p}} = \frac{N(-q{\cdot}y_{had} > 0) - N(-q{\cdot}y_{had} < 0)}{N(-q{\cdot}y_{had} > 0) + N(-q{\cdot}y_{had} < 0)} \tag{1.5}$$

This is the definition for A_{fb} used in our previous work, Reference [1].

1.8.2 $t\bar{t}$ Frame

To make a measurement of A_{fb} in the $t\bar{t}$ frame, consider the following algebra:

$$\begin{aligned}
y_{top}^{rest} &= y_{top}^{lab} - y^{t\bar{t}\text{ system}} \\
&= y_t - \frac{1}{2}(y_t + y_{\bar{t}}) \\
&= \frac{1}{2}(y_t - y_{\bar{t}}) \\
&= \frac{1}{2}\Delta y_{top} \\
&= \frac{1}{2}q_{lepton}(y_{lep} - y_{had}) \qquad (1.6) \\
&\equiv \frac{1}{2}q\Delta y \qquad (1.7)
\end{aligned}$$

where y_{lep} and y_{had} are the rapidities of the leptonic and hadronically-decaying top systems measured in the lab frame. These equations show that top rapidity measured in the $t\bar{t}$ rest frame is proportional to the quantity $q\Delta y = q_{lepton}(y_{lep} - y_{had})$, formed from lab frame variables. Because Δy_{top} is the difference of two rapidities, it is Lorentz-invariant. We see from the definition of Δy_{top} (Equation 3 in reference [3]) that Δy_{top} is related to the angle of the top quark production with respect to the incoming parton:

$$y_t - y_{\bar{t}} = 2 \cdot \tanh^{-1}\left(\frac{\cos(\theta^*)}{\sqrt{1 + \frac{4m_t^2}{\hat{s} - 4m_t^2}}}\right) \tag{1.8}$$

where $\hat{s}$ is center of mass energy squared, m_t is the top quark mass, and $\cos(\theta^*)$ is the angle of the top quark production with respect to the incoming parton. Note that while there is not an exact 1:1 correspondence of Δy with $\cos(\theta^*)$ due to $\hat{s}$, the forward-backward nature remains the same. That is, if $\theta^* < 0$ then $\tanh^{-1}(\cos(\theta^*)) < 0$, so $\Delta y < 0$. Therefore asymmetries in Δy will be identical to those in $\cos(\theta^*)$, allowing an effective measurement of A_{fb} in the $t\bar{t}$ rest frame. In practice, the difference of top and anti-top rapidities is related to the difference of the hadronic and leptonic top rapidities. Again, because of CP invariance, we are able to multiply the distribution $(y_{had} - y_{lep})$ by -1 times the sign of the lepton q_{lepton}, resulting in $q\Delta y_{lep,had}$ being equivalent to $(y_t - y_{\bar{t}})$. Throughout this dissertation, we will refer to the quantity $-1 \cdot q_{lepton}(y_{had} - y_{lep}) = q_{lepton}(y_{lep} - y_{had})$ with the notation $q\Delta y$.

Using our new notation and the frame-invariance of $q\Delta y$, we are able to write

$$A_{fb}^{t\bar{t}} = \frac{N(q\Delta y > 0) - N(q\Delta y < 0)}{N(q\Delta y > 0) + N(q\Delta y < 0)} \tag{1.9}$$

In principle, this equation recovers a larger undiluted asymmetry than $A_{fb}^{p\bar{p}}$, but possibly with a larger uncertainty, as the neutrino uncertainty still enters through the involvement of y_{lep} in the calculation of Δy. However, since that means that the $A_{fb}^{t\bar{t}}$ measurement includes information "thrown-away" from the $A_{fb}^{p\bar{p}}$ measurement, we see that it is best to make *both* measurements to compare with other experiments and theoretical predictions. We will use the lab-frame measurement $A_{fb}^{q \cdot y_{had}}$ to establish the *existence* of a non-zero asymmetry, since there are no neutrinos present on the hadronic side of the top decay, making our A_{fb} measurement easier to interpret. Then we will use the $t\bar{t}$ frame measurement $A_{fb}^{q\Delta y}$ to study the properties of the asymmetry (such as

its dependence on rapidity, $\frac{dA_{fb}}{d(\Delta y)}$). We use this variable as opposed to -q·y_{had} because most theoretical predictions for the rapidity dependence are in the $t\bar{t}$ frame, and qΔy is Lorentz-invariant.

1.9 Measurement Strategy

The raw A_{fb} values calculated directly from data using Equations 1.4 and 1.9 need to be corrected back to the parton level by accounting for the presence of backgrounds and shape distortions. First, we note that non-signal events that pass our selection criteria cuts (see Sections 3.1 and 4.4.6), particularly those from electroweak processes, may have asymmetries that affect the final A_{fb} calculation. These backgrounds are estimated and subtracted, using the method we repeat and explain in Section 7.1. Event selection cuts (see Section 3.1) remove some signal events and modify the distribution shape of our production angle data, so we will need to correct for possible acceptance bias (explained in Section 7.2). Finally, the t and $\bar{t}$ four vectors must be reconstructed from limited information (4 jets, 1-2 btags, and missing transverse energy $\not\!\!E_T$, as explained in Chapter 3), and it is known that uncertainty in reconstruction causes smearing of the y_{had} and Δy distributions. The acceptance and smearing effects are corrected using a matrix unfold method that we explain in Section 7.2.

1.10 Previously Published Results

Using 3.2 fb^{-1} of data, Reference [1] observed

$$A_{fb}^{\text{-q·y}_{had}} = A_{fb}^{p\bar{p}} = 0.193 \pm 0.065^{stat} \pm 0.024^{syst} \tag{1.10}$$

This $p\bar{p}$ frame A_{fb} value is large, but still roughly consistent with the NLO prediction of $A_{fb} = 0.05 \pm 0.015\%$ within large uncertainty[2]. Reference [1] did not measure $A_{fb}^{t\bar{t}}$, but in Reference [2], using 1.9 fb^{-1} of data, the $t\bar{t}$ frame asymmetry was measured as

$$A_{fb}^{q\Delta y} = A_{fb}^{t\bar{t}} = 0.24 \pm 0.14^{stat} \tag{1.11}$$

These results in the two frames are roughly consistent with the theoretically expected dilution of 30% in passing from $t\bar{t}$ to $p\bar{p}$ frames [7].

[2] Still, one may also say that the value is *discrepant* by 2 σ – this is an unsatisfying level of precision, since it neither confirms nor rejects the Standard Model, nor BSM theories, either.

An independent detector experiment at Fermilab, DØ, has also measured A_{fb} [5, 6]. They did not correct their value to the parton frame, and chose simply to state the "raw" measured value. Using 0.9 fb^{-1} of data and the Δy variable, they find

$$A_{fb}^{D\emptyset}(|\Delta y|) = 0.12 \pm 0.08^{stat} \pm 0.01^{syst} \tag{1.12}$$

In their most recent publication [6] using 4.3 fb^{-1} of data, DØ finds

$$A_{fb}^{D\emptyset}(|\Delta y|) = 0.08 \pm 0.04^{stat} \pm 0.01^{syst} \tag{1.13}$$

1.11 The Differential Asymmetry $\frac{dA_{fb}}{d(\Delta y)}$

As we discussed in the introduction, A_{fb} measurements are a way to test the Standard Model and search for physics beyond the Standard Model. However, finding a non-zero A_{fb} is not all we can do – to distinguish between possible models it is advantageous to investigate the dependence of A_{fb} as a function of other variables. Now that our dataset has more than 1000 $t\bar{t}$ events, we are gaining enough statistical precision to do this.

The discussion in Reference [10] indicates that the cross-section terms responsible for the asymmetry are proportional to the β of the top/antitop quarks in the center-of-mass frame; thus, the asymmetry is expected to increase with the rapidity separation of the two quarks. We have shown above in Section 1.8.2 that the rapidity separation is very closely related to the production angle $\cos(\theta^*)$, so we are not surprised that Reference [10] predicts that the asymmetry grows almost linearly with the production angle, as seen in Figure 1.7. In fact, Reference [10] also uses re-summation techniques to examine the stability of the asymmetry at higher orders and finds only modest corrections, as shown.

In order to reproduce these calculations for ourselves, we use the program MCFM [22], which is a fully NLO calculation with NLO PDFs (next-to-leading-order parton-distribution-functions). In Figure 1.8, we see that the predicted NLO QCD $\frac{dA_{fb}}{d(\Delta y)}$ behavior is linear, as we expect from the close relationship between Δy and $\cos(\theta^*)$.

To compare with MCFM predictions, we measure the asymmetry as a function of our Δy distribution bins, which we then write as $\frac{dA_{fb}}{d(\Delta y)}$. We use 10 bins for a fine-dependence measurement of raw data and the background-subtracted

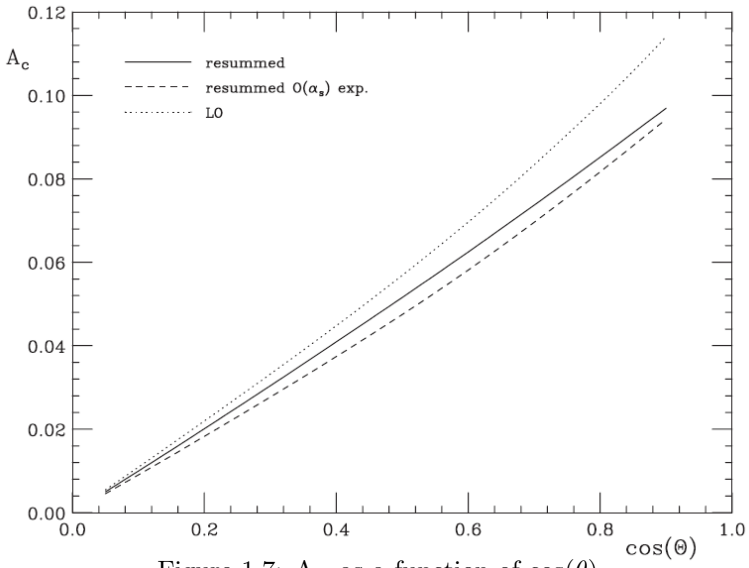

Figure 1.7: A_C as a function of $\cos(\theta)$
(Reproduced from Reference [10]) Note that A_C is equivalent to A_{fb}, as explained in Section 1.8.

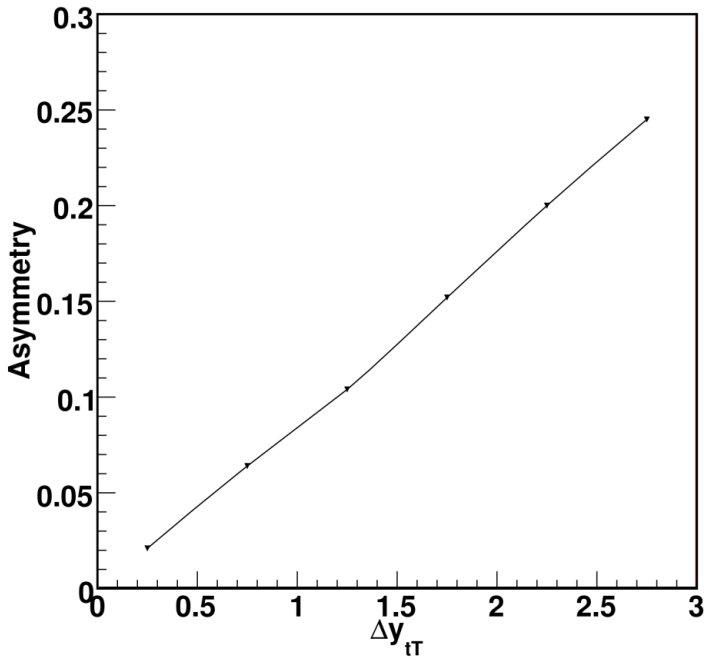

Figure 1.8: MCFM Prediction for $\frac{dA_{fb}}{d(\Delta y)}$

distribution, but in order to measure the dependence of the parton-level corrected data, we use 4 bins as discussed in Section 7.3. The rapidity dependence is then measured by examining the inner and outer bin pairs, using the forward and backward bin event counts in our usual formula. We perform this calculation for raw data as well as background-subtracted and corrected distributions, using the bin values from the 4-bin distributions. Statistical errors are propagated using the methods described in Sections 7.6 and 8. Thus we obtain $\frac{dA_{fb}}{d(\Delta y)}$ for background-corrected data as well as fully-corrected data.

We verify that this new measurement method works by examining Monte-Carlo (MC) simulation samples with known asymmetries and compare our measured values with the true A_{fb} and $\frac{dA_{fb}}{d(\Delta y)}$ values. By using pseudo-experiments (explained in Section 7.7), we can additionally verify the error propagation techniques and test our method for possible biases. We find that our method is reasonable and reconstructs the truth-level A_{fb} and $\frac{dA_{fb}}{d(\Delta y)}$ values quite well.

1.12 Main Plan for Thesis Dissertation

Now that we have introduced our variables and motivated our measurement by explaining some of the theory behind a possible non-zero A_{fb}, the rest of this dissertation is organized as follows: Chapter 2 discusses Fermilab, CDF, and our experimental apparatus used for obtaining our data. Chapter 3 will explain the event selection cuts used for semi-leptonic $t\bar{t}$ events, as well as the CDF Top Group method for reconstructing $t\bar{t}$ events from CDF data. Our $t\bar{t}$ signal Monte Carlo (MC) and background MC models are explained in Chapter 4. We discuss our 5.3 fb^{-1} dataset in Chapter 5, along with validation plots showing that the event reconstruction in Section 3.2 was good. The raw asymmetry measurement and dataset crosschecks are shown in Chapter 6. Our correction method for measuring the inclusive asymmetry at the parton-level is explained in Chapter 7. In Chapter 8 we introduce our new measurement of $\frac{dA_{fb}}{d(\Delta y)}$, the rapidity dependence of A_{fb}. We will discuss systematic uncertainties in Chapter 9. We end our work with our final measurement values and a discussion of their relevance in the Conclusion, Chapter 10.

Chapter 2.

Fermilab, the Tevatron, and CDF, the Experimental Apparatus

To measure properties of the top quark requires a sophisticated experimental apparatus. Particle physics experiments that could fit in one room and be managed by one university are a thing of the past – most current experiments require huge accelerators, complicated detector systems, and large collaborations of scientists and technicians.

Due to their heavy mass and small cross-section, top quarks are quite difficult to produce. As explained in Section 1.5, the top quark does not commonly exist in nature (except perhaps in cosmic rays), because these quarks decay rapidly into lighter particles. In order to obtain top quarks to study, it becomes necessary to produce them in high energy beam experiments as explained in Chapter 1. We examine data obtained from the Tevatron Accelerator at Fermi National Accelerator Laboratory (FNAL, or Fermilab) to collide protons (p) with antiprotons ($\bar{\mathrm{p}}$) at an collision interaction energy of $\sqrt{s} = 1.96$ TeV, energies sufficient for producing an occasional $\mathrm{t\bar{t}}$ pair with a mean mass of $M_{\mathrm{t\bar{t}}} = 172.5$ GeV/c^2 This analysis uses 1260 collisions that resulted in $\mathrm{t\bar{t}}$ pairs, details of which will be explained in Chapter 5. These data were obtained at the Collider Detector at Fermilab (CDF) from 2001 to 2010, corresponding to 5.3 fb^{-1} of total integrated luminosity.

2.1 Fermi National Accelerator Laboratory (Fermilab)

Fermi National Accelerator Laboratory is a multi-experiment site located in Batavia, IL, about 30 miles from Chicago. Planning for Fermilab, originally

named the "National Accelerator Laboratory", began in 1952 when the Midwestern Universities Research Association (MURA) formed with the purpose to design an accelerator. The lab was built in 1967 for a cost of $243 million, safely under the $250 million budget. Fermilab was built for the purpose of studying energy regions higher than those reachable by other experiments at the time. One of the most important early discoveries made at Fermilab was the bottom quark (also called the "beauty quark", or simply "b quark"), which was discovered in 1977 [15]. The lab is additionally known for many other important discoveries in particle physics, most notably the top quark in 1995 [14], the tau neutrino ν_τ in 2000 [16], the exotic Ω_b^- baryon in 2008-09 [17], and for observing single top production in 2009 [18]. Currently, Fermilab is competing with experiments at the Large Hadron Collider (LHC) in Europe to discover the Higgs Boson.

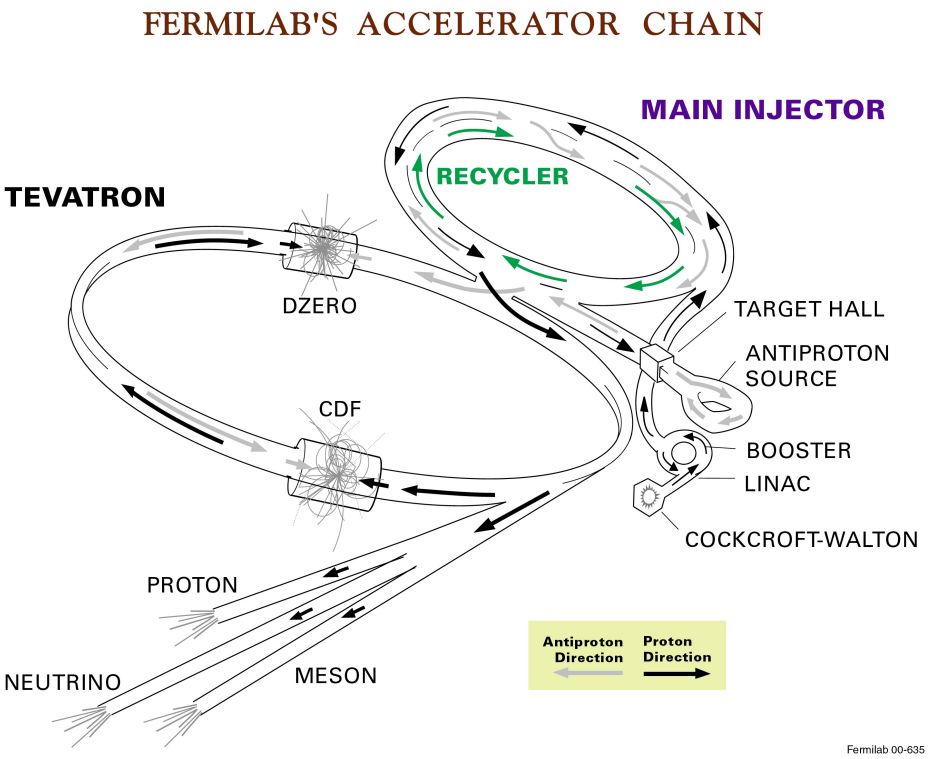

Figure 2.1: The Accelerator Complex at Fermilab (image courtesy of FNAL)

2.2 The Tevatron and Accelerator Systems at FNAL

Fermilab uses several accelerators linked back-to-back in order to reach high energies and accelerate protons to near the speed-of-light. The journey begins

in a humble tank of hydrogen gas, which is subsequently ionized to H^- by adding electrons using a device known as the "Magnetron". These particles are then accelerated in the "Cockcroft-Walton Generator", the first of several accelerators. The Cockcroft-Walton accelerates the H^- ions to 750 keV, and then it feeds them into the "Linac" (linear-accelerator). The Linac accelerates the ions to 400 MeV, which for H^- is roughly 70% the speed of light. These ions are directed into a carbon foil target that strips the electrons from the ions, leaving a bare proton (H^+). From here, the protons are accelerated using the Booster, which brings the particle energies to about 8 GeV. They are then accelerated by the "Main Injector" to energies of 120-150 GeV. At this point, some of the protons are sent to the "anti-proton source", where the beam is directed into a nickel target, producing anti-protons for use in collisions. In order to produce a beam of anti-particles, we do not want the particles to have a huge, wide distribution in energies (equivalently, particle velocities). The beam should have as small a variation as possible, so that we have a narrow distribution of velocities around the average beam velocity. This is done through a process known as "stochastic-cooling", where the beam is monitored and the spread of particle momenta is measured. By applying negative feedback through a kicker magnet, particles with momenta greater or less than the average bunch momenta are accelerated or decelerated to better match the average. If the bunch is thought of as a gas, making the particles have less velocity in the bunch rest frame is essentially cooling the energy, hence the term stochastic-cooling.

Once the energies of the anti-protons are stabilized, they are fed back into the Main Injector where they are also accelerated to 150 GeV, although they are made to travel opposite to the proton direction around the ring, since they are oppositely charged. Finally, both the protons and anti-protons are sent to the Tevatron, the largest accelerator at Fermilab. The Tevatron is a ring about 4 miles in circumference that accelerates particles to energies 980 GeV. When the opposing p and $\bar{\text{p}}$ beams collide at the CDF and D$\emptyset$ detectors, p$\bar{\text{p}}$ collisions have an energy of roughly $\sqrt{s} = 1.96$ TeV. A schematic diagram of the accelerator systems at FNAL can be seen in Figure 2.1.

The actual beams of protons and antiprotons are not continuous, but are actually made into "bunches". There are 36 bunches for each beam. Because of the spacing between bunches, it is possible to time collisions to occur in regular intervals and no activity in between collisions, allowing the products of one

collision to (mostly) leave the detector before the next collision occurs. There is some overlap for the products of interactions (most notably the time for ionized gas to reach a detector in the COT is longer than the time between collisions), but this effect is handled by the data acquisition system, as explained in Section 2.3.6.

2.3 The Collider Detector at Fermilab (CDF)

CDF is a large detector – actually, a system of detectors – positioned around one of the two beam collision points in the Tevatron ring (the other being the location of the DØ experiment). Here protons and antiprotons ($p + \bar{p}$) collide to produce new particles through strong-force interactions. Particles produced in line with the beam are lost down the beam pipe, but those produced moving perpendicular to the beam are able to be observed by the cylindrically-shaped detector systems located around the beam pipe. Detector tracks and particle identifications are then used to reconstruct the event. This process of tracking and particle identification requires sophisticated hardware and software to achieve the optimal data recording rate needed for top physics.

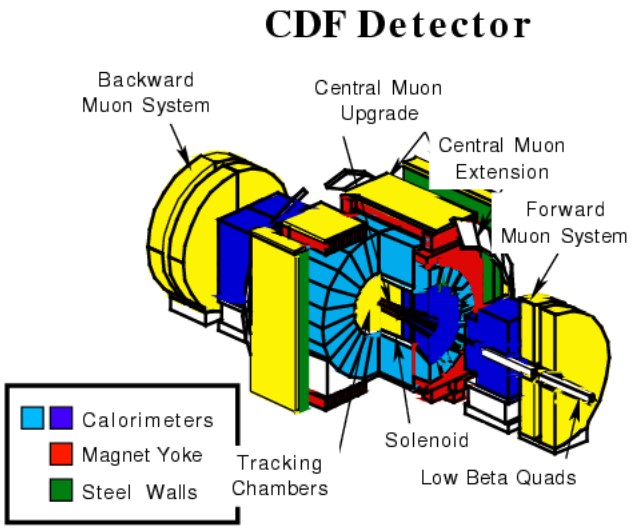

Figure 2.2: The Collider Detector at Fermilab (CDF) (image courtesy of CDF)

The detector itself is a cylindrically-shaped system, divided into subsystem layers categorized by their perpendicular distance from the beam line. A schematic of the CDF detector is shown in Figure 2.2. Dividing the detector into inner and outer systems is a large solenoid magnet. This solenoid produces a 1.4 T field that causes charged particles to have curved trajectories inside of the magnet tube. The curvature of these tracks can be used to calculate the momentum of these particles, which aids us in identifying various events. To record tracks, the inner-most layers of CDF are composed of a silicon tracking system, which is used for finding the path of charged particles with high angular and positional precision, which is needed for finding secondary vertices in b-tagging, as explained in Section 2.3.2. The next inner-most system is the Central Outer Tracker (COT), a drift chamber containing charged wires and inert gas. It is used in conjunction with the silicon tracking to find the paths of charged particles. The COT is explained in detail below in section 2.3.3.

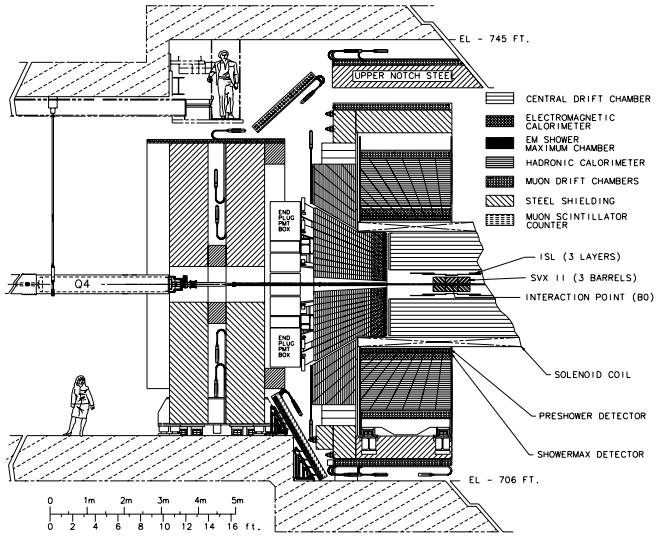

Figure 2.3: Another view of CDF (image courtesy of CDF)

Outside of these tracking systems and the solenoid magnet are the calorimetry systems. Calorimeters are used to find the energy of particles (both charged and uncharged), as well as assist in identifying particle types. In general, calorimeters have coarser angular resolutions than the tracking systems, but they can measure the total energy of all particles passing through, including neutral particles. All of these systems, along with a description of particle identification will be explained in detail below. A description of event reconstruction will be postponed until Section 3.2.

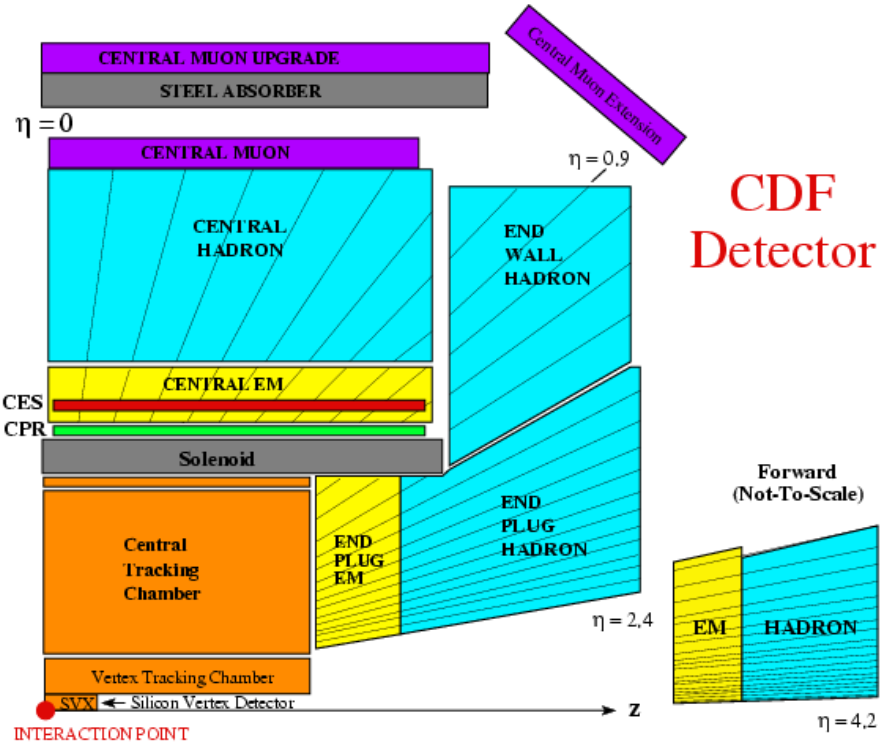

Figure 2.4: The Collider Detector at Fermilab (CDF) (image courtesy of CDF)

2.3.1 Coordinate System

Using the proton beam direction to define the positive $\hat{z}$ axis, CDF uses a right-handed coordinate system, with azimuthal angle ϕ measured with respect to the direction away from the Tevatron ring center, and polar angle θ measured from the z-axis. Because $p\bar{p}$ interactions are actually parton collisions (gluon and quark interactions, as explained in Section 1.5), the $q\bar{q}$ rest frame is not (usually) the same as the $p\bar{p}$ lab frame. It becomes useful to change to a modified coordinate system, and first we choose one that is related to particle momenta. Leaving z and ϕ unchanged, we can choose an alternative third orthogonal coordinate, called *rapidity*:

$$y = \frac{1}{2} \ln \left(\frac{E + p_z c}{E - p_z c} \right) \tag{2.1}$$

where E is the energy of the outgoing particle and p_z is the particle momentum in the $\hat{z}$ direction. We can also use another coordinate system that does not require the use of reconstructed energy and momentum quantities. *Pseudora-*

pidity is defined as

$$\eta = -\ln\left(\tan\frac{\theta}{2}\right) \tag{2.2}$$

This quantity is calculated from the detector θ variable, and is convenient in that it is independent of particle momenta. It can be shown that rapidity y and pseudorapidity η are equivalent for high energy particles, that is, when $E \gg m$. Thus, because the rapidity density of outgoing particles is roughly uniform, it is similarly uniform in η, so pseudorapidity η is used to define a measure of (solid) angular separation of tracks and jets in events. We define ΔR as

$$\Delta R = \sqrt{(\Delta\phi)^2 + (\Delta\eta)^2} \tag{2.3}$$

We will use ΔR to define jets, η for many of the detector validation checks in this analysis, and y for the reconstructed event quantities used in our physics analysis (namely -q·y_{had} and qΔy, as explained in Chapter 1). A schematic of the CDF detector is shown in Figure 2.4, showing the η positions of the sub-detector systems we discuss below.

2.3.2 Silicon Tracking

The heart of CDF is the Silicon microstrip detector system, which is used to measure tracks of charged particles. Closest to the beam line is the Layer 00 (L00), which is bonded directly to the beam pipe, so it has a radius of approximately 1.3 cm. Next are 5 layers comprising the Silicon Vertex Detector (SVX II). Finally, at a radius of approximately 29 cm are the 3 Intermediate Silicon Layers (ISL), which also extend out further along the z-axis so that they measure a higher η range.

Each layer of silicon is made of flat microstrip detectors, arranged so that they overlap at the edges and make a cylindrical shape, as shown in Figure 2.5. Strips are double sided (except for Layer 00), made of p-n silicon junctions and voltage biased so that charged particles passing through the detectors cause a current to flow in a cell. The junctions are positioned such that one layer measures the azimuthal position of a particle, while the other layer is set at either a 90 deg or 1.25 deg angle in order to measure the z-position, which then corresponds to an η position. The resolution of the silicon system is designed to be fine enough to measure the vertex position of jet cones formed by partons in a collision. B-quarks are known to have a lifetime of $\sim 1.6 \times 10^{-12}$ s, which gives the b-quark decay tracks a slight offset from the interaction point,

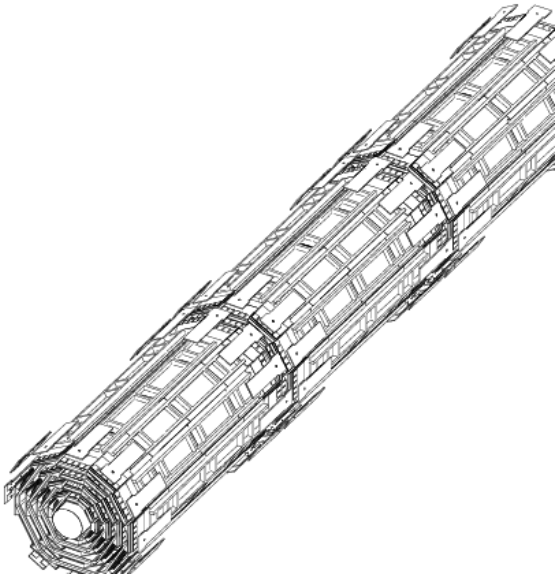

Figure 2.5: A view of the SVX barrels (image courtesy of CDF)

resulting in what is called a "secondary vertex" in the jet cone. The lifetime of the b-quark corresponds to a rough displacement of ~460 microns (for the B^0 meson), and the silicon detector is able to resolve this. The technique is known as "b-tagging" a jet, meaning that if a secondary vertex is found to exist in a jet, that jet has a high likelihood of being produced from a b-quark, as opposed to a lighter quark. There is a "contamination" of charm quark jets that get mistakenly tagged as b-quarks, but in our particular sample this contamination rate is small enough to ignore.

At CDF, Silicon microstrips are used for the inner volume instead of a wire-chamber because the silicon detectors have a much high resolution, which is needed in order to measure secondary vertices, a requirement for b-tagging. Unfortunately, silicon systems are much more expensive than wire-chambers, which is why the larger volume COT (explained in the next section) is used instead of a larger silicon system.

2.3.3 Central Outer Tracker (COT)

The Central Outer Tracker, or COT, also lies within the solenoid of CDF, outside of the silicon detectors. It is an "open-cell" drift chamber, having wires passing through an inert gas mixture composed of argon and ethane. The wires of the COT are positioned in 8 "superlayers" of cells, as shown in Figure 2.6.

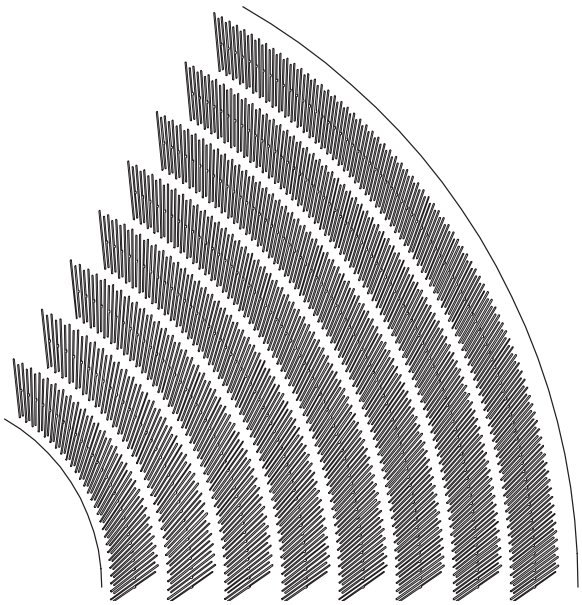

Figure 2.6: A view of a 1/6 section of the COT (image courtesy of CDF)

A high voltage is applied to the wires, causing an electric field to be produced. Each layer has 29 wires with 2000V and 3000V potentials applied in an alternating pattern with two additional ground wires at the ends. Half of the cells are arranged at an angle with respect to the other half so that the z (and η) positions of the tracks can be measured.

When a charged particle passes through the gas, it ionizes some of the gas molecules. The electrons produced in ionization experience a force due to the electric field produced by the voltage on the wires, which attracts the electrons to the nearest 3000V wire. This movement of ions produces a current on the wires, known as a "hit", which is measured by the COT system. However, electrons do not experience a continuous acceleration, since they collide with gas molecules, so they tend to move with a constant "drift-velocity". By knowing the drift velocity for the gas mixture used in the COT, the "radius of closest approach" between the incoming particle and the 3000V wire can be calculated to a resolution of approximately 180 microns.

Because the COT and silicon systems are within the 1.4 T solenoid field, charged particles experience a force that causes them to move in helical trajectories. Using the COT wire hits, a continuous track can be found and fitted to a helix, which can then be used to measure the incoming particle's transverse momentum P_t with a resolution of $\frac{\delta P_T}{P_T} = 0.0015\ P_T$.

2.3.4 Solenoid

Made from superconducting aluminum-stabilized NbTi and cooled with liquid helium, the solenoid in the CDF detector uses 4650 Amps of current to produce a 1.4 T magnetic field along the z-axis. This causes charged particles traveling through the field to have helical paths. The field strength is uniform to within 0.1%. Having a relatively uniform field causes the paths to be close to perfect helices, as opposed to more complicated shapes. This uniformity makes it easier for tracks to be fitted to the COT wire hits.

2.3.5 Calorimetry

While tracking can only be done for charged particles, the calorimeter systems of CDF respond to all particles, including neutral hadrons such as the neutron, and even electromagnetic radiation (photons). These systems are all located outside of the tracking systems and solenoid, with different subsystems designed to be sensitive to different particle types. By looking at which calorimeters respond and whether or not a track from the COT and silicon system points to that energy deposit, CDF can find the identity of particles. See Figure 2.7 for a schematic of which detectors respond to each particle type. We will discuss these various systems below.

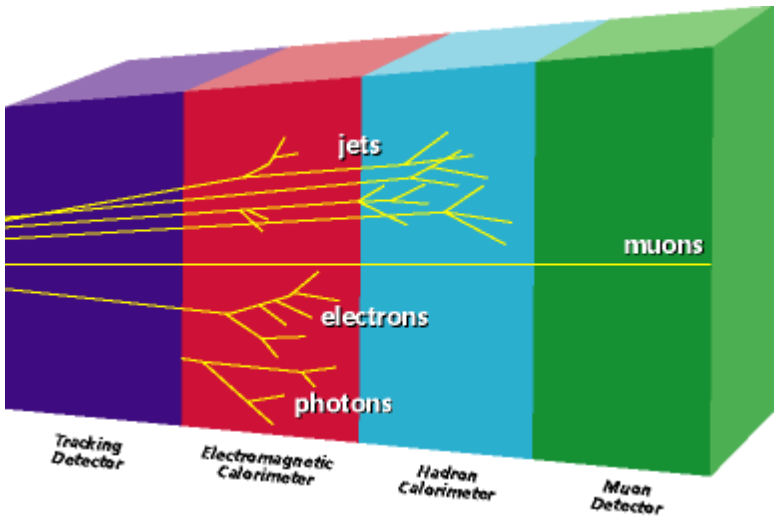

Figure 2.7: Detector-component responses for various particle types (image courtesy of CDF)

Electromagnetic Calorimeters

As explained briefly in the Introduction, electromagnetic calorimeters in CDF use layers of dense material alternated with transparent scintillating ma-

terial to measure the energies of particles traveling through it. The Central Electromagnetic Calorimeters (CEM) and Plug Electromagnetic Calorimeters (PEM) use 23 layers of lead (each a thickness of 4.5 mm) and scintillator plastic (4.0 mm). The CEM covers an η range of $|\eta| < 1.1$, while the PEM is used for the high eta regions $1.3 < |\eta| < 3.6$. As an electron passes through the dense region, the particle loses energy and momentum as it interacts with the electric fields of the lead nuclei. Scattering of an electron off of the positive nucleus produces a high-energy photon, which, if energetic enough, can split into an electron-positron pair. This is repeated until the photons produced no longer have the energy to split. By this point, the total number of electrons, positrons, and photons is quite high, and each particle contributes to producing photons in the scintillating region. This entire process is known as "showering", since the high energy incoming particles are essentially turned into a "shower" of lower-energy particles.

The distance a particle needs to travel through a material in order for its energy to be diminished by $1/e$ is known as its "radiation length" for that material. The electromagnetic calorimeters in CDF have about 21 radiation lengths for electrons in lead, so electrons that penetrate the entire CEM/PEM systems are reduced in energy by a factor of $\frac{1}{e^{21}}$. This means that most electrons stop within the calorimeter.

In order to match response in the calorimeters to tracks in the inner chambers, a small proportional wire chamber detector is placed about 6 radiation lengths inside the CEM and PEM. These are known as the Central EM ShowerMax system (CES) and Plug system (PES). Using capacitively-coupled scintillator strips, these detectors find the transverse profile of the showers in the CEM and PEM to help distinguish between electrons and photons, and to match tracks in the COT.

Hadronic Calorimeters

Because nuclear interactions have a smaller cross-section than electromagnetic interactions, in order to measure hadrons (such as protons, neutron, and $\pi^{\pm}$), it becomes necessary to use a larger detector and a different material for the showering layer. The Central Hadronic Calorimeter (CHA) and Plug Hadronic Calorimeter (PHA) use iron instead of lead, with 4.5 and 7.0 nuclear absorption lengths, respectively. This corresponds to 23 layers of iron plates (2-

inch) alternating with scintillator (6 mm). The showers produced by hadrons are larger and more varied than electromagnetic showers, resulting in a poorer resolution for these calorimeters ($0.50\sqrt{E_T}$ GeV for the CHA) compared with the electromagnetic calorimeters. These showers are grouped together ("clustered") to find cone-like "jets" of particles, characteristic of partons (quarks) in the collision products.

Muon Tracking Chambers

Because muons are much more massive than electrons (~200x), they are less likely to interact with matter through Bremsstrahlung showering processes as explained above in Section 2.3.5. Thus, muons travel straight through all of the previously mentioned detectors, leaving only an ion track but no particle shower. In order to ensure muons are distinguished from other particles, additional steel is placed around the CDF detector so that only muons can penetrate. Planar drift chambers are then placed around these shielded areas, consisting of 4 layers of argon-ethane filled proportional drift tubes. These detectors are somewhat similar to the COT in that they use the drift times to locate particles moving through the chamber. There is also an outer layer of scintillator, which is used to find the initial time a muon passes through the system, since the photon released by the scintillator is almost immediate, compared with the delay of ions moving in a drift chamber. By knowing the initial time, the drift time for ions in the drift chamber can be measured, so that a radius of closest approach can be found for a wire hit and a track fitted to the information. Two of the four layers in the drift chamber are set at an angle with respect to the other two so that the track position can be known in all dimensions.

These detectors are named according to their coverage range. The Central Muon Detector (CMU) and Central Muon Upgrade (CMP) cover the central range ($|\eta| < 0.6$), and if a muon is detected in both then it is called a "CMUP" muon. The Central Muon Extension (CMX) covers $0.6 < \eta < 1.0$, and the range $1.0 < \eta < 1.5$ corresponds to the Barrel Muon Upgrade (BMU).

2.3.6 Data Acquisition System (DAQ)

Although collisions happen every 396 nanoseconds at CDF (2.5 MHz), most do not produce anything "interesting", meaning that the interaction did not produce a heavy quark or boson, but instead was just a parton scatter. Because the rate of collisions is so high, it is not possible to record every event to

tape, so a filter system, called the Data Acquisition System (DAQ) is implemented to reject the non-interesting events. In order to do this, however, the DAQ must be able to identify the product particles quickly in order to decide whether to record it or not. This is accomplished in several steps – see Figure 2.8 for a schematic of the various processes we explain below.

At the first level, the CDF data acquisition system uses a hardware-level "trigger" to identify rough physics quantities. See Sections A.1.1, A.2.1, and A.2.2 in the Appendix, where we explain the Level 1 (L1) triggers used to identify leptons for the event selection used in this analysis. Because making these calculations takes more time than exists between collisions, event data is placed in the L1 storage pipeline, a buffer that holds 42 bunch crossing events while the L1 system reconstructs the relevant variables. This buffer is also needed because different detectors within CDF respond at different times – most notably the drift chambers such as the COT, which respond after other crossings have already occurred. By synchronizing the collision data between the detector, buffer, and the L1 trigger, we are able to accept or reject events safely. The L1 triggers also are able to scale with detector luminosity, so that the overall accept rate remains constant. The L1 system is designed to accept events at a rate of 50 kHz.

Next we have the Level 2 (L2) system. See Sections A.1.1, A.2.1, and A.2.2 in the Appendix, where we explain the L2 triggers used in this analysis. Because the L1 system decreased the data rate by such a large factor, the L2 system is able to reconstruct events more carefully and at a higher level, closer to the actual physics. The L2 system reconstructs leptons, photons, and finds jets in the event. L2 uses 4 event buffers to hold events while they are being processed. The final accept rate is about 300 Hz.

Finally, the Level 3 (L3) triggers are used to reduce the acceptance rate to 75 Hz, which is low enough to write events to tape. The L3 system uses software as opposed to the hardware used in the previous levels. Each event from accepted by L2 is sent to a processor in the L3 "farm" that fully reconstructs the event. The final accepted events are sent to the off-site computing cluster where they are processed offline. See Sections A.1.1, A.2.1, and A.2.2 in the Appendix for examples of L3 trigger criteria.

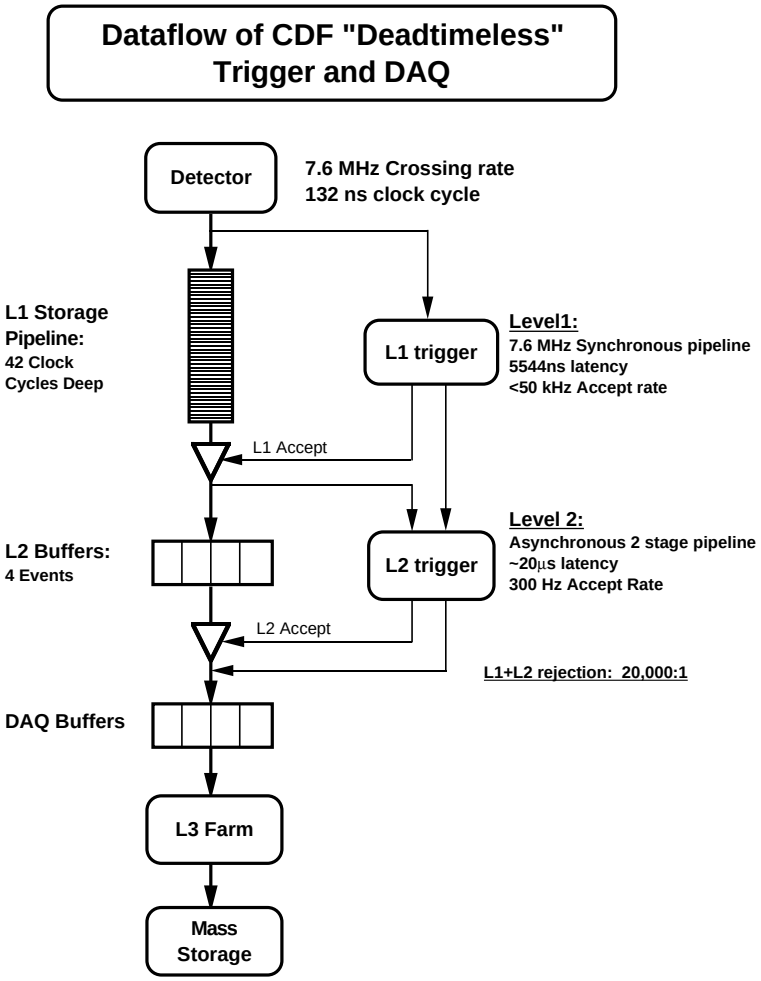

Figure 2.8: Data flow for the CDF DAQ system (image courtesy of CDF)

Chapter 3.

Event Selection and Reconstruction

As explained in Section 1.5, we choose the semi-leptonic channel of $t\bar{t}$ production for our data sample. See Figure 3.1 for a Feynman diagram of these decays. We see that the decay products include 4 jets (2 of which come from b-quarks), a lepton, and missing transverse energy $\not\!\!E_T$ from a neutrino. We choose our event selection cuts to reflect this and describe a summary of the cuts in Section 3.1. The full details of the event selection are shown in Appendix A. We then must *reconstruct* the detector-level event and match jets in the event to partons in the semi-leptonic decay diagram. This is explained in Section 3.2.

3.1 Event Selection

Note that these selection cuts are not unique to this analysis, but represent standard "legacy" cuts used by the CDF top group for all semi-leptonic $t\bar{t}$ analyses. We quote the full details of event selection in Appendix A, and additional information can be found in Reference [29]. As shown in Chapters 4 and 5, where we describe our background samples and data set, this set of selection requirements produces a 3.5:1 signal to background ratio in our dataset.

Here is a summary of the selection criteria for semi-leptonic $t\bar{t}$ events:

- One "tight" high-P_t lepton, $P_t > 20$, $|\eta| < 1$, as described in the Appendix, Sections A.1 and A.2. This is the first criteria for selection, and occurs at both trigger level and offline.
- Dilepton veto, which removes dilepton $t\bar{t}$ decays from our semi-leptonic $t\bar{t}$ sample.

- Z veto, which reduces the amount of background with Z-bosons.
- A primary vertex check, which ensures that the lepton and jets originate from the same collision.
- $\not\!\!E_T \geq 20$ GeV, which requires the presence of a neutrino in the event.
- ≥ 4 "tight" Jets, $E_t > 20$, $|\eta| < 2$, which reduces background by requiring the same number of jets as partons in a $t\bar{t}$ lepton plus jets event. "Tight" is a technical term related to the size of the region where energy from a jet was deposited in the calorimeter.
- ≥ 1 SecVtx "Tagged" jet, which rejects any background processes not containing heavy flavor quarks.

3.2 Event Reconstruction

The $t\bar{t}$ semi-leptonic decay results in an up-quark jet, down-quark jet, b and $\bar{b}$ jets, a lepton, and neutrino. Each of these products can be described by a four-vector of momentum (P_x, P_y, P_z, E/c) that contains the momentum and rest mass information for each particle. Four-vectors are convenient to use when calculating quantities in Special Relativity, since we can add four-vector components up for decay products and find the four-vector for a parent particle's momentum and rest mass.

We need to reconstruct the top-quark kinematics from these pieces in order to measure the rapidities and other variables. However, in a CDF event these physics objects only appear as general jets, leptons, and missing transverse energy $\not\!\!E_T$. It becomes necessary to take detector-level data for an event and match the jets to the partons in our semi-leptonic Feynman diagram and solve for the $t\bar{t}$ kinematics. See Figure 3.1 for two diagrams showing the "detector" event and desired "reconstructed" event. In order to do this reconstruction, the top group at CDF uses a procedure called a "kinematic fitter". We look at all possible jet-to-quark matches, and for the hypothetical $t\bar{t}$ system that each combination represents, we impose the constraints $M_{\mathrm{W}} = 80.4$ GeV/c^2 and $M_{\mathrm{top}} = 172.5$ GeV/c^2 using a χ^2-based algorithm. That is, a reconstructed W mass is calculated by adding the four-vectors of the detector-level lepton and neutrino (for leptonic decay) or the up and down quarks (for a hadronic decay), and the top and antitop are found by adding these W four-vectors with the appropriate b-quark four-vectors. The final masses are compared with the known masses of these particles. We then add the differences for these calculations together, resulting in a "χ^2" quantity, which we show in Equation 3.1. χ^2

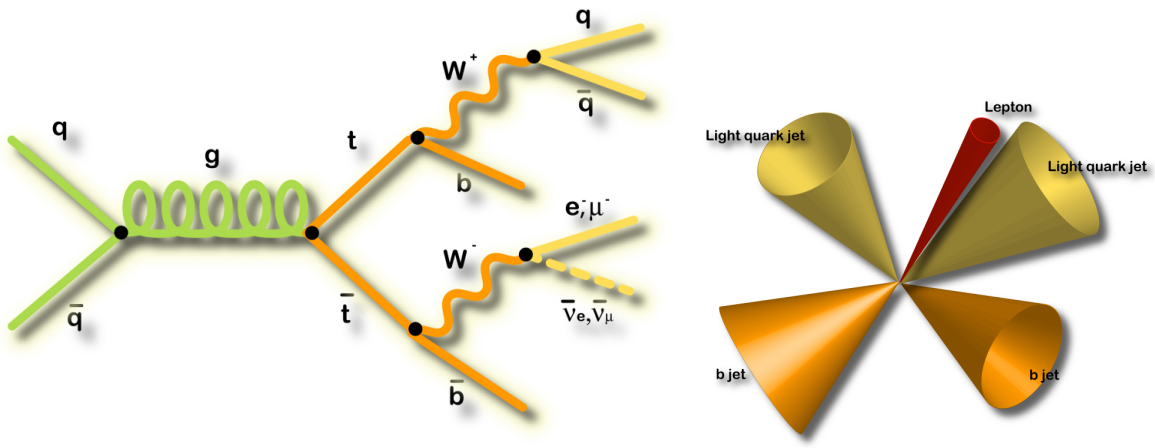

Figure 3.1: Semi-leptonic $t\bar{t}$ Feynman diagram and corresponding detector event

also includes terms to allow for the jets to vary within their energy resolutions, so that poorly measured jets do not result in a non-representative χ^2. Next, we reject all combinations of jet-to-quark matchings that are not consistent with the b-tagging information from the event, meaning that if there are one or two b-tagged jets in the event, these jets *must* be matched to a b-quark and not an up or down quark. Events having three or more tagged jets must match two of them to b-quarks. Finally, once we have a list of χ^2 values for all possible jet-to-quark combinations that are b-tagging consistent, we choose the combination with the lowest χ^2 as our reconstructed event.

The resulting combination of jet assignments is the best match resulting in the closest W and top quark masses. Thus, the kinematic fitter finds the best estimate for matching jets to each of the partons, according to the physics constraints suggested by the semi-leptonic $t\bar{t}$ Feynman diagram. This results in good estimates for the four-vectors of the higher-level physics objects, such as the W bosons and top quarks, which we can then study to measure the top quark rapidity.

Our kinematic fitter uses the following equation for calculating χ^2:

$$
\begin{aligned}
\chi^2 \;=\; & \sum_{i=\text{lepton, jets}} \frac{(P_t^{i,\text{meas}} - P_t^{i,\text{fit}})^2}{\sigma_i^2} \\
& + \sum_{j=\text{x,y}} \frac{(P_j^{UE,\text{meas}} - P_j^{UE,\text{fit}})^2}{\sigma_j^2} \\
& + \frac{(M_{jj} - M_{\text{W}})^2}{\Gamma_{\text{W}}^2} + \frac{(M_{\text{l}\nu} - M_{\text{W}})^2}{\Gamma_{\text{W}}^2} \\
& + \frac{(M_{bjj} - M_{\text{top}})^2}{\Gamma_{\text{top}}^2} + \frac{(M_{bl\nu} - M_{\text{top}})^2}{\Gamma_{\text{top}}^2}
\end{aligned} \tag{3.1}
$$

where the W mass $M_{\text{W}} = 80.4$ GeV/c^2 and the top mass $M_{\text{top}} = 172.5$ GeV/c^2.

In Figure 3.2, we see the distribution of χ^2 for data (black points with Poisson error bars) compared with the background (blue histogram) plus Pythia $\text{t}\bar{\text{t}}$ signal MC (blue histogram). Note that the signal has been renormalized such that the number of signal+background events will be equal to the number of data events (1260). We see that there is good overall agreement between the data and model, even out to the overflow bin at $\chi^2 \geq 90$, and that the distribution of χ^2 is mostly low with an exponential fall-off.

In Section 5.2, we compare the reconstructed parton kinematics in the data to the MC model for the $\text{t}\bar{\text{t}}$ signal and background. There is overall good agreement for all distributions, which we will make quantitative in the introduction to Chapter 5. This is a simultaneous test that the data behave as expected, that the MC model of the $\text{t}\bar{\text{t}}$ decay and background process kinematics are a good match to the data, and that the model reproduces the same (if any) misreconstruction effects seen in the data for the MC samples. Figure 3.3 shows our results for the main distributions used in our analysis. We show them here to emphasize their importance and show the reconstructed-level shapes. We describe these plots in detail in Chapter 6.

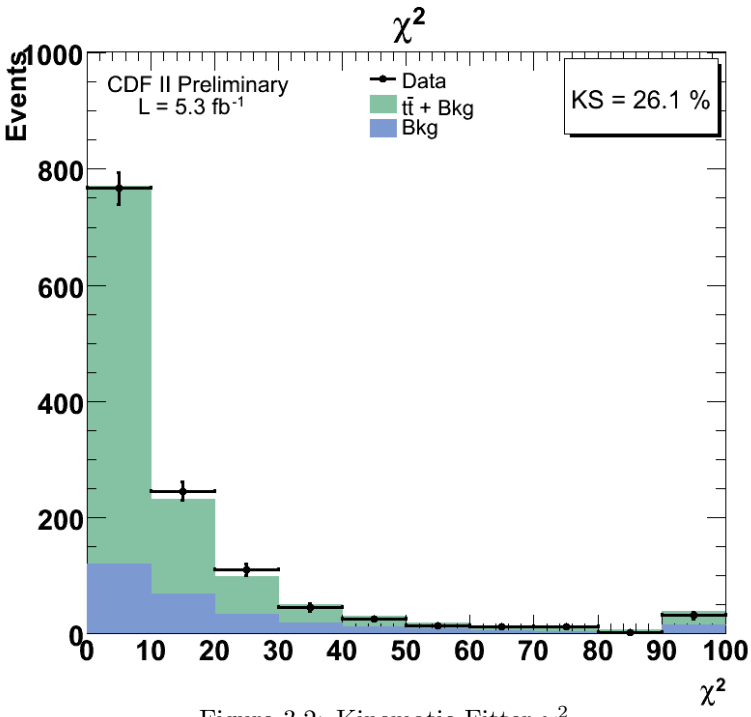

Figure 3.2: Kinematic Fitter χ^2

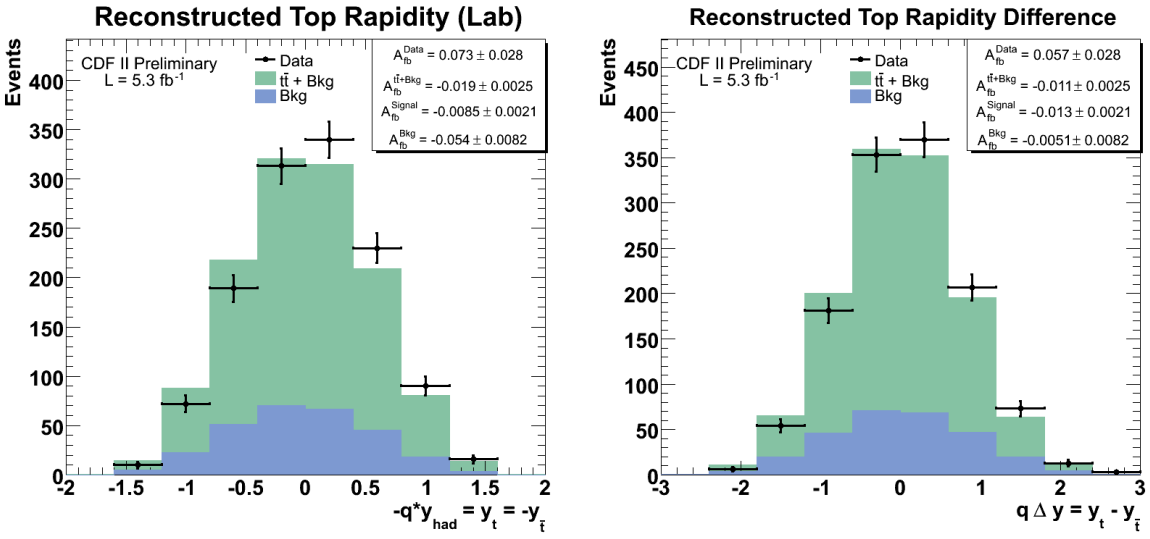

Figure 3.3: -q·y_{had} and qΔy distributions

Chapter 4.

Signal and Background Models

4.1 Modeling the $t\bar{t}$ Signal

In order to compare our data to prediction models, we need to generate simulations of $t\bar{t}$ events. This is highly complex. First, we know that the partons within protons and antiprotons have a distribution of momenta, so that the actual interactions vary in energy. These partons may radiate gluons before or after the collision, resulting in extra jets in the final event. Any simulation of signal must make estimations for these factors, along with estimates of the cross-sections of all processes, and additionally must predict the final jets and the detector response. There are many theoretical aspects to all of these simulation steps, and an in-depth discussion of these is beyond the scope of this dissertation. However, we will discuss a few aspects of using the Pythia Monte Carlo model in our analysis.

4.2 Tagging in the Monte Carlo

While the Monte Carlo can predict the event kinematics fairly well, the simulation results do not quite agree with the actual level of tagging and mistagging of jets. We can correct for this effect by constructing a jet-tagging probability for each jet, based on its kinematics and geometry in the detector. When we reconstruct events in our analysis, the solution to the kinematic fitter depends on which jets are tagged, since tagged jets are required to be assigned as bottom quarks. We actually use all possible tagging combinations, weighting by the probability for that tagging combination. Each tagging combination has a unique lowest χ^2 solution associated with it. We weight each solution from the fitter by its associated tagging probability. For example, in a four-jet event, the tagging probability for tagging just the first jet is:

$$P_{1Tag}^{Jet1} = P_1 \cdot (1 - P_2) \cdot (1 - P_3) \cdot (1 - P_4)$$

where P_1 is the tagging scale factor (SF) or the mistag probability, depending on whether the jet originates from light flavor or heavy flavor in the Monte Carlo. The event tagging probability is then:

$$P_{1Tag}^{Event} = P_{=1Tag}^{Jet1} + P_{=1Tag}^{Jet2} + P_{=1Tag}^{Jet3} + P_{=1Tag}^{Jet4}$$

4.2.1 Smearing due to Reconstruction

The Monte Carlo simulations generate actual parton-level $t\bar{t}$ decays. However, because we need to account for the geometry and efficiencies of our detector, the MC also simulates detector-level variables such as jet Et, $\not\!\!E_T$, etc. These quantities may or may not be equal to the true parton quantities. Furthermore, the kinematic fitter we use for event reconstruction allows jet energies to vary within their jet energy resolution, which further can modify the final fitted kinematics. We call these final variables "reconstructed" quantities and the original generated quantities "truth-level". The differences between the truth and reconstructed variables is called "smearing" and is related to our detector resolution. In Section 7.2, we will see that this smearing dilutes any truth-level asymmetries in the data and will discuss how to correct for this effect.

4.2.2 Modeling the Asymmetry at NLO

We do not have a usable simulation sample that includes the NLO QCD effect. That is, the CDF Top Group does not have a working MC@NLO sample, although work is in progress. Instead, we use a $t\bar{t}$ Pythia MC sample with $M_t = 172.5$ GeV/c^2. This sample has been verified by the CDF Top Group to closely match our data in most reconstructed variables, as we show in our data validation plots and discuss in Chapter 5. Pythia is a LO Monte Carlo and has no intrinsic asymmetry. We can use it as a null-signal control sample, and it is useful in that regard to establish that we are free from bias. A preliminary examination of an NLO MC sample showed only very small asymmetries in reconstructed distributions, which shows that our Pythia sample is a decent default.

4.3 Modeling Axigluons for testing non-zero A_{fb}

In order to have a control sample that resembles the data, we need a sample having a large A_{fb}. We have made an MC model using madgraph and a new physics model: the ctopoat$\bar{t}$ MC was made using the Axigluon differential cross section shown in Equation 1.2, with parameters M = 1.8 TeV, $g_V = 0$, $g_A^q = -\frac{3}{2}$, $-g_A^t = +\frac{3}{2}$, picked so that both the $M_{t\bar{t}}$ distribution and measured A_{fb} value of the MC closely match that of our data. The axigluon mass was chosen to be $M_G = 2.0$ TeV, and we chose coupling parameters that resulted in an asymmetry value of $A_{fb} = 11\%$. The t$\bar{t}$ cross section increased by 2% in this sample. See Figures 4.1 and 4.2 below, where we compare the ctopoa+background shape (green histogram) with data (black) using our standard background predictions (blue). Ignore the KS-test values for now, we will discuss these in the introduction to Chapter 5. For now, it is sufficient to see the the data seem to agree with the signal+background shapes. We see that t$\bar{t}$ctopoa/madgraph does reproduce the raw A_{fb} seen in the data (in fact, it is actually a bit high) while keeping the $M_{t\bar{t}}$ distribution in relative compliance with the data. We are encouraged that there is a physics model that can do this, but more importantly, it means that we can test a correction procedure on a sample that has a large asymmetry and no other spectrum distortions (as would be the case of Z'$\rightarrow$ t$\bar{t}$, for example).

We use this MC in Section 7.2, Chapter 8, and elsewhere – whenever we need a sample with non-zero A_{fb} for verification of a procedure. For example, in Section 7.7 we use t$\bar{t}$ctopoa to verify that we can correct the reconstructed $-q\cdot y_{had}$ and $q\Delta y$ distributions back to the parton level and measure the correct A_{fb} value.

Note that we are not claiming this sample as signal hypothesis – we are merely using ctopoa as a non-zero A_{fb} control sample.

4.4 Modeling the Background

In the previous chapter, we described selection cuts used for obtaining our t$\bar{t}$ sample. Note that events passing these criteria include t$\bar{t}$ events as well as non-t$\bar{t}$ events that "slip through" and contaminate our sample. The selection criteria were chosen to maximize the number of true t$\bar{t}$ events (signal) while minimizing non-t$\bar{t}$ events (background). In order to correctly measure the t$\bar{t}$

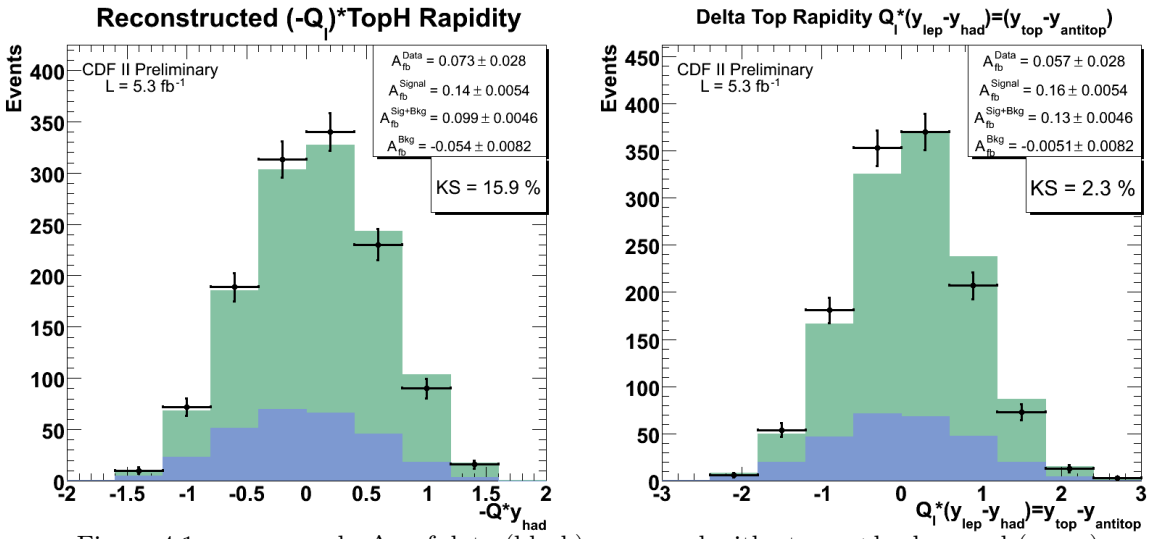

Figure 4.1: -q·y_{had} and qΔy of data (black) compared with ctopoa+background (green)

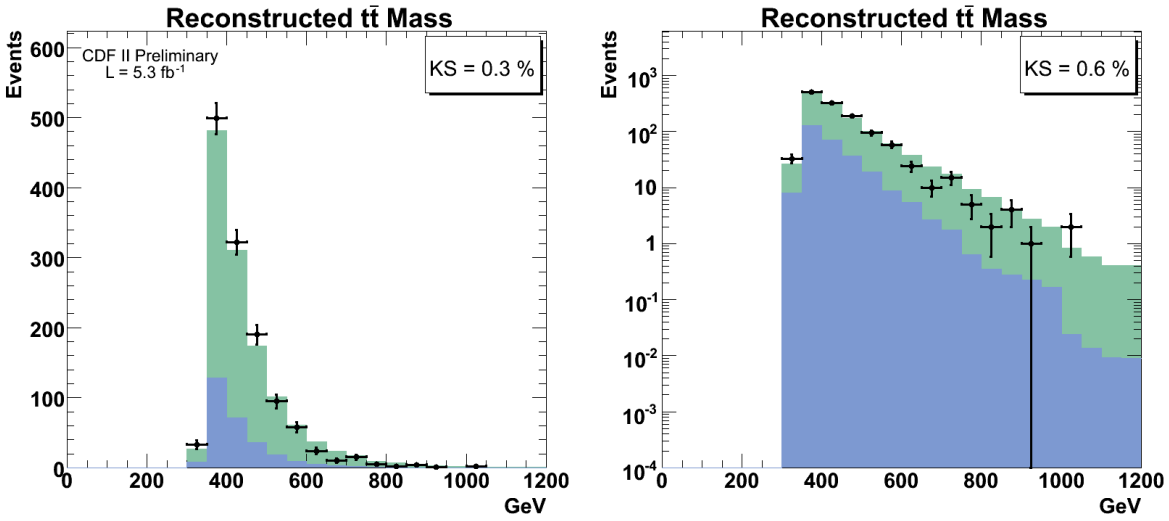

Figure 4.2: $M_{t\bar{t}}$ of data (black) compared with ctopoa+background (green) for ctopoa

production asymmetry A_{fb}, we must subtract off the background contribution, as described in Section 7.1. This requires a careful estimate of the background shapes and cross-sections. The QCD background model we use is generated from data events that had a jet that faked an electron. The rest of the background components are generated from Monte-Carlo (MC) simulations of all physics processes known to have contributions to our sample selection. Once we have obtained shapes for all processes, the cross-sections for these interactions are calculated using the method explained below in Section 4.4.6. The non-$t\bar{t}$ processes are categorized as electroweak, single-top, QCD, W-boson plus heavy-flavor quarks, and W-boson plus light-flavor quarks. We explain these processes below.

4.4.1 Electroweak Processes

Electroweak processes (those involving $W^{\pm}$ and Z bosons) frequently produce leptons and neutrinos in their decay products. If there are jets in the event from gluon radiation (and at least one jet is tagged), the final event may satisfy our selection criteria. To account for these backgrounds, we examine WW, WZ, and ZZ$\rightarrow \tau\tau$ events and estimate the background contribution numbers using the theoretical cross section, our data sample luminosity, and our selection efficiency, calculated from our MC samples of WW, WZ, and ZZ. The theoretical cross sections for these processes are found in Table 4.1. To calculate the number of background events, we use the formula

$$N_{p\bar{p}\rightarrow X} = \sigma_{p\bar{p}\rightarrow X} \cdot \epsilon_{pretag} \cdot \epsilon_{tag} \cdot \int dt \cdot \mathcal{L} \tag{4.1}$$

where $\sigma_{p\bar{p}\rightarrow X}$ is the theoretical cross section, ϵ_{pretag} is the "pre-tag" selection efficiency (we use the selection criteria in Chapter 3 but remove the tagged jet requirement) derived from MC, and $\int dt \cdot \mathcal{L}$ is the total luminosity of our data sample. ϵ_{tag} is the tagged selection efficiency, which we calculate using the formula

$$\epsilon_{tag} = \epsilon_{tag}^{MC} \cdot \Phi_{MC,data} \tag{4.2}$$

where ϵ_{tag}^{MC} is the tagged efficiency of the MC and $\Phi_{MC,data}$ is a scale factor that accounts for the differences between tagging MC as opposed to data. From these formula, we find that number of expected electroweak background events in our sample is

$$N_{Electroweak} = 19.5 \pm 1.3 \tag{4.3}$$

Process	Cross Section
WW	13.25 ± 0.25 pb
WZ	3.96 ± 0.06 pb
ZZ	1.58 ± 0.02 pb
ZZ $\rightarrow \tau\tau$	13.0 ± 1.5 pb

Table 4.1: Theoretical cross sections for WW/WZ/ZZ background contributions

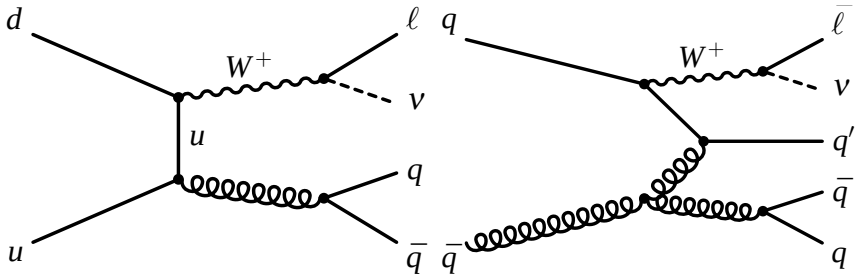

Figure 4.3: Representative Feynman diagram for Wb$\bar{\text{b}}$, Wc$\bar{\text{c}}$, and W+lf production for 2 and 3 jets.

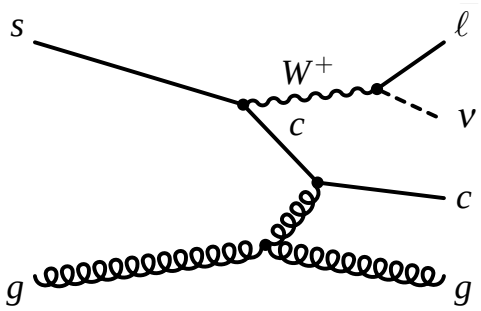

Figure 4.4: Representative Feynman diagram for Wc production.

4.4.2 QCD Processes

Because there are so many possible interactions between partons in a collision, QCD predicts many processes that pass our event selection. To pass our cuts, however, there must be a lepton found in the event, missing transverse energy $\not\!\!E_T$, and at least one b-tagged jet. A lepton can be found in QCD processes when a jet is misidentified as a lepton (we call this a jet "faking" a lepton), or if a bottom or charm quark leptonically decays. Missing transverse

energy can be present in an event if jets are mis-measured in the calorimeters. There can be an actual heavy quark in a QCD event, or tracks could be mis-measured, leading to an incorrectly mistagged jet. These "fake" events happen for only a small percentage of all QCD interactions, but because there are so many, these fakes contribute much of the background. A diagram of one possible contribution to the QCD background is shown in Figure 4.5.

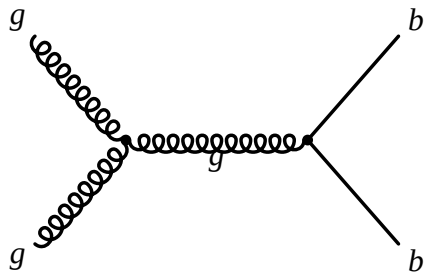

Figure 4.5: Representative Feynman diagram for QCD backgrounds

We use data to find the shape of our QCD background, using events that are known to have jets faking leptons. This is accomplished by loosening our event selection cuts so that a high background-to-signal ratio is obtained. However, we will also need a prediction for the cross-section of these interactions for the QCD events that pass our actual selection cuts for $t\bar{t}$. The most significant variables for distinguishing between QCD and $t\bar{t}$ events are the missing transverse energy $\not\!\!E_T$ and the lepton isolation (I_l, as defined in Appendix A). Because there are no weak interactions in QCD events, there should be no neutrino and thus no $\not\!\!E_T$. Lepton isolation I_l is important because there are typically more tracks close to a lepton in QCD events than in $t\bar{t}$ events. Jets faking leptons will similarly have less "lepton" isolation, since the fake lepton is surrounded by other tracks. Using a selection of events before b-tagging, we can construct an "$\not\!\!E_T$ vs. lepton isolation" plane, divided into four regions:

- Region A: $\not\!\!E_T < 15$GeV and $I_l < 0.2$
- Region B: $\not\!\!E_T < 15$GeV and $I_l > 0.1$
- Region C: $\not\!\!E_T > 20$GeV and $I_l > 0.2$
- Region D: $\not\!\!E_T > 20$GeV and $I_l < 0.1$

Region D is the signal region, whereas regions A and B are dominated by QCD background events. We assume that the fraction of events that pass the isolation cut is uncorrelated with $\not\!\!E_T$, which allows us to estimate the *fraction*

of QCD events in the signal region D using the ratio

$$F_{QCD,\text{notag}} = \frac{B}{A} \cdot \frac{C}{D} \tag{4.4}$$

This fraction is calculated using a "pretag" event selection, meaning that we do not make any requirements on the number of b-jets in the events. We then can find a similar fraction for the number of b-tagged events in the signal region by looking at a similar ratio of events after requiring a b-tagged jet.

$$F^1_{QCD,\text{tagged}} = \frac{B^{\text{tagged}}}{A^{\text{tagged}}} \cdot \frac{C^{\text{tagged}}}{D^{\text{tagged}}} \tag{4.5}$$

However, because requiring a b-tag rejects a lot of background, we do not have the necessary statistics to use this formula by itself. So we additionally use the *ratio* of events in Region B before-and-after tagging to calculate an expecting tagging rate for background and apply it in this formula:

$$F^2_{QCD,\text{tagged}} = F_{QCD,\text{notag}} \cdot D \cdot \frac{B^{\text{tagged}}}{B} \tag{4.6}$$

Using the average of $F^1_{QCD,\text{tagged}}$ and $F^2_{QCD,\text{tagged}}$, we find a background prediction of 67.5 ± 26.9.

4.4.3 Single Top

While most top quarks are produced in pairs via quark-quark collisions or gluon-fusion (as explained in Section 1.5), it is possible for single top quarks to be produced through electroweak processes. If a W boson is produced through an energetic $u\bar{d}$ or $d\bar{u}$ interaction, it can then decay into a top quark and bottom quark. This is known as the "S" channel, and is shown in the left diagram of Figure 4.6. Another way to generate single top quarks is through the "T" channel, as shown in the right diagram of Figure 4.6, where a virtual W boson is created from a high momentum gluon that interacts with the $b\bar{b}$ "sea" to produce a virtual W boson that interacts with the quark from an incoming proton or antiproton. Since both the s- and t-channels contain real top quarks, it is possible for these events to pass our selection cuts, but we wish to treat these as backgrounds for our analysis (since these are quite different events from $t\bar{t}$, so production angle is more difficult to define, plus the events will not be correctly handled by our kinematic fitter). We use predicted cross-sections for these processes (Table 4.2) and multiply by our total luminosity to find a predicted number of background events. We find

$$N_{singletop} = 15.6 \pm 0.9 \tag{4.7}$$

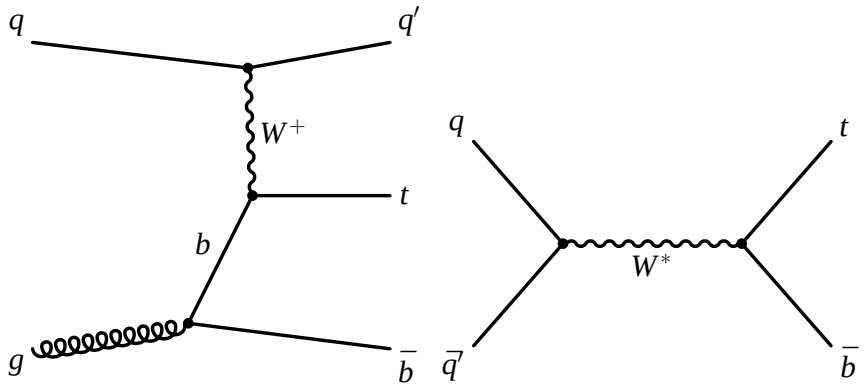

Figure 4.6: Feynman diagrams for t- and s-channel single top production

Process	Cross Section
$t\bar{t}$	6.7 ± 0.07 pb
t channel single top	1.98 ± 0.08 pb
s channel single top	0.88 ± 0.05 pb

Table 4.2: Theoretical cross sections for single top background contributions, compared to the $t\bar{t}$ cross section

4.4.4 W-Boson Plus Heavy Flavor Quarks

Some background events contain a W boson and heavy quarks – a W$b\bar{b}$ event is shown in Figure 4.7. Since these W bosons can decay leptonically, the final event may contain a lepton and $\not\!\!E_T$, and the number of jets can also be high enough to pass our selection cuts if there are additional QCD processes (such as gluon radiation). We calculate the expected number of these W+heavy flavor (W+HF) events using the following equation:

$$N_{W+HF} = (N_{pretag}(1 - F_{QCD}) - N_{electoweak} - N_{SingleTop} - N_{t\bar{t}}) \cdot f_{HF} \cdot \epsilon_{tag} \quad (4.8)$$

where the numbers for the other background processes come from the sections above, f_{HF} comes from an "Alpgen" MC simulation that includes all possible single-W production diagrams [20], and ϵ_{tag} is defined in Equation 4.2. We actually calculate f_{HF} and ϵ_{tag} separately for the processes W$b\bar{b}$, W$c\bar{c}$, and Wc. We find the following number of background events for these processes to be

$$N_{W+HF} = 135.5 \pm 35.2 \quad (4.9)$$

4.4.5 W-Boson Plus Light Flavor Quarks

One large background in our event selection comes from W events that have "light flavor" jets (u,d,s) where one of the jets is mistagged, faking a b-

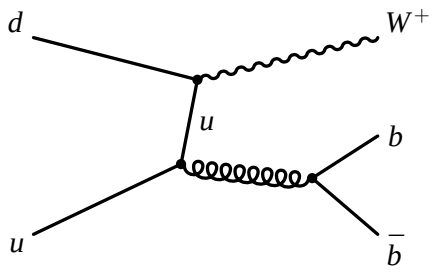

Figure 4.7: Feynman diagram for Wb$\bar{\text{b}}$ backgrounds

quark. These diagrams are similar to the diagram above in Figure 4.7, only having light quarks in place of the b-quarks. Since we perform b-tagging by looking for events that have a secondary vertex, it is possible to find events having a *negative* secondary vertex, which could not correspond to a b-quark. It is presumed that the number of these negatively tagged jets is equal to the number of mistagged events in the tagged sample, so we can find a fraction ratio of mistags to tags. Using a high-statistics sample made from 50 GeV jet triggers, this negative tag rate is found to be well described by a function of jet Et, number of good SVX tracks, sum of all jet Et, jet η, and jet ϕ. By parameterizing the mistag rate by a function of these variables, we have an idea of how frequent a W+LF event passes our cuts. We use the following equation to estimate the number of background events for W+light flavor (LF) processes:

$$N_{W+LF} = N_{mistag}^{prediction} \cdot \frac{(N_{pre} - N_{pre}^{t\bar{t}} - N_{pre}^{QCD} - N_{pre}^{W+HF} - N_{pre}^{electroweak} - N_{pre}^{singletop})}{N_{pre}} \tag{4.10}$$

we find our predicted number to be

$$N_{W+LF} = 45.2 \pm 9.8 \tag{4.11}$$

4.4.6 Background Cross-Section Estimates

Our background models and their normalizations are based on the standard CDF top group procedure [24] explained above, calculated from our 5.3 fb^{-1} of data. The samples used for generating our background shapes are listed in Table 4.3. The calculated contribution of each background component in our sample is given in Table 4.4. The total number of background events in the sample is 283.3 ± 91.2. The sample contains 1260 top-pair events, and the ratio of number of signal events to background is roughly 3.5:1.

Process	Dataset ID	Type
$t\bar{t}$	ttop25	Pythia
QCD	gjt1X	Jet Electrons
Wbb	btopXw, dtopXw	Alpgen
Wcc	btopXX, ctopXw, etopwX	Alpgen
Wc	stopwX, otopwX	Alpgen
Wlf	ptopXw, ptopwX, utopX, utopXw	Alpgen
WW/WZ/ZZ	itopww, htopww, itopwz, htopwz, itopzz, htopzz	Pythia
Single Top - S	stop26, stop23	MadEvt/Pythia
Single Top - T	stop27_28, stop3m	MadEvt/Pythia
Z+Jets	btopzX, ztopbX, ztopcX, ztoppX, ztopXp	Alpgen

Table 4.3: $t\bar{t}$ Signal and Background MC Samples

Process	==4 Jets	$\geq$ 5 Jets
W + HF Jets	109 $\pm$ 34.1	26.5 $\pm$ 8.6
Mistags (W+LF)	36.8 $\pm$ 9.3	8.4 $\pm$ 3.1
Non-W (QCD)	50.1 $\pm$ 25.3	17.4 $\pm$ 9.2
Single Top S	5.6 $\pm$ 0.6	1.2 $\pm$ 0.1
Single Top T	7.5 $\pm$ 0.6	1.3 $\pm$ 0.1
WW	6.2 $\pm$ 0.8	1.7 $\pm$ 0.2
WZ	1.6 $\pm$ 0.2	0.5 $\pm$ 0.1
ZZ	0.6 $\pm$ 0.1	0.1 $\pm$ 0.01
Z+Jets	7.1 $\pm$ 0.9	1.7 $\pm$ 0.2
Total Prediction	224.5 $\pm$ 47.8	58.8 $\pm$ 14.2

Table 4.4: Summary of calculated background cross-section normalizations
See Table 7.1 for the raw A_{fb} values of each background sample.

Chapter 5.

Dataset and Validation

In order to trust our measurement, we must first check that the detector does not have an inherent asymmetry or that the kinematic fitter biases our reconstructed quantities. The plots in the following sections demonstrate that this is not the case, as data match the signal+background model prediction and do not show an asymmetry for detector-level variables (jet rapidities, for example), but only show asymmetries for reconstructed top quark rapidities.

In order to make this agreement quantitative, we perform a "Kolmogorov-Smirnov" (KS) test for each of our validation plots. Roughly speaking, this statistical test is a measure of how similar two histograms are – for histograms coming from the same true distribution, KS-test values should be greater than one or two times $1/\sqrt{N}$, where N is the number of events in the histogram. Our data sample has 1260 $t\bar{t}$ events, so $1/\sqrt{N} = 0.028$. Thus we expect that the KS-test values for our validation plots will vary between 1 and 0.02 or so, and that discrepant distributions will have very low KS values. We see that our histograms have KS values greater than 10^{-3} (except for the top angle distributions), thus we conclude that our data agree with our signal+background model.

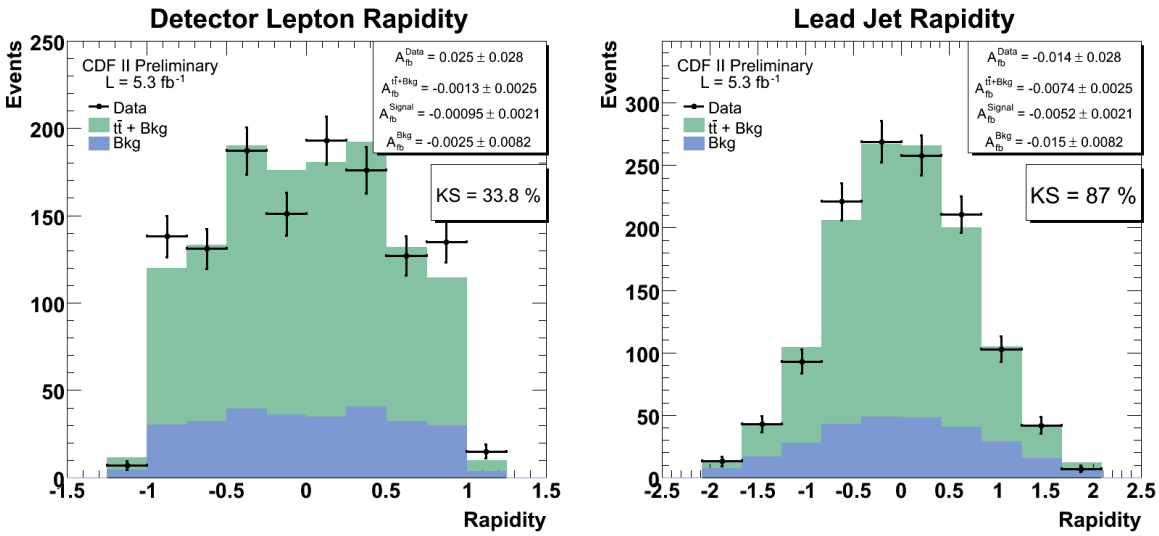

Figure 5.1: Sample validation distributions – see below for the full set of plots

5.1 Detector Variables and Observables

Before checking reconstructed $t\bar{t}$ event variables, we will first verify that our signal and background shapes correctly model the CDF detector. To do this, we examine "detector-level" event variables such as jet energy, jet rapidities, lepton Pt and rapidity, and various angles between the jets, lepton, and $\not\!\!E_T$. Plots showing low KS-test values would suggest that our signal+background model does not match our data, or that the detector itself might have biases for detecting forward or backward-moving particles. However, we instead see that our KS values are above 10^{-3} for all such distributions, and that no obvious asymmetries exist. See the plots in Figure 5.1, which shows the lead jet energy and rapidity distributions. The fact that our data match our signal+background model so well both validates our model and allows us to believe our detector has no inherent biases. If such biases did exist, the A_{fb} values for the data and signal+bkg shapes would be discrepant or differ significantly from zero, and we see that this is not the case.

Our validation plots tabulated below use the data sets explained above. See Figure 5.1 above for an example of our validation plots. The black points represent data with Poisson errors, the blue region is the normalized background MC, and the green region is Pythia signal MC normalized such that background+signal is equal to the number of data events (1260).

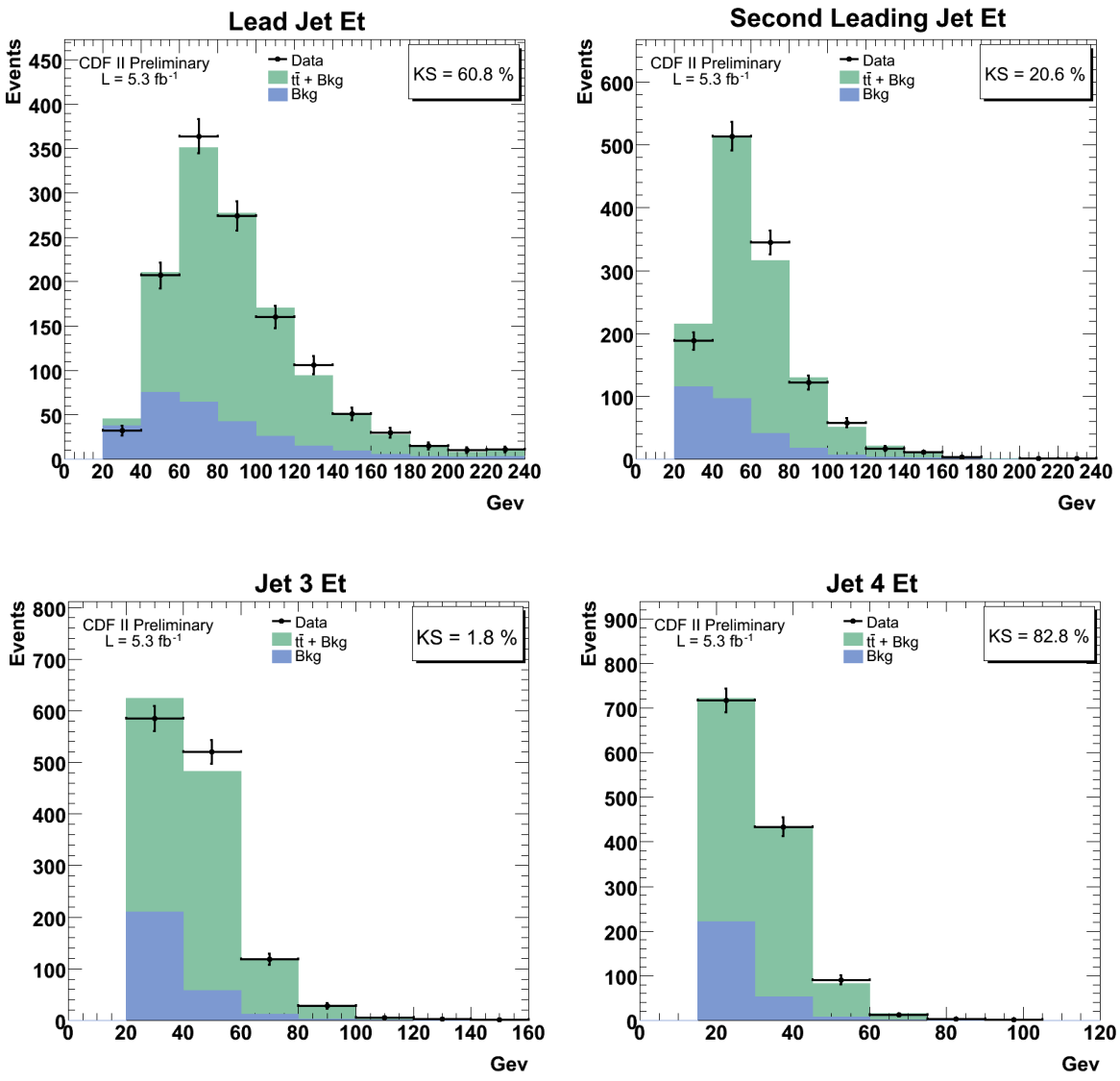

Figure 5.2: The Leading Jet Et Distributions

We see that the energy distributions for the leading jets match our model predictions. If jets from QCD processes are mis-assigned to partons in the $t\bar{t}$ decay, these errors must be happening at the same rate in the MC as in data. This is the main thing that we wish to ensure, since as long as the kinematic fitter treats both data and MC the same we can safely compare the A_{fb} values to each other. In other words, it helps us be more confident that any observed A_{fb} is not caused by the kinematic fitter, or else we would see an anomalous non-zero A_{fb} value in the reconstructed signal+bkg shape.

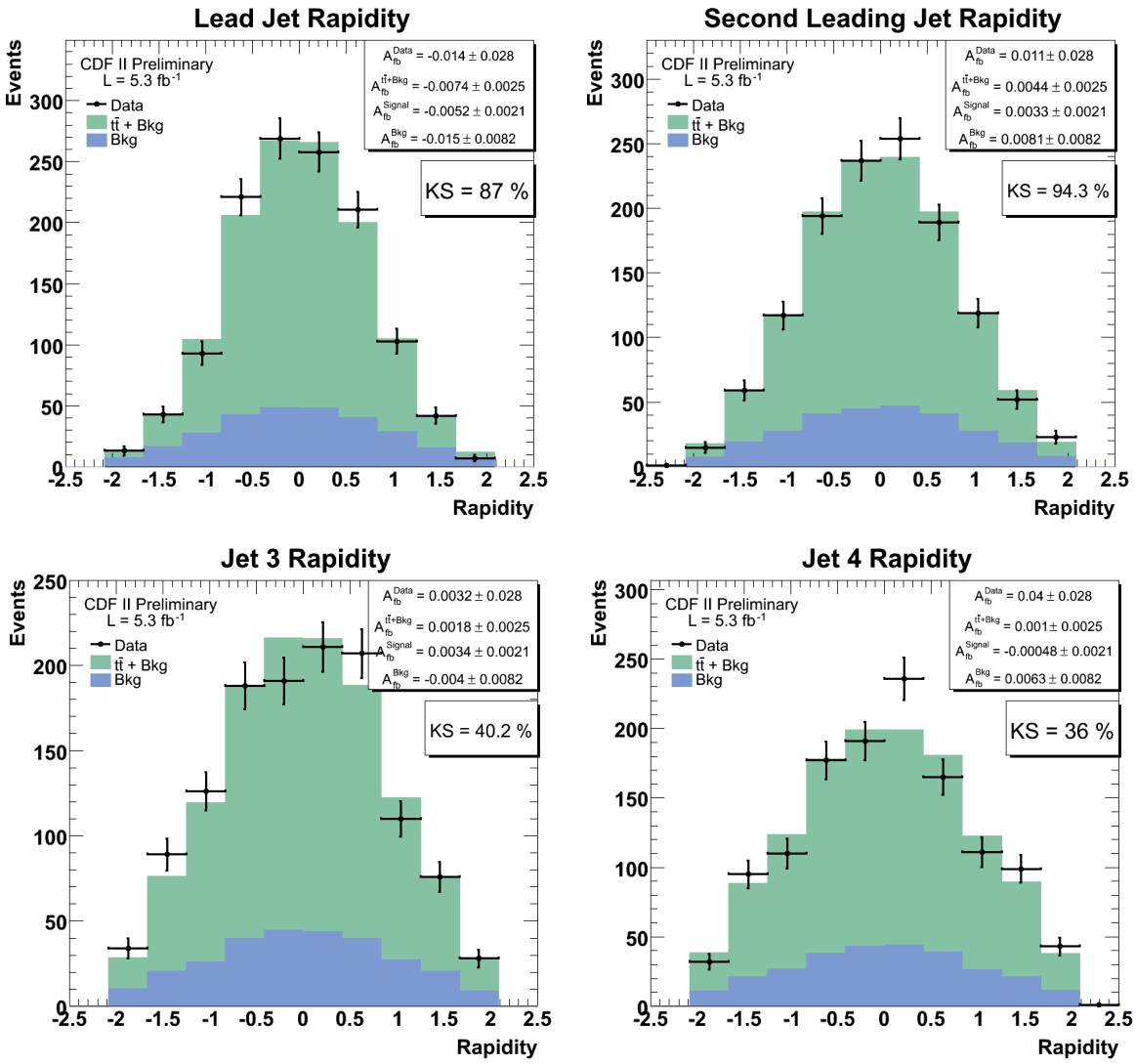

Figure 5.3: The Leading Jet Rapidity Distributions

Similarly, we find that the rapidities of the jets match the model well. This shows that there is no inherent asymmetry already present in the detector that would falsely make an asymmetry in our reconstructed parton variables.

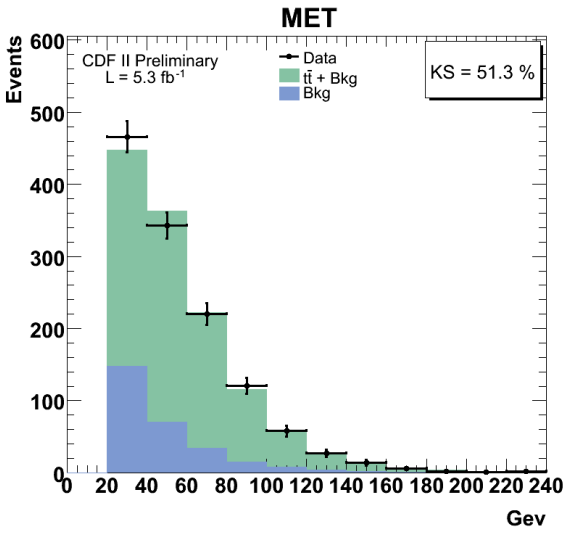
MET
CDF II Preliminary
L = 5.3 fb-1
Data
tt̄ + Bkg
Bkg
KS = 51.3 %
Events
Gev

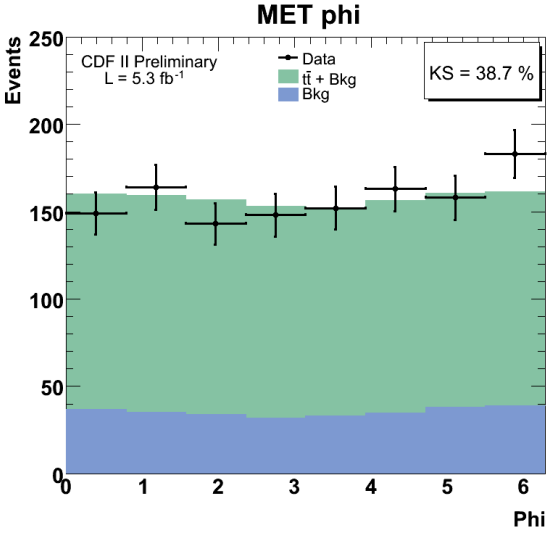
MET phi
CDF II Preliminary
L = 5.3 fb-1
Data
tt̄ + Bkg
Bkg
KS = 38.7 %
Events
Phi

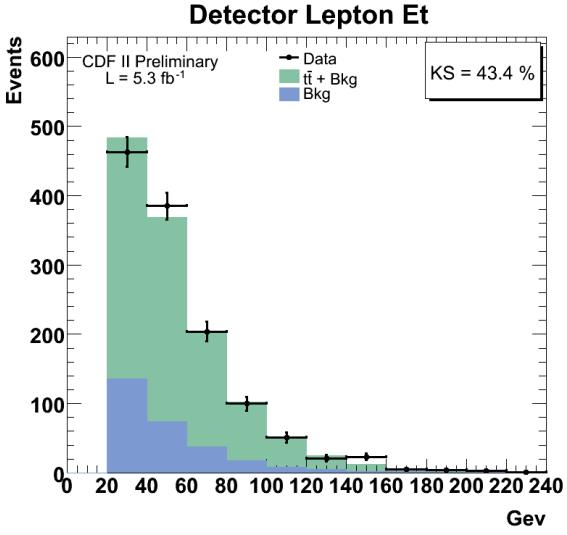
Detector Lepton Et
CDF II Preliminary
L = 5.3 fb-1
Data
tt̄ + Bkg
Bkg
KS = 43.4 %
Events
Gev

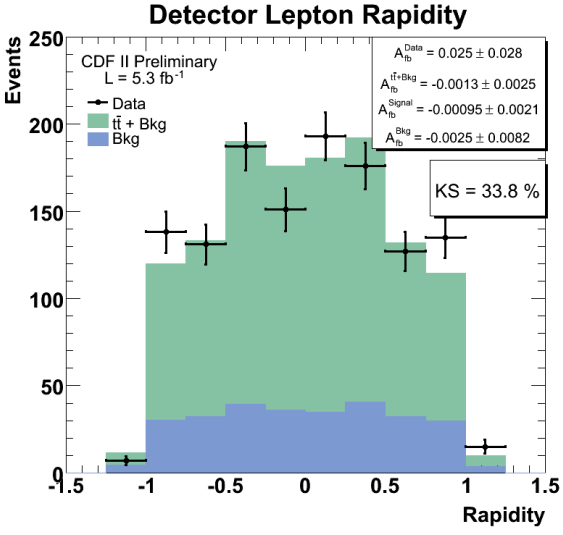
Detector Lepton Rapidity
CDF II Preliminary
L = 5.3 fb-1
Data
tt̄ + Bkg
Bkg
A_fb^Data = 0.025 ± 0.028
A_fb^tt̄+Bkg = -0.0013 ± 0.0025
A_fb^Signal = -0.00095 ± 0.0021
A_fb^Bkg = -0.0025 ± 0.0082
KS = 33.8 %
Events
Rapidity

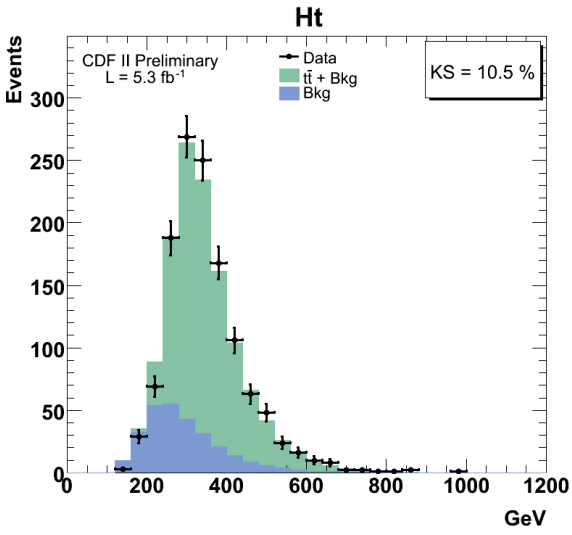
Ht
CDF II Preliminary
L = 5.3 fb-1
Data
tt̄ + Bkg
Bkg
KS = 10.5 %
Events
GeV

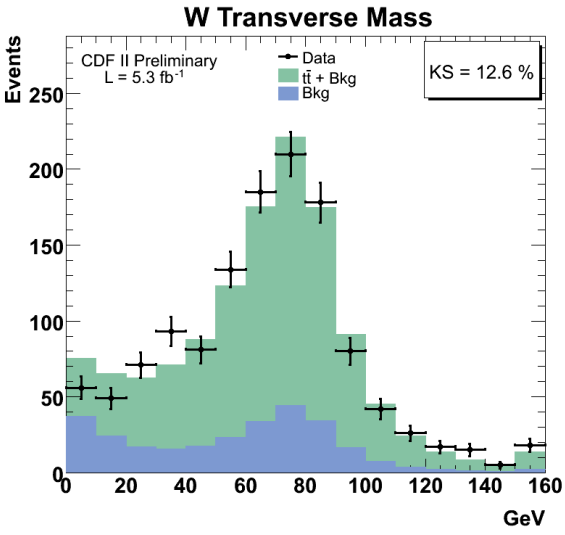
W Transverse Mass
CDF II Preliminary
L = 5.3 fb-1
Data
tt̄ + Bkg
Bkg
KS = 12.6 %
Events
GeV

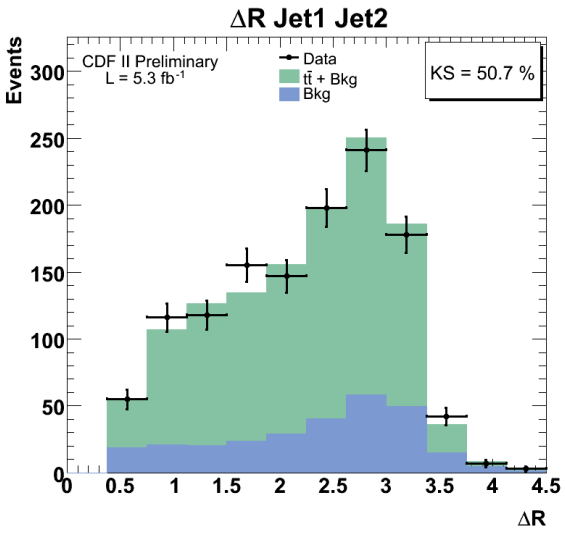
ΔR Jet1 Jet2
CDF II Preliminary
L = 5.3 fb-1
Data
tt̄ + Bkg
Bkg
KS = 50.7 %
Events
ΔR

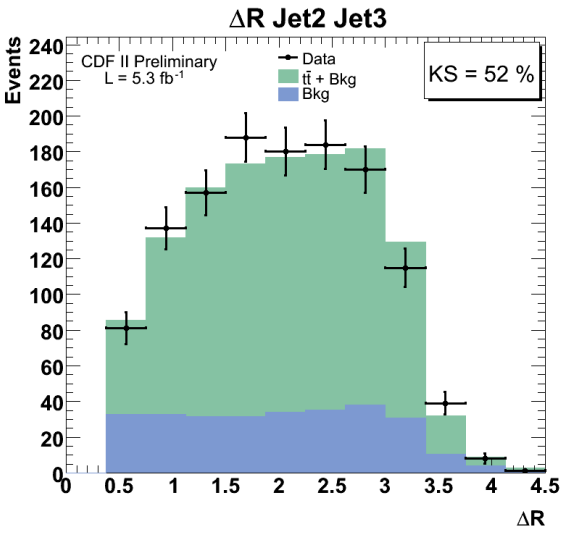
ΔR Jet2 Jet3
CDF II Preliminary
L = 5.3 fb-1
Data
tt̄ + Bkg
Bkg
KS = 52 %
Events
ΔR

5.2 Kinematic Fitter and Reconstructed Variables

In this section, we present plots comparing data and MC for variables reconstructed using the kinematic fitter. The $t\bar{t}$ semi-leptonic decay results in an up-quark jet, down-quark jet, b and $\bar{b}$ jets, a lepton, and neutrino. The kinematic fitter assigns the jets, lepton, and $\not\!\!E_T$ to these particles, as explained above in Section 3.2. We examine these plots to check the goodness of the kinematic fitter. We note from the χ^2 distribution in Figure 5.4 that our fitter does equally well reconstructing $t\bar{t}$ events from data as from MC, as the χ^2 distribution of the fitted events closely matches the shape of the background even out to the overflow bin at $\chi^2 \geq 90$. See Equation 3.1 and Section 3.2 for a complete explanation of the χ^2 variable and the kinematic fitter used for event reconstruction.

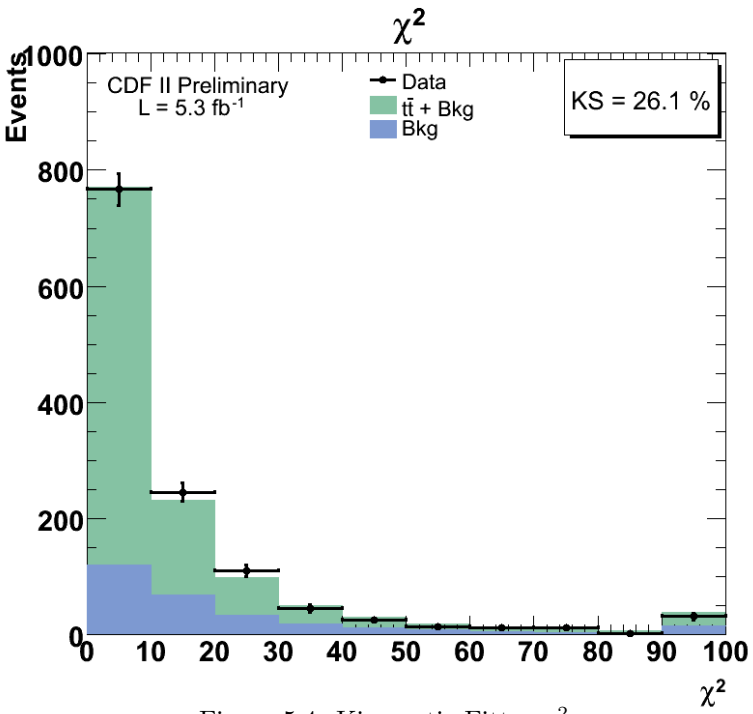

Figure 5.4: Kinematic Fitter χ^2

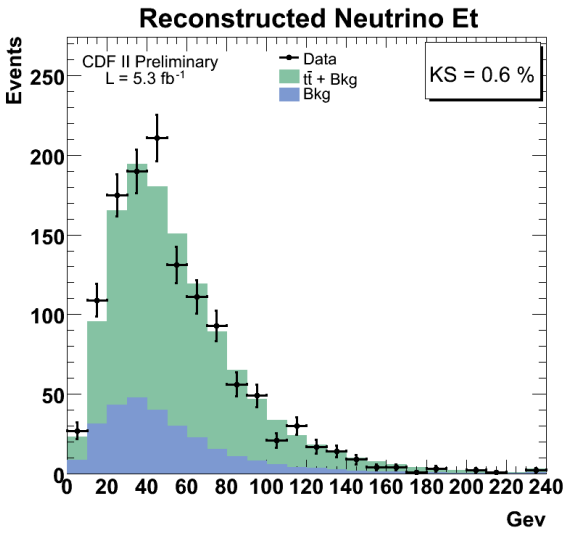
Reconstructed Neutrino Et
CDF II Preliminary
L = 5.3 fb-1
Data
tt̄ + Bkg
Bkg
KS = 0.6 %
Events
Gev

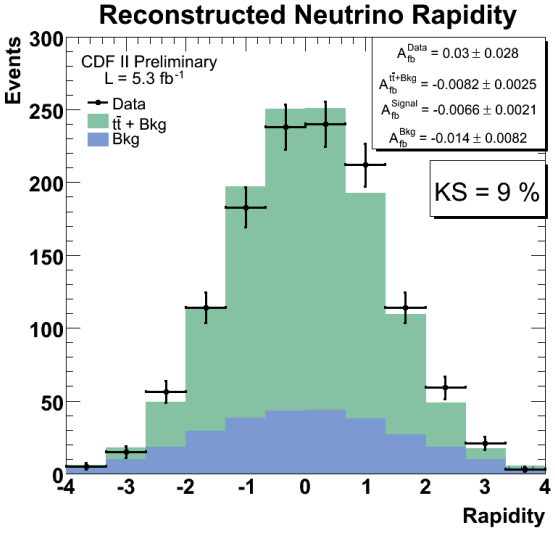
Reconstructed Neutrino Rapidity
CDF II Preliminary
L = 5.3 fb-1
Data
tt̄ + Bkg
Bkg
A_fb^Data = 0.03 ± 0.028
A_fb^tt̄+Bkg = -0.0082 ± 0.0025
A_fb^Signal = -0.0066 ± 0.0021
A_fb^Bkg = -0.014 ± 0.0082
KS = 9 %
Events
Rapidity

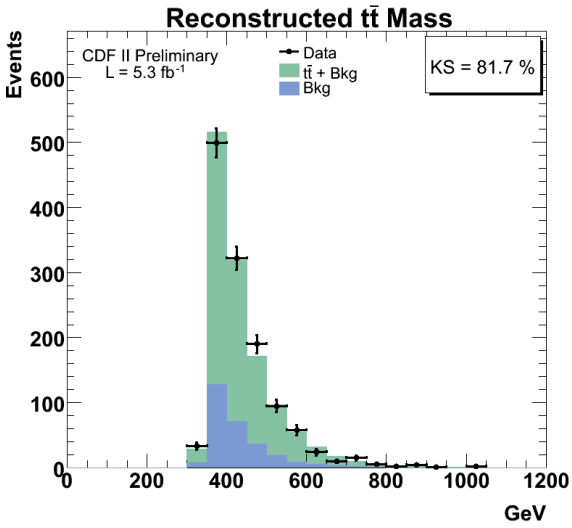
Reconstructed tt̄ Mass
CDF II Preliminary
L = 5.3 fb-1
Data
tt̄ + Bkg
Bkg
KS = 81.7 %
Events
GeV

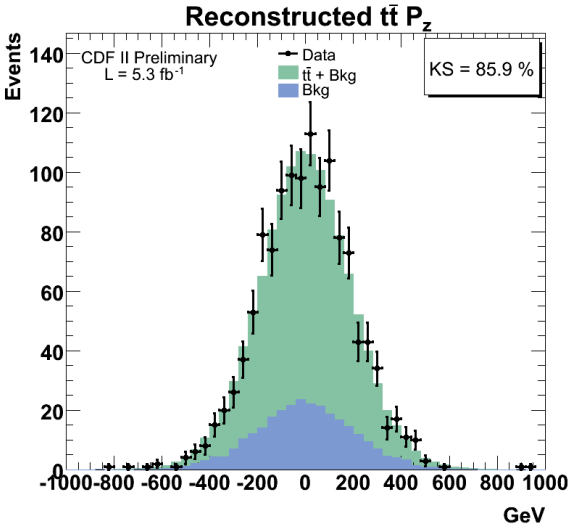
Reconstructed tt̄ Pz
CDF II Preliminary
L = 5.3 fb-1
Data
tt̄ + Bkg
Bkg
KS = 85.9 %
Events
GeV

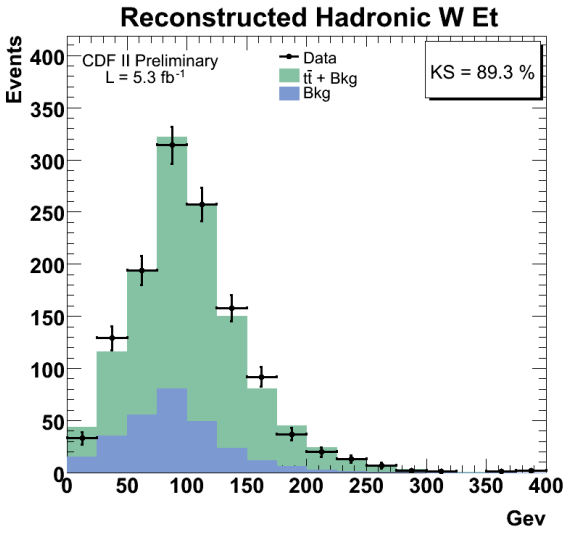
Reconstructed Hadronic W Et
CDF II Preliminary
L = 5.3 fb-1
Data
tt̄ + Bkg
Bkg
KS = 89.3 %
Events
Gev

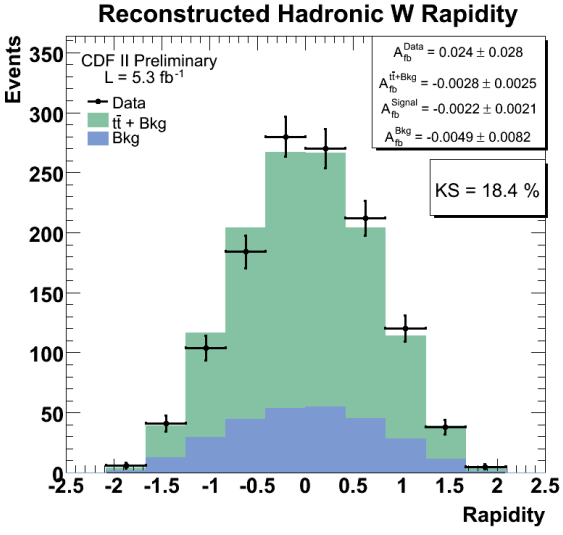
Reconstructed Hadronic W Rapidity
CDF II Preliminary
L = 5.3 fb-1
Data
tt̄ + Bkg
Bkg
A_fb^Data = 0.024 ± 0.028
A_fb^tt̄+Bkg = -0.0028 ± 0.0025
A_fb^Signal = -0.0022 ± 0.0021
A_fb^Bkg = -0.0049 ± 0.0082
KS = 18.4 %
Events
Rapidity

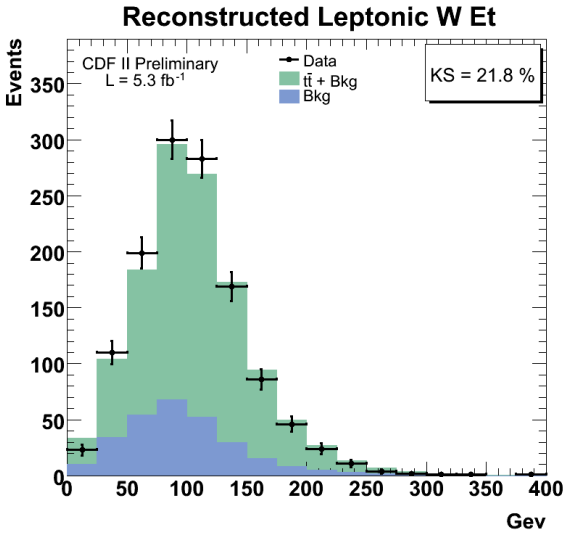
Reconstructed Leptonic W Et
CDF II Preliminary
L = 5.3 fb-1
Data
tt̄ + Bkg
Bkg
KS = 21.8 %
Events
Gev

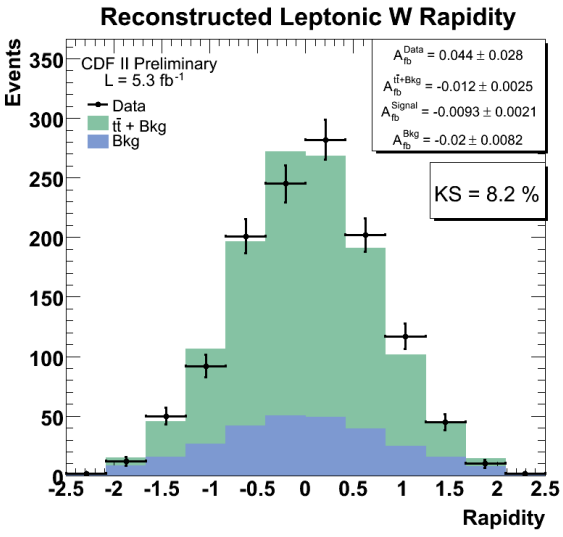
Reconstructed Leptonic W Rapidity
CDF II Preliminary
L = 5.3 fb-1
Data
tt̄ + Bkg
Bkg
A_fb^Data = 0.044 ± 0.028
A_fb^tt̄+Bkg = -0.012 ± 0.0025
A_fb^Signal = -0.0093 ± 0.0021
A_fb^Bkg = -0.02 ± 0.0082
KS = 8.2 %
Events
Rapidity

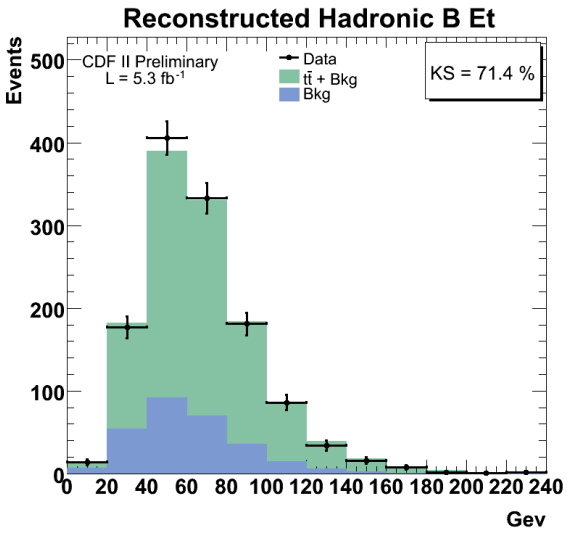
Reconstructed Hadronic B Et
CDF II Preliminary
L = 5.3 fb-1
Data
tt̄ + Bkg
Bkg
KS = 71.4 %
Events
Gev

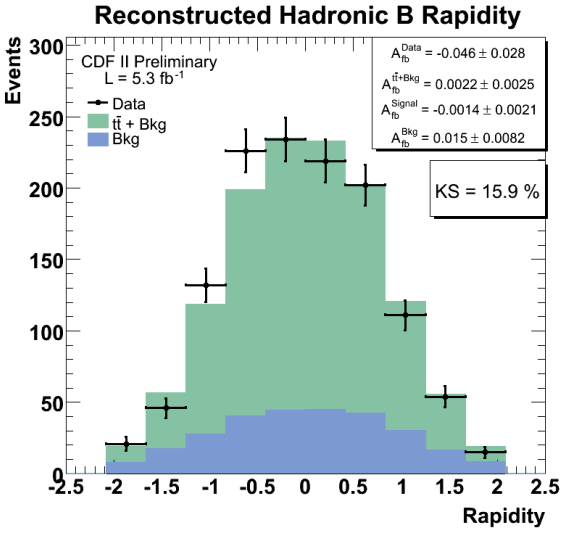
Reconstructed Hadronic B Rapidity
CDF II Preliminary
L = 5.3 fb-1
Data
tt̄ + Bkg
Bkg
A_fb^Data = -0.046 ± 0.028
A_fb^tt̄+Bkg = 0.0022 ± 0.0025
A_fb^Signal = -0.0014 ± 0.0021
A_fb^Bkg = 0.015 ± 0.0082
KS = 15.9 %
Events
Rapidity

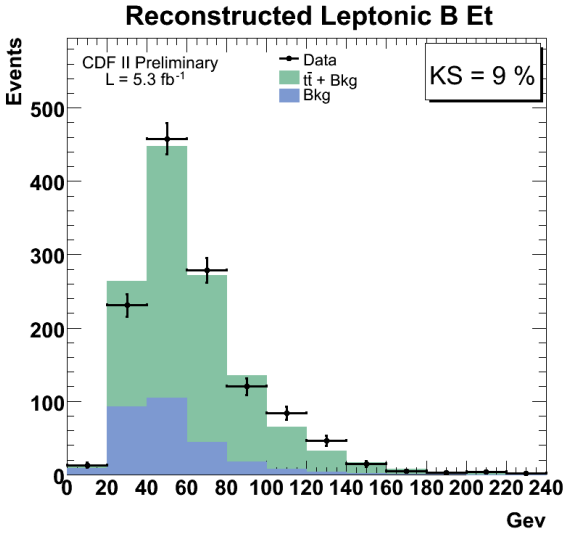
Reconstructed Leptonic B Et
CDF II Preliminary
L = 5.3 fb-1
Data
tt̄ + Bkg
Bkg
KS = 9 %
Events
Gev

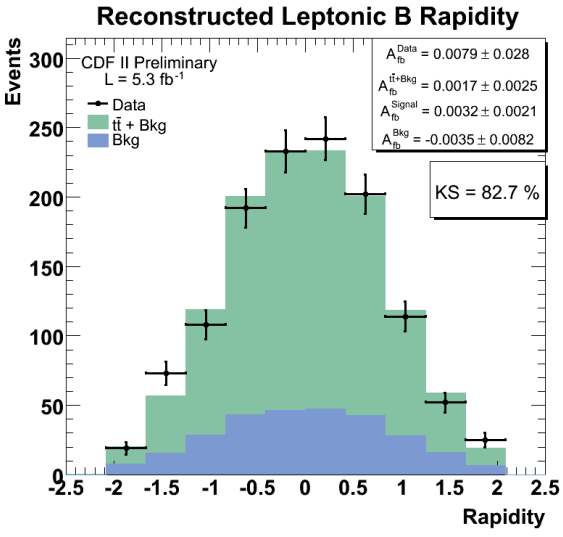
Reconstructed Leptonic B Rapidity
CDF II Preliminary
L = 5.3 fb-1
Data
tt̄ + Bkg
Bkg
A_fb^Data = 0.0079 ± 0.028
A_fb^tt̄+Bkg = 0.0017 ± 0.0025
A_fb^Signal = 0.0032 ± 0.0021
A_fb^Bkg = -0.0035 ± 0.0082
KS = 82.7 %
Events
Rapidity

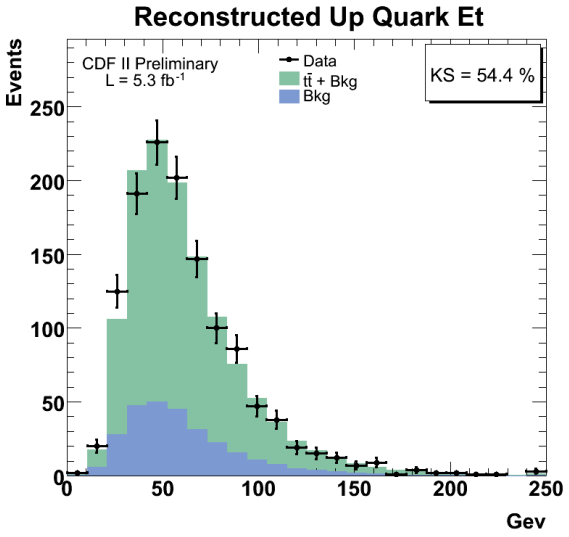
Reconstructed Up Quark Et
CDF II Preliminary
L = 5.3 fb-1
Data
tt̄ + Bkg
Bkg
KS = 54.4 %
Events
Gev

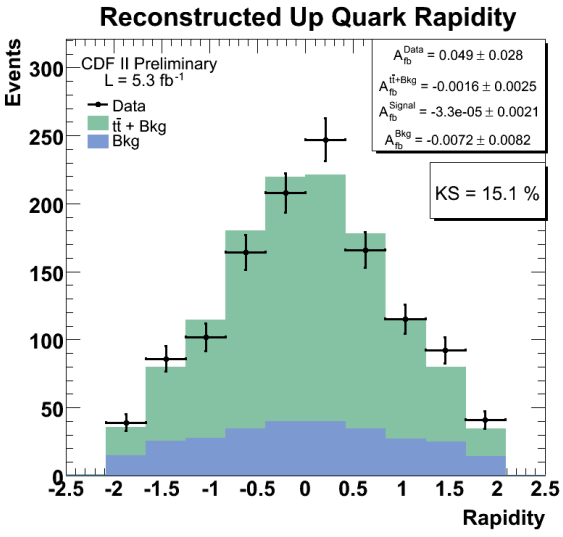
Reconstructed Up Quark Rapidity
CDF II Preliminary
L = 5.3 fb-1
Data
tt̄ + Bkg
Bkg
A_fb^Data = 0.049 ± 0.028
A_fb^tt̄+Bkg = -0.0016 ± 0.0025
A_fb^Signal = -3.3e-05 ± 0.0021
A_fb^Bkg = -0.0072 ± 0.0082
KS = 15.1 %
Events
Rapidity

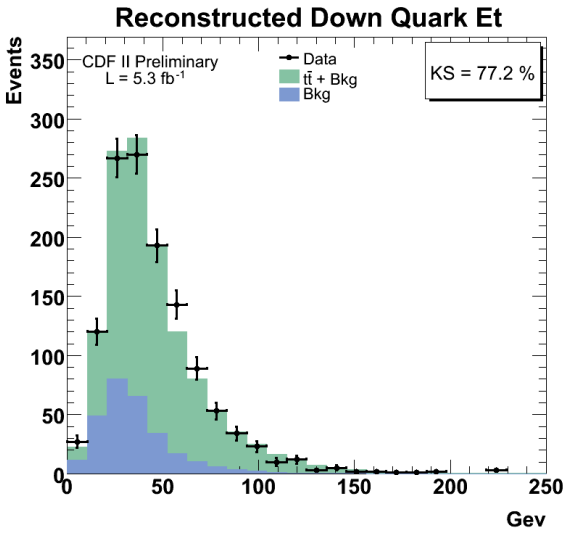
Reconstructed Down Quark Et
CDF II Preliminary
L = 5.3 fb-1
Data
tt̄ + Bkg
Bkg
KS = 77.2 %
Events
Gev

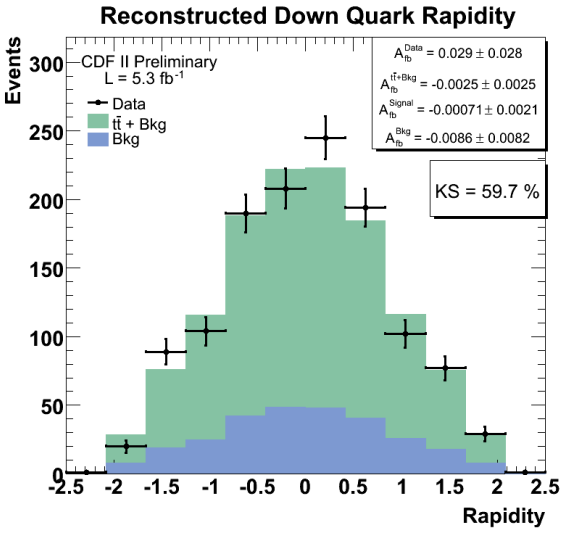
Reconstructed Down Quark Rapidity
CDF II Preliminary
L = 5.3 fb-1
Data
tt̄ + Bkg
Bkg
A_fb^Data = 0.029 ± 0.028
A_fb^tt̄+Bkg = -0.0025 ± 0.0025
A_fb^Signal = -0.00071 ± 0.0021
A_fb^Bkg = -0.0086 ± 0.0082
KS = 59.7 %
Events
Rapidity

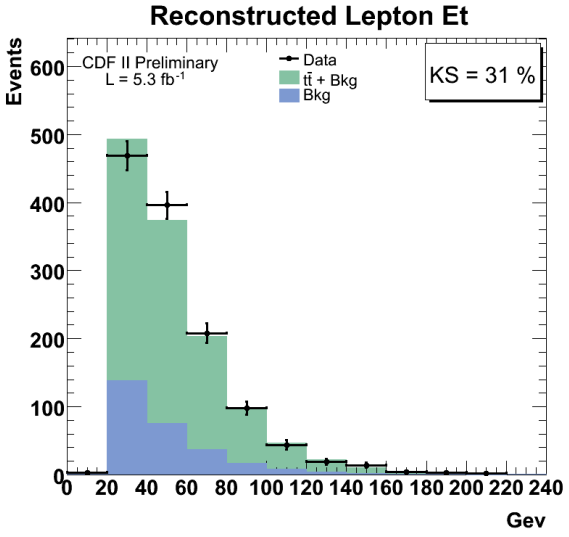
Reconstructed Lepton Et
CDF II Preliminary
L = 5.3 fb-1
Data
tt̄ + Bkg
Bkg
KS = 31 %
Events
Gev

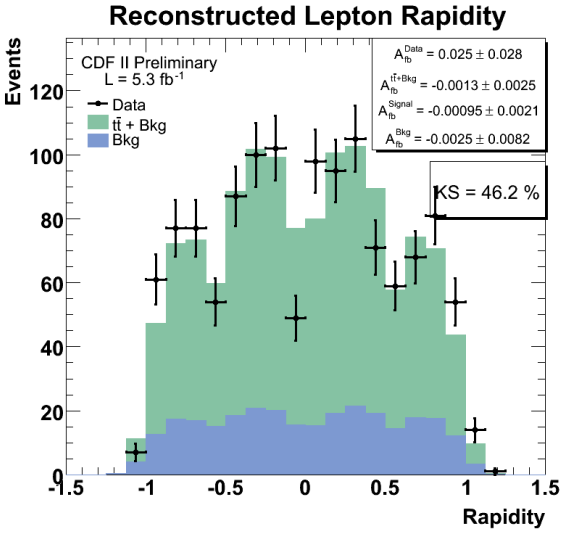
Reconstructed Lepton Rapidity
CDF II Preliminary
L = 5.3 fb-1
Data
tt̄ + Bkg
Bkg
A_fb^Data = 0.025 ± 0.028
A_fb^tt̄+Bkg = -0.0013 ± 0.0025
A_fb^Signal = -0.00095 ± 0.0021
A_fb^Bkg = -0.0025 ± 0.0082
KS = 46.2 %
Events
Rapidity

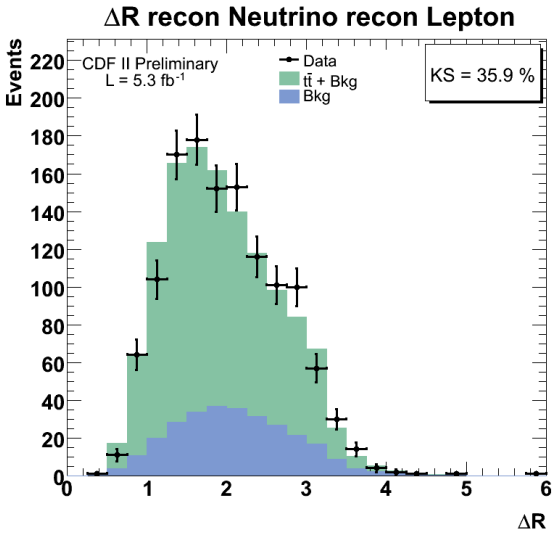
ΔR recon Neutrino recon Lepton
CDF II Preliminary
L = 5.3 fb-1
Data
tt̄ + Bkg
Bkg
KS = 35.9 %
Events
ΔR

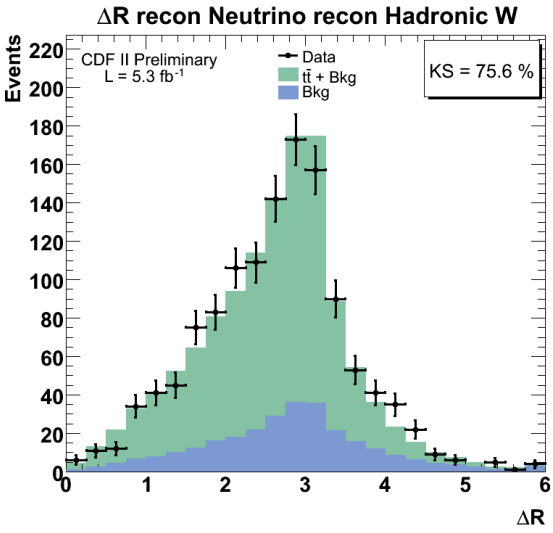
ΔR recon Neutrino recon Hadronic W
CDF II Preliminary
L = 5.3 fb-1
Data
tt̄ + Bkg
Bkg
KS = 75.6 %
Events
ΔR

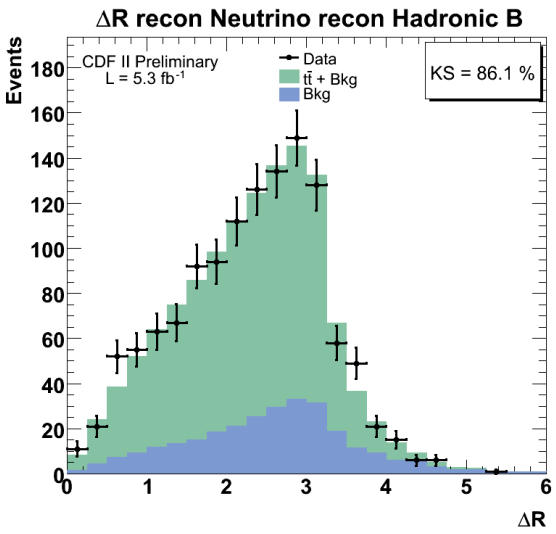
ΔR recon Neutrino recon Hadronic B
CDF II Preliminary
L = 5.3 fb-1
Data
tt̄ + Bkg
Bkg
KS = 86.1 %
Events
ΔR

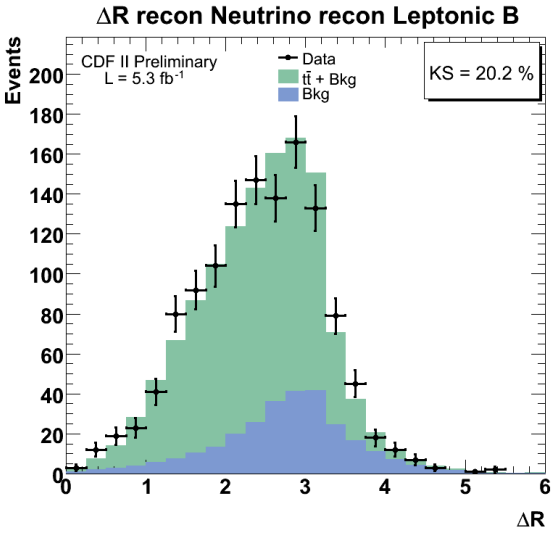
ΔR recon Neutrino recon Leptonic B
CDF II Preliminary
L = 5.3 fb-1
Data
tt̄ + Bkg
Bkg
KS = 20.2 %
Events
ΔR

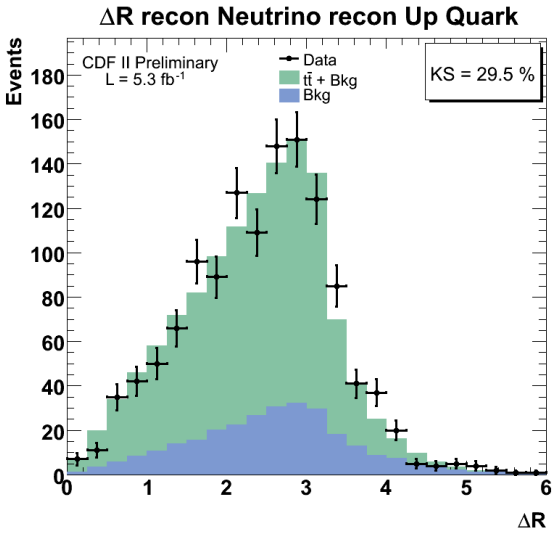
ΔR recon Neutrino recon Up Quark
CDF II Preliminary
L = 5.3 fb-1
Data
tt̄ + Bkg
Bkg
KS = 29.5 %
Events
ΔR

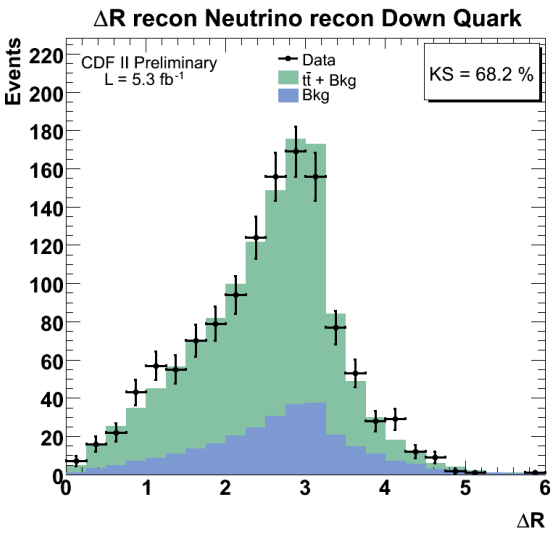
ΔR recon Neutrino recon Down Quark
CDF II Preliminary
L = 5.3 fb-1
Data
tt̄ + Bkg
Bkg
KS = 68.2 %
Events
ΔR

Chapter 6.

Data Asymmetry and Cross-checks

Having validated our detector data and reconstructed variables from the kinematic fitter, we are now ready to investigate our -q·y_{had} and qΔy distributions and measure our (uncorrected) A_{fb} values in the lab and $t\bar{t}$ frames as they are directly observed. We will see that there is an observed asymmetry that is CP-invariant in this raw data, before any corrections are made, suggesting that this effect is caused by physics and not by an artifact of our event selection, reconstruction, or correction techniques.

Once we have established that there is an asymmetry in the raw data, we then validate the data in Section 6.2 by making measurements of the raw A_{fb} values of subsets of the data, checking if the A_{fb} is a result of the kinematic fitter or event selection.

6.1 The Charge Asymmetry

First, let us briefly examine the reconstructed y_{had} and Δy distributions before multiplying by the lepton charge of the event. We see in Figure 6.1 that these distributions are completely symmetric, with A_{fb} values statistically consistent with 0, just as we expect from our signal+background model.

Next, let us look at the reconstructed y_{had} distribution, *separated by the lepton charge*, as shown in Figure 6.2. Charge separated data for the Δy variable is similarly shown in Figure 6.3, and Table 6.1 shows the raw A_{fb} of these distributions. These data shapes for each lepton charge are roughly reflections

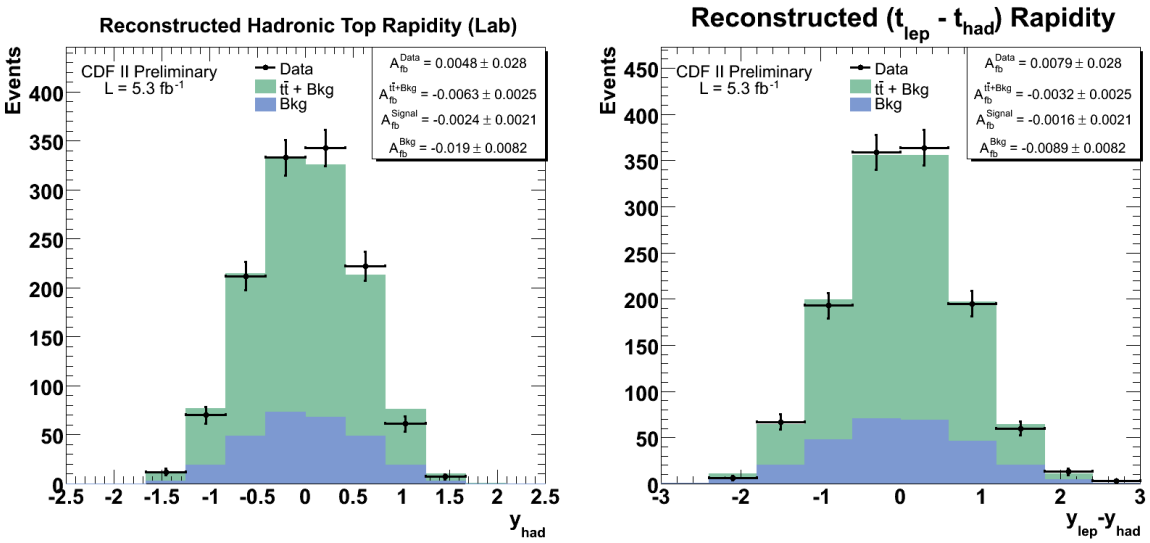

Figure 6.1: y_{had} and Δy distributions

about $y = 0$, and their A_{fb} values are significantly non-zero, similar to each other in magnitude, but opposite in sign. If we were to take events from one of these distributions, switch the charges of all particles, and reverse the momenta of all particles (just as the physics observed in a mirror image is "flipped"), we would see that the modified distributions of $-q \cdot y_{had}$ or $q\Delta y$ for one charge now would appear to match the other charge distribution. This flipping of charges is called "charge symmetry" (abbreviated as C), and mirror-flipping particle momenta is called "parity symmetry" (abbreviated as P). Thus we say that the separated positive and negative lepton plots of y_{had} and Δy are *CP-invariant*. This is indicative that the y_t distribution is indeed asymmetric, and in a *CP-invariant way*, with the top and anti-top asymmetries equal in magnitude but different in sign. This CP-invariance suggests that the observed asymmetries are caused by physics processes and are not merely statistical fluctuations. That is, because the positive and negative lepton subsamples are statistically independent, if the asymmetries were a statistical fluctuation we would expect to see different values for the charge-separated y_t distributions. The charge of the lepton is not used by the χ^2 kinematic fitter during event reconstruction, so the significant dependence of the asymmetry on charge suggests that the asymmetry is real, not a statistical fluctuation.

If CP is a good symmetry, then we can combine the charge-separated distributions into a single distribution by multiplying each event by a term proportional to the lepton charge, q_{lepton}. We described this technique and combined

charge	$A_{fb}^{-q\cdot y_{had}}$	$A_{fb}^{q\Delta y}$
positive (no q weight)	-0.0701 ± 0.0403	-0.0669 ± 0.0403
negative (no q weight)	0.0757 ± 0.0392	0.0479 ± 0.0393
total	0.0730 ± 0.0281	0.0571 ± 0.0281

Table 6.1: Raw A_{fb} for the $-q\cdot y_{had}$ and $q\Delta y$ distributions
see Table 6.5 for full breakdown

distributions in Section 1.8. Using this method, we combine the charge-separate plots into the primary distributions used in the remainder of our analysis, shown in Figure 6.4. We find the A_{fb} value for $-q\cdot y_{had}$ to be $A_{fb}^{-q\cdot y_{had}} = A_{fb}^{p\bar{p}} = 0.073 \pm 0.028$ and for the $q\Delta y$ variable, $A_{fb}^{q\Delta y} = A_{fb}^{t\bar{t}} = 0.057 \pm 0.028$. These A_{fb} values are large and significantly from 0. We also note that they are also larger than the NLO QCD predictions, as discussed in Section 1.7. The KS-test values (method described in Chapter 5) for these combined distributions are also quite low (0% for $-q\cdot y_{had}$ and 2% for $q\Delta y$), again underlining the statistcal significance of the observed distributions.

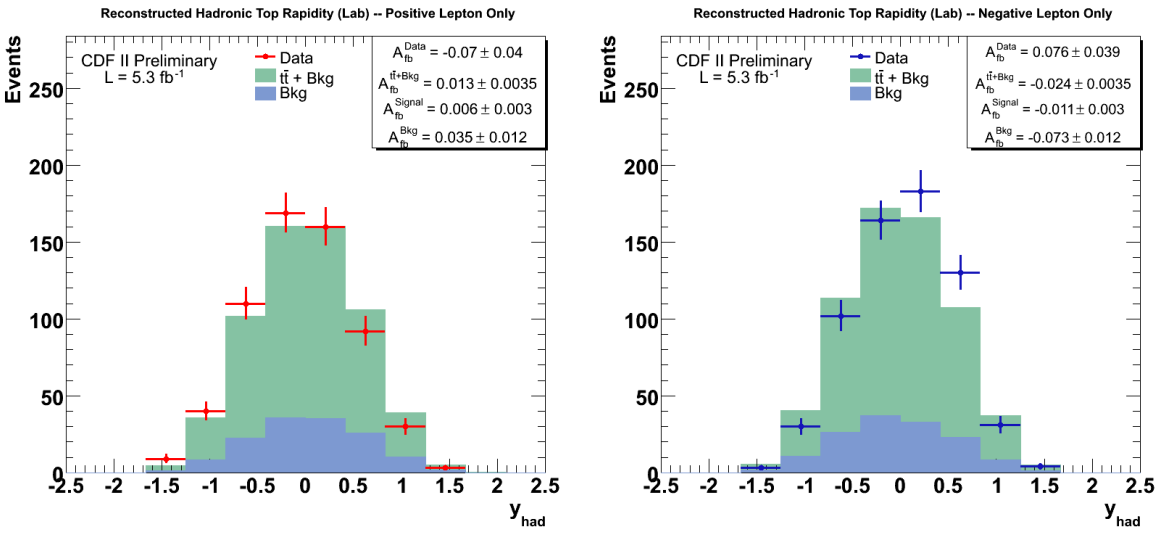

Figure 6.2: y_{had} distributions by lepton charge
Note that the A_{fb} values for these plots are similar in magnitude and differ in sign.
The top signal areas have been renormalized for each lepton shape, so bkg+sig has same area as data.

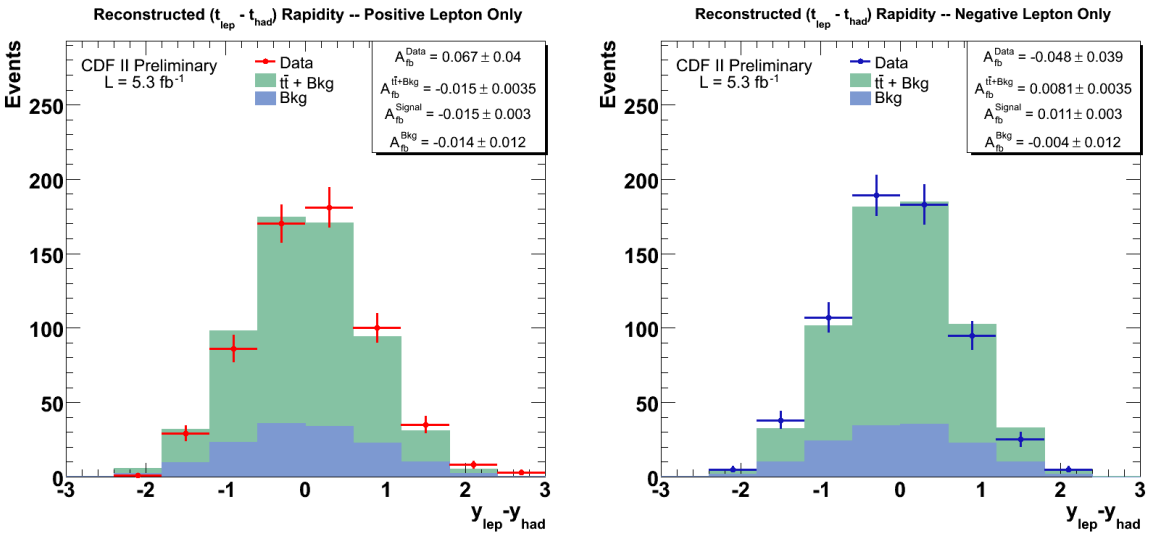

Figure 6.3: Δy distributions by lepton charge
Note again that the A_{fb} values for these plots differ in sign.

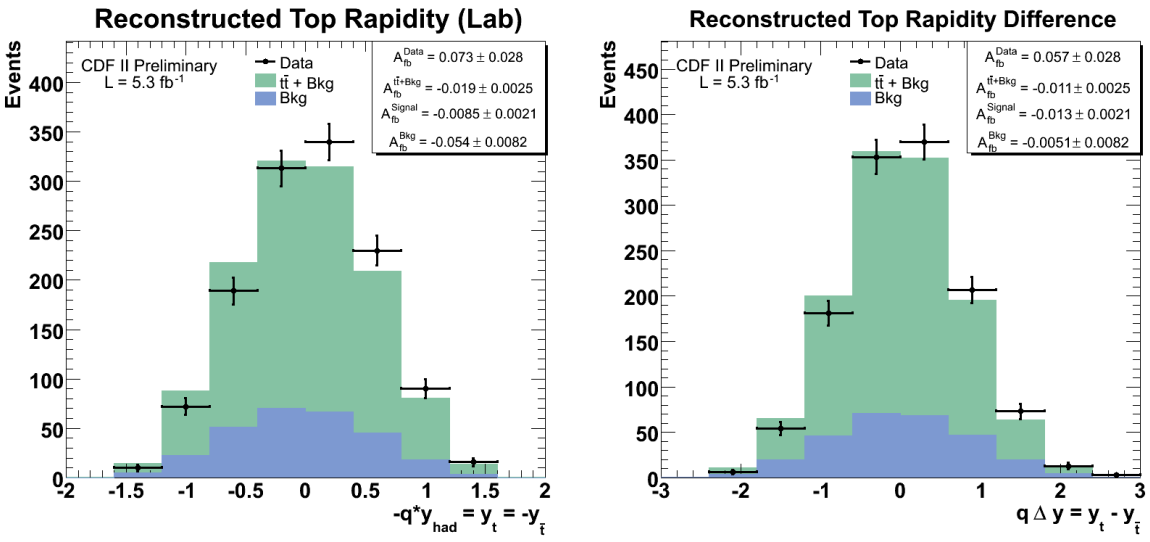

Figure 6.4: -q·y_{had} and qΔy distributions

6.2 Cross Checks of Data Subsets

We now examine the stability and robustness of the inclusive asymmetries against simple variations of the selection and reconstruction. A proper comparison of a real $t\bar{t}$ effect across these selections should employ a background subtraction in order to establish a pure $t\bar{t}$ signal. But because we wish to avoid any assumptions at this stage, we perform these cross-checks using the inclusive lepton+jets data. For each selection or reconstruction variation, we look at both asymmetries, $A_{fb}^{-q\cdot y_{had}}$ and $A_{fb}^{q\Delta y}$ (A_{fb}^{lab} and $A_{fb}^{t\bar{t}}$). A summary of all the results is given in Section 6.3, and values summarized in Table 6.5.

6.2.1 Frame

Row 1 shows the inclusive asymmetry in the two frames. The ratio in the data is $A_{fb}^{t\bar{t}}/A_{fb}^{lab} = 1.05 \pm 0.60$, where the uncertainty assumes the asymmetries are independent, and is therefore an over-estimate. In the Madgraph Axigluon coloron sample $t\bar{t}$ctopoa, we find $A_{fb}^{t\bar{t}}/A_{fb}^{lab} = 1.56 \pm 0.14$ from corrected reconstructed values and 1.41 ± 0.02 from truth. The data ratio is smaller than these predictions but compatible within uncertainties.

6.2.2 χ^2

Rows 4-5 show the asymmetries when the data is partitioned by a cut on the reconstruction quality at $\chi^2 = 9.0$, the value established and used in the

top mass analysis. As seen in Figure 5.4, this cut restricts the sample to the peak in the distribution. There are 725 events out of 1260 with $\chi^2 \leq 9$. In this high quality reconstruction sample, $A_{fb}^{t\bar{t}}$ is diminished to 1σ significance, but A_{fb}^{lab} grows in significance. Both values are statistically compatible with the result in the full sample. We will keep an eye on the χ^2 in $A_{fb}^{t\bar{t}}$ but the data seem to suggest that the asymmetry is not associated with bad reconstructions that show up as large χ^2.

6.2.3 Run Range

Rows 6-7 show the asymmetries when the data is divided into an early and a later part. We see that $A_{fb}^{t\bar{t}}$ is relatively stable, but in the newer data, A_{fb}^{lab} drops significantly. However, the stability of the former values might suggest that the latter is a downward fluctuation. The A_{fb} values in the two data periods are consistent within 2σ.

asymmetry	all data	early data (3.4 fb^{-1})	update (2.1 fb^{-1})
$A_{fb}^{t\bar{t}}$	$+0.057 \pm 0.028$	$+0.071 \pm 0.036$	$+0.035 \pm 0.046$
$A_{t\bar{t}}^{+}$	-0.067 ± 0.040	$+0.095 \pm 0.053$	-0.030 ± 0.061
$A_{t\bar{t}}^{-}$	$+0.048 \pm 0.039$	-0.051 ± 0.048	$+0.041 \pm 0.068$
A_{fb}^{lab}	$+0.073 \pm 0.028$	$+0.104 \pm 0.036$	$+0.023 \pm 0.046$
A_{lab}^{+}	-0.070 ± 0.040	-0.130 ± 0.053	$+0.008 \pm 0.061$
A_{lab}^{-}	$+0.076 \pm 0.043$	$+0.084 \pm 0.048$	$+0.060 \pm 0.068$

Table 6.2: The inclusive and charged asymmetries in all, early, and later data

Charge components

The signed asymmetries are shown for the two data periods in Table 6.2. Within the largish statistical uncertainty of the latter data, the $A_{fb}^{t\bar{t}}$ charge components are self-consistent and stable across the datasets. In A_{fb}^{lab} we see that the A_{lab}^{-} for negative leptons is stable across the datasets, but that the latter data has a wrong sign in A_{lab}^{+}. This leads to the null in the total A_{fb}^{lab} for the latter data. Interestingly, opposing contributions in the early and later data combine to give an inclusive A_{lab}^{+} that is in very good agreement with the inclusive A_{lab}^{-}. We will not conjecture further on this – it is possible to over-think these things.

Time series

In order to monitor the integrity of dataset for this analysis, we have calculated the asymmetries separately in each of the standard CDF data periods

and studied the trends. The top row of Figure 6.5 shows the two asymmetries as measured separately for various time periods of CDF data-taking. For the time axis variable, we use the total number of b-tagged events in the inclusive sample, which roughly correlates to the integrated luminosity. This plot shows trends in all tagging categories: pretags are in black, tags are in blue, double tags are in green, and anti-tags are in red. The double tags show large fluctuations consistent with the smaller sample. A very correlated downward fluctuation in all categories, driven by the pretag value, is seen in one of the periods and is probably a main ingredient in the differences between early 3.2 fb^{-1} and our cumulative 5.3 fb^{-1} sample.

The cumulative asymmetries are shown in the bottom row of Figure 6.5. The $A_{\text{fb}}^{t\bar{t}}$ asymmetry seems to be converging to values near +5% for all tag categories. The $A_{\text{fb}}^{\text{lab}}$ trends show the negative asymmetry in the background dominated anti-tags (dominated by electroweak processes like $Wb\bar{b}$), the positive asymmetry in the tags (dominated by $t\bar{t}$), and their net of almost zero asymmetry in the pre-tag sample. The trend in the double tags is probably the result of small statistics early in the Run, but could also be part of the general "double-tag problem" which will be discussed in Sec. 6.2.6, along with other observations about asymmetries across the b-tagging selections.

The cumulative significance of the asymmetries is shown in Figure 6.6. If the effect is real, we expect the significance to grow as $\sqrt{N}$. In fact,

$$\text{Significance} = \frac{A}{\sigma(A)} = \frac{A}{\sqrt{1-A^2}}\sqrt{N} \tag{6.1}$$

so that the scaling curve is normalized by the size of the asymmetry. Here we are most interested in the significance in the tagged sample. On each plot we show the best fit curve of the form $\sqrt{N}$ to the tagged data. The $\sqrt{N}$ curve is a good representation of the significance and we can use the normalization in fits Figure 6.6 as an alternate derivation of the ensemble asymmetry. The results are shown in Table 6.3. The fit means are in good agreement with the means in the data (the unphysical fit uncertainties are due to neglect of the uniform statistical errors on the significance).

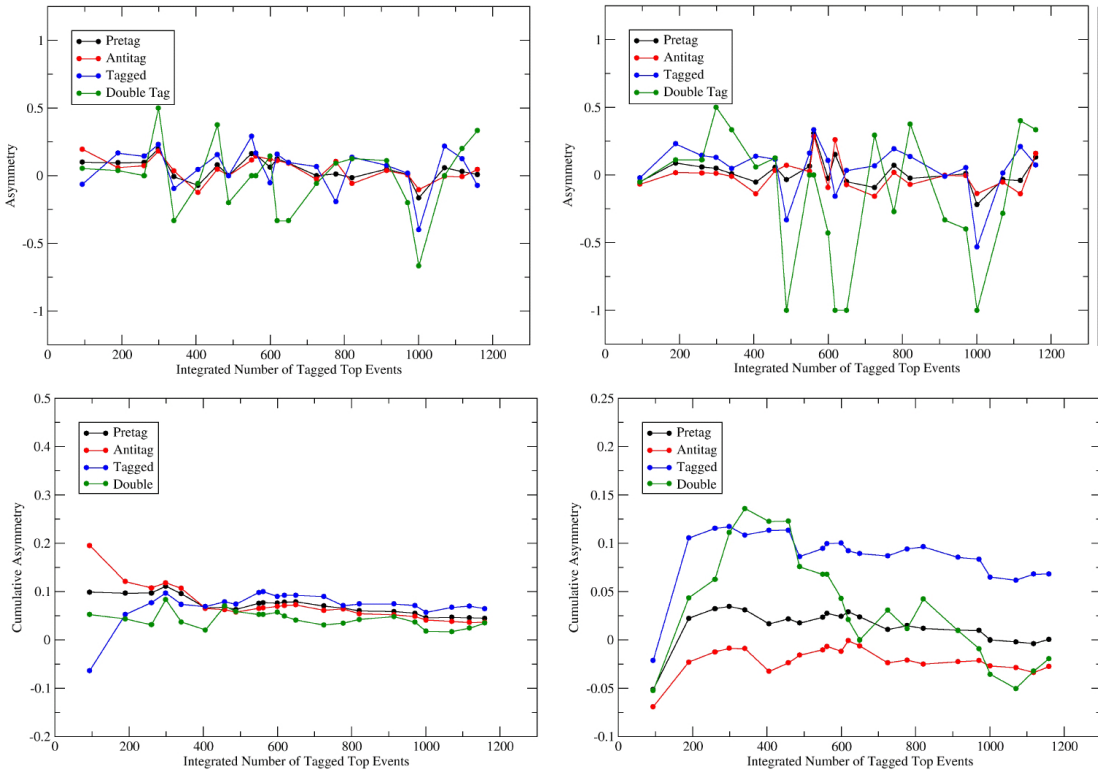

Figure 6.5: Top: Each point is the $A_{fb}^{t\bar{t}}$ (left) and A_{fb}^{lab} (right) for a CDF data period. Bottom: cumulative values for same variables as a function of data period.

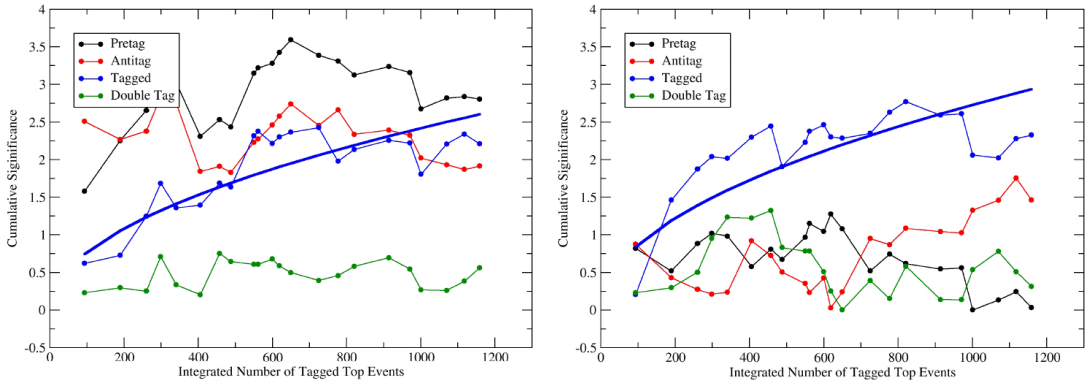

Figure 6.6: Significance of $A_{fb}^{t\bar{t}}$ (left) and A_{fb}^{lab} (right) for each data period.

	A_{fb}^{lab}	$A_{fb}^{t\bar{t}}$
data	0.075 ± 0.030	0.070 ± 0.030
fit	0.085 ± 0.004	0.076 ± 0.004

Table 6.3: Inclusive asymmetries from the ensemble average and from the fit to the $\sqrt{N}$ hypothesis for the significance.

6.2.4 Triggers

The rows "CEM,CMUP,CMX" show the asymmetry measured separately for each one of our trigger lepton types. The fluctuations across the trigger types are large, but the values are all consistent within error.

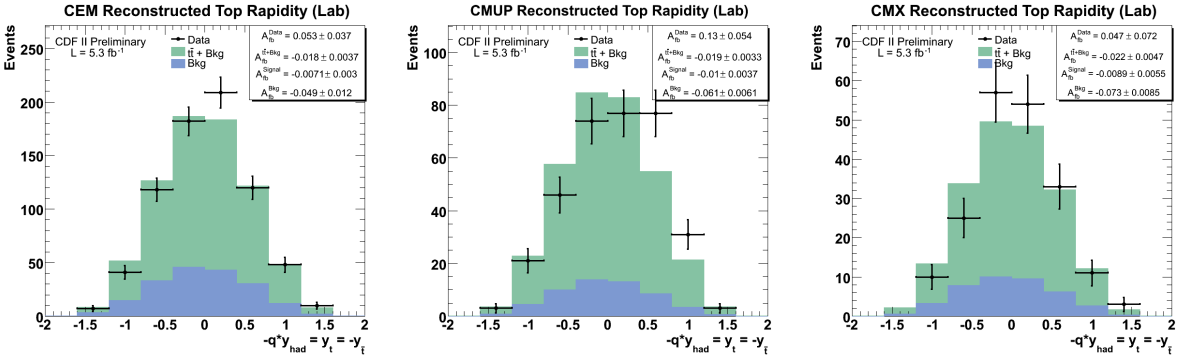

Figure 6.7: $-q \cdot y_{had}$ split for CEM, CMUP, and CMX lepton events

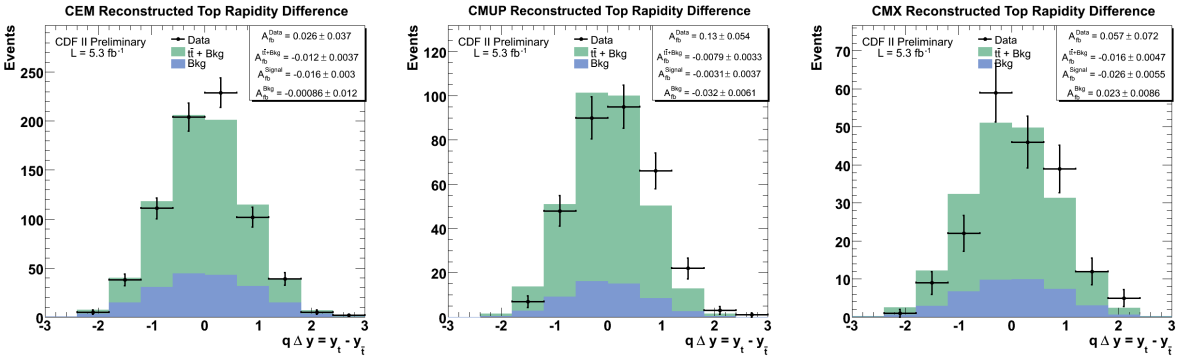

Figure 6.8: $q\Delta y$ split for CEM, CMUP, and CMX lepton events

6.2.5 Jet Multiplicity

Recall that the NLO QCD asymmetry is the sum of a positive asymmetry in exclusive 4-jet events and a negative asymmetry in events with gluon radiation. In MCFM, restricting the sample to 4-jets almost doubles the asymmetry. Rows 11-12 show the two asymmetries in data samples partitioned according to the presence of an extra jet. The "4-jet" sample requires exactly 4 tight jets (no

other jets with energy ¿20 GeV), has 939 events, and asymmetries of 0.0756 ± 0.0325 and 0.0650 ± 0.0326 for $-q \cdot y_{had}$ and $q\Delta y$, respectively. The "5-jet" sample is actually 5-or-more tight jets, and has 321 events, and asymmetries of 0.0654 ± 0.0557 and 0.0343 ± 0.0558 for $-q \cdot y_{had}$ and $q\Delta y$, respectively. The 4-jet vs. 5-jet asymmetries are marginally consistent within the large uncertainties. The jet multiplicity dependence is in the direction of the NLO effect, but weaker: in 4-jets, the asymmetry increases, but it is not doubled, while for 5-jets, we see that the asymmetry is reduced, but we note that it is not negative. See Figures 6.9 and 6.10 for plots.

6.2.6 B-tagging

Rows 13-15 of Table 6.5 show the behavior of the asymmetries under different b-tagging selections. In row 15, we find that the asymmetries in the double-tags are very small. The asymmetry in the single-tags is then correspondingly larger than the full inclusive result. The single tags and double tags are barely statistically compatible, and the double tags still seem suggestively small. The double tags have very small backgrounds and, owing to the identification of both b-jets, very good accuracy in parton-jet assignment. The obvious hypothesis is that there is no real asymmetry, and some issue with backgrounds or b-jets in the reconstruction is creating a false asymmetry in the single tags. This is one of the biggest mysteries in these studies.

Perhaps the single-tag result is somehow due to the treatment of single b-jets in the reconstruction. This is already somewhat disfavored by the results of the charge-separated distributions, shown and explained in Section 6.1: why would the sign of a pull from a mis-identified b-jet depend on the lepton sign which is not used anywhere in the calculation? As an additional check we can look at the results when we use the lowest χ^2 reconstruction solution *without* the requirement that b-tags are associated with b-partons. We impose an additional cut on χ^2 to reject difficult-to-reconstruct events, so that the final number of accepted events is close to our normal data sample size of 1260. We find a cut at $\chi^2 < 3$ works well for this. The results in all tag selection categories, shown in Table 6.4, are very close to asymmetries found when b-tag consistency is required, suggesting that the asymmetry is not arising from any kind of bias associated with assigning b-tagged jets to the b-quarks.

The other special feature of double tagged events is an acceptance restriction: both b-jets must have $|\eta| < 1.0$. It is conceivable that some aspect of the

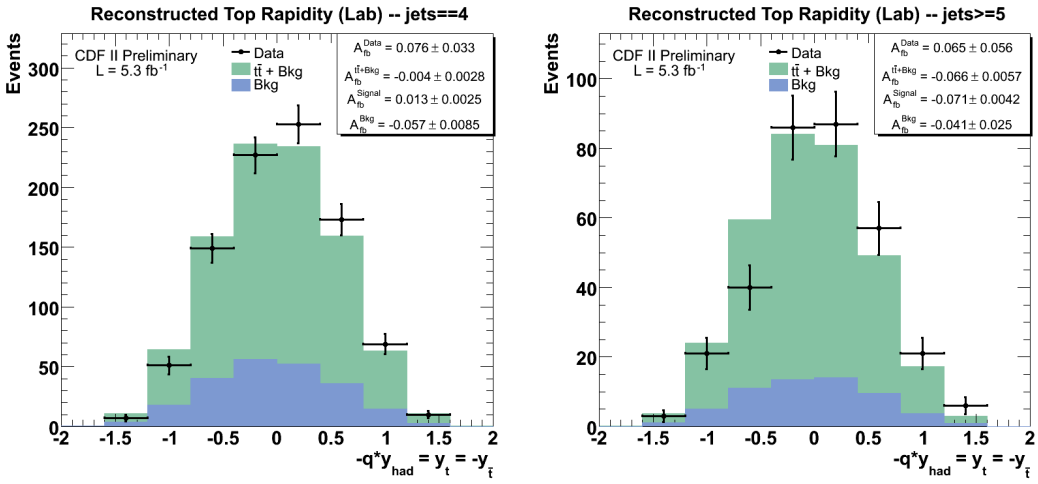

Figure 6.9: -q·y_{had} split by nJets

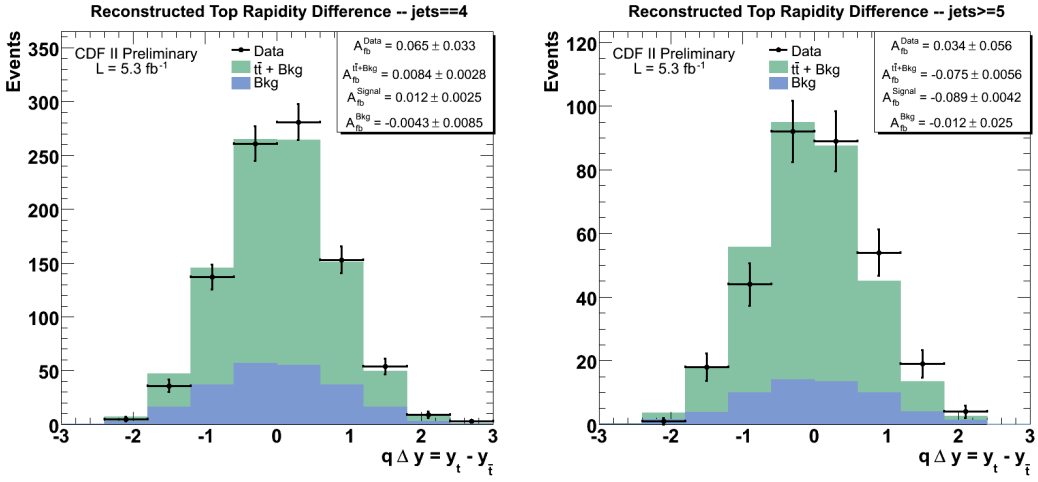

Figure 6.10: qΔy split by nJets

asymmetry disfavors 2 central b-jets, and it therefore cannot be seen in that selection. Our one cherry-picked physics model does not show this however: in the Madgraph coloron sample $t\bar{t}$ctopoa, the double-tags there have very similar asymmetries to the single tags. The lack of asymmetry in the double tagged data sample remains mysterious. It is definitely a concern, but it is at least historical, since we've noticed this deficiency for some time over many periods of data. Maybe more importantly, it has also been observed in the recent DØ results [6]. Our conclusion is that this effect may be related to some kind of acceptance issue. Requiring two tagged b-quarks in the event biases our sample towards central top quark rapidities, which we see from our differential measurement causes the asymmetry to be lower. If there are spin-polarization effects going on for the top quarks and daughter b-quarks, this effect might be exacerbated. While our current signal MC samples do not show the deficiency in double tags as we had hoped, we note that these samples are not NLO and do not include spin, so they may leave room for an unaccounted-for acceptance effect. These questions should hopefully be addressed in the next iteration of this analysis, which will tie in the mass-dependence and possibly spin-dependence of the asymmetry with the rapidity dependence.

Finally, we note the asymmetries in the pretag sample as shown in line 13 of Table 6.5. The pretag sample behaves as expected from the admixture of the backgrounds and b-tagged-$t\bar{t}$ asymmetries. For A_{fb}^{lab} the negative backgrounds combine with the positive $t\bar{t}$ to give zero pre-tag asymmetry. For $A_{fb}^{t\bar{t}}$, the pre-tags are the sum of the positive signal asymmetry and the positive background asymmetry.

selection	A_{fb}^{lab}	A_{fb}^{tt}
pre-tag	0.065 ± 0.028	0.062 ± 0.028
inclusive tag	0.140 ± 0.045	0.047 ± 0.045
single tag	0.160 ± 0.052	0.058 ± 0.052
double tag	0.082 ± 0.090	0.016 ± 0.091

Table 6.4: The asymmetry in A_{fb}^{lab} and $A_{fb}^{t\bar{t}}$ for various selections when the b-tag consistency is NOT used in the kinematic reconstruction

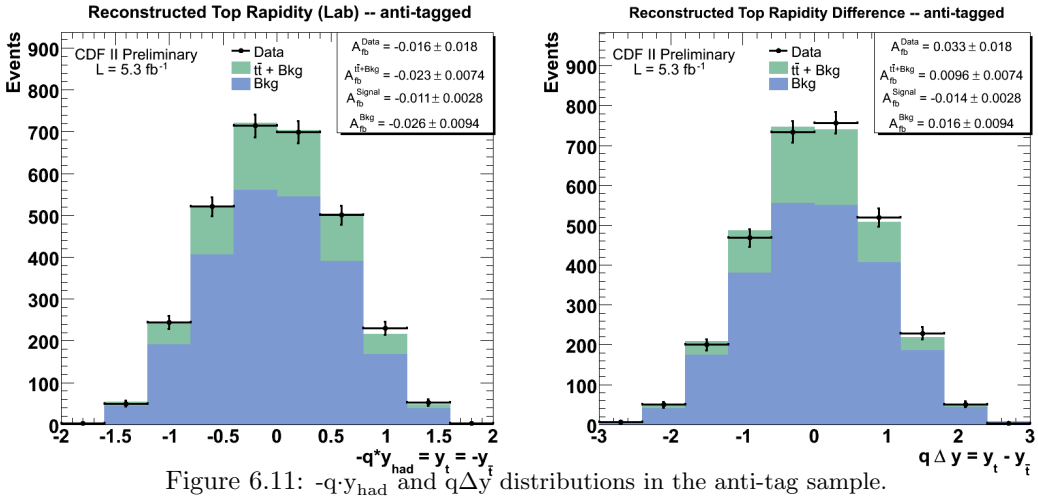

Figure 6.11: -q·y_{had} and qΔy distributions in the anti-tag sample.

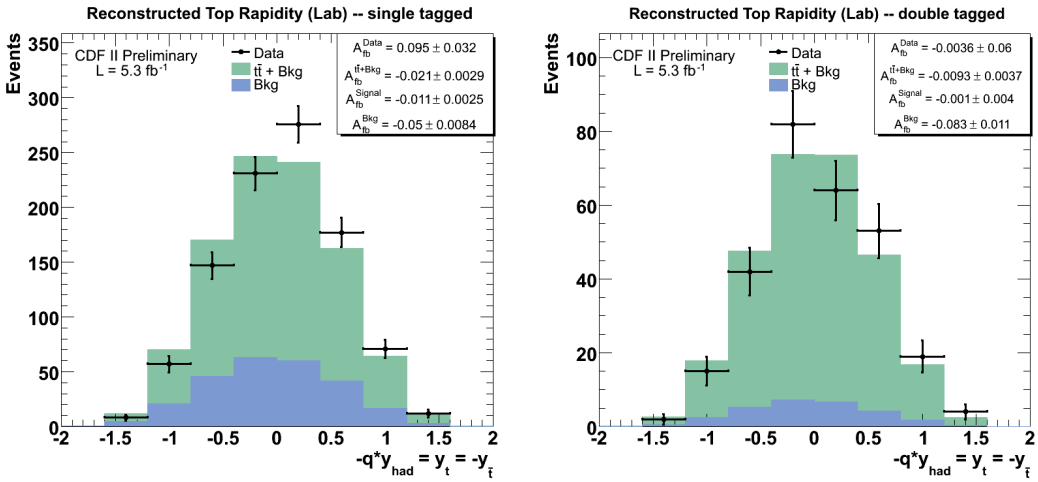

Figure 6.12: -q·y_{had} split by number of tags (single / double)

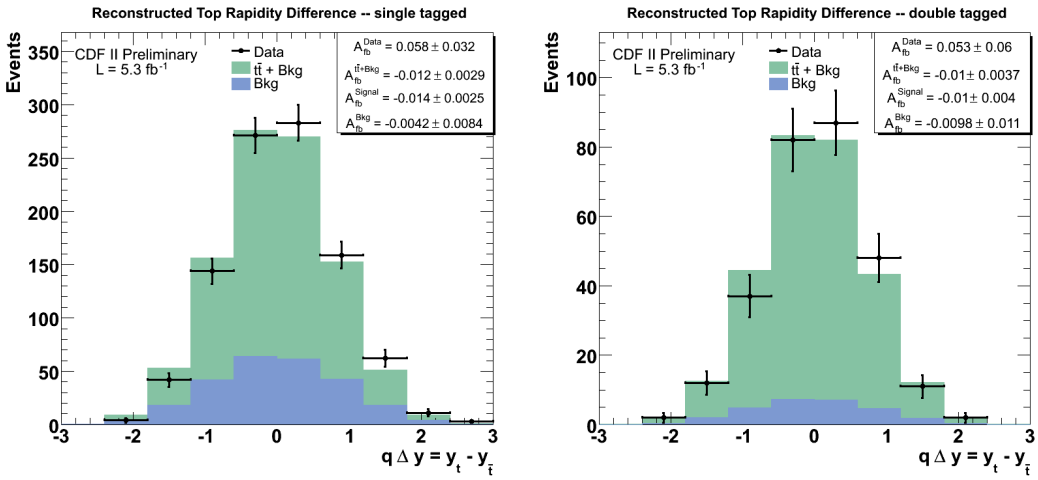

Figure 6.13: qΔy split by number of tags (single / double)

6.3 Conclusions from the Cross Check Study

Having performed various cross-checks of our sample by looking at the A_{fb} values of subsamples, we draw several conclusions. We see that making a χ^2 cut does not cause the asymmetry to vanish, as might be expected were the asymmetry an artifact of the kinematic fitter. Next, we note that the A_{fb} effect is present in both early and late data. While the effect has lessened in the more recent data, we note that the asymmetry is still positive. Overall, it seems that our observed asymmetry is present for events with leptons in each of the detectors, although the asymmetry is somewhat lower for CEM. We do notice some differences for 4-jet and 5-jet subsamples for the $q\Delta y$ variable, but this could be an acceptance effect and shouldn't cause us to doubt the inclusive asymmetry values. Most curious, however, is the asymmetry consistent with 0 for the double-tagged data. This has been observed in previous measurements of A_{fb}, and no clear answer for it has been given.

The results of our cross check studies are summarized below in Table 6.5.

		$A_{-q\cdot y_{had}}$	$A_{q\Delta y}$
1	inclusive tagged	0.0730 ± 0.0281	0.0571 ± 0.0281
2	pos lep (no q weight)	-0.0701 ± 0.0403	-0.0669 ± 0.0403
3	neg lep (no q weight)	0.0757 ± 0.0392	0.0479 ± 0.0393
4	$\chi^2 \leq 9$	0.0924 ± 0.0370	0.0428 ± 0.0371
5	$\chi^2 > 9$	0.0467 ± 0.0432	0.0766 ± 0.0431
6	early data (3.4 fb^{-1})	0.1042 ± 0.0357	0.0708 ± 0.0358
7	later data (2.1 fb^{-1})	0.0228 ± 0.0455	0.0352 ± 0.0455
8	CEM	0.0531 ± 0.0368	0.0259 ± 0.0369
9	CMUP	0.1325 ± 0.0544	0.1265 ± 0.0544
10	CMX	0.0466 ± 0.0719	0.0570 ± 0.0719
11	nJet = 4	0.0756 ± 0.0325	0.0650 ± 0.0326
12	nJet ≥ 5	0.0654 ± 0.0557	0.0343 ± 0.0558
13	pretagged	0.0105 ± 0.0153	0.0404 ± 0.0153
14	single tagged	0.0950 ± 0.0318	0.0582 ± 0.0319
15	double tagged	-0.0036 ± 0.0597	0.0534 ± 0.0596

Table 6.5: The asymmetry in $A_{fb}(-q\cdot y_{had})$ and $A_{fb}(q\Delta y)$ for various selections

Chapter 7.

The Inclusive Parton-level Asymmetry

Now that we have established the presence of an asymmetry in the inclusive $t\bar{t}$ raw sample, we would like to perform corrections to obtain an A_{fb} value for the parton-level. This is the value that theorists are most interested in studying, since it corrects for our experimental biases, such as detector-dependence, event selection, and event reconstruction biases. We will show in the sections below the steps used to correct the raw asymmetry for these effects. First, we wish to remove the background contribution from our data distribution. Next, we will simultaneously correct for acceptance biases and event reconstruction smearing by using a matrix-based linear correction technique. We present our parton-level A_{fb} measurement values in Section 7.9.

7.1 Background Subtraction

Non-$t\bar{t}$ events that pass our event selection requirements have a small overall asymmetry (see Figure 7.1, as well as Table 7.1 for numbers), and this affects our measured $-q\cdot y_{had}$ and $q\Delta y$ distribution shapes. We can estimate the overall shape and size of the background contributions, and we can subtract off a total background shape and correct our data back to the signal shape. We note that some background asymmetries can be large, especially for electroweak processes. The background process for W plus heavy-flavor jets (W+HF) has a predicted asymmetry of $A_{fb}^{-q\cdot y_{had}} = -0.0872 \pm 0.004$ and $A_{fb}^{q\Delta y} = -0.0325 \pm 0.0044$. This is expected, given that the W decays asymmetrically due to the vector-axial (VA) interaction. The other components of the background have much smaller asymmetries, except for the single top samples, but their cross-section is so small that they do not contribute much to the

overall background A_{fb}. One thing to note is that the overall asymmetry predicted is *negative* for both $-q \cdot y_{had}$ and $q\Delta y$, meaning that any correction to the raw distributions will *increase* the asymmetry. Even if we have mis-estimated some of the A_{fb} values or cross-sections for each background component, the background-corrected A_{fb} values should still be larger than the measured raw A_{fb} value. The fact that we observe a large raw asymmetry *before* making a background correction again suggests that our observed asymmetry is caused by physics and not from a mis-modeling of the background.

Because semi-leptonically-decaying top events have 2 bottom quarks, we know that statistically most events will have at least 1 b-tagged jet. Using our event selection cuts as described in Chapter 3, modified so that we require NO jets to be b-tagged, results in an "anti-tagged" sample that presumably is mostly background – that is, has a very low signal-to-background ratio. In fact, the background to signal ratio in our anti-tagged sample is predicted to be $2350/669 = 3.5$. We use this antitagged data sample as a comparison with anti-tagged signal+background MC to see if our background shapes are properly modeled by the MC. Figure 7.2 shows our anti-tagged data sample compared with the anti-tagged $t\bar{t}$ Pythia signal model and predicted background. We see that signal+background shape has an A_{fb} value of -0.011 ± 0.0028 for $-q \cdot y_{had}$, which is in excellent agreement with the value seen for the anti-tagged data, -0.016 ± 0.018. Similarly for $q\Delta y$, we have a signal+background anti-tagged A_{fb} of -0.014 ± 0.0028, comparable to the data value of 0.033 ± 0.018. Additionally, the KS-test values for comparing the data distribution with the signal+background is also very good: 87.6% for $-q \cdot y_{had}$ and 32.5% for $q\Delta y$. Now, it is true that the asymmetry is smaller in the anti-tagged sample than the tagged sample accounted for in Table 7.1. This is because the anti-tags select against the W+HF which has the highest asymmetry. The anti-tags are the control sample we have, and we take the good agreement in the background dominated anti-tags as evidence that the model reproduces the data. Possible model dependence in the shapes and normalizations will be included as systematic uncertainties (see Section 9.1).

It may seem odd that subtracting background generally increases the A_{fb}, even for some positive A_{fb} valued background shapes. This can be explained by the fact that the asymmetry is the difference in forward and background events *divided by the total number of events* – so subtracting off *any* "reasonable" background will increase the magnitude of the data asymmetry. For a

quick example, say we have 55 forward events and 45 backward events in the data. This results in a 10% "raw" asymmetry. Now say we have a background of 22 forward events and 20 backward, an asymmetry of ~5%. When we subtract off this background from the data, we are left with 33 forward events and 25 backward, for a final asymmetry of 14%, a significant increase from the original 10%. Subtracting off a negative asymmetry would result in an even larger increase. Thus, we see that background events tend to dilute any real A_{fb}, so any good measurement of a true parton-level A_{fb} must correct for backgrounds.

There is a slight danger of "over-correcting" for the background contribution, but this is included as a systematic uncertainty, which we will explain in detail in Chapter 9.

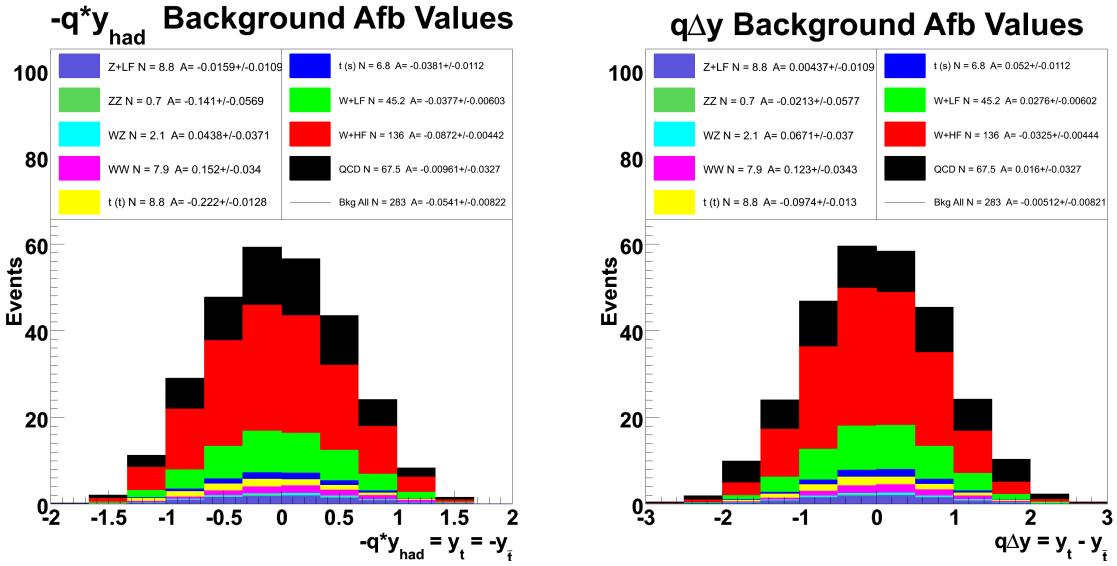

Figure 7.1: Background components for $-q \cdot y_{had}$ and $q\Delta y$

Process	$A_{fb}^{-q \cdot y_{had}}$	$A_{fb}^{q\Delta y}$
Tagged Non-W (QCD)	-0.0096 ± 0.0327	0.016 ± 0.0327
Tagged W+HF Jets	-0.0872 ± 0.004	-0.0325 ± 0.0044
Tagged W+LF	-0.0377 ± 0.006	0.0276 ± 0.006
Tagged Single Top s	-0.0381 ± 0.0112	0.052 ± 0.0112
Tagged Single Top t	-0.222 ± 0.0128	-0.0974 ± 0.013
Tagged WW	0.152 ± 0.034	0.123 ± 0.0343
Tagged WZ	0.0438 ± 0.0371	0.0671 ± 0.037
Tagged ZZ	-0.141 ± 0.0569	-0.0213 ± 0.0577
Tagged Z+Jets	-0.0159 ± 0.0109	0.0044 ± 0.0109
Total Prediction	-0.0541 ± 0.0082	-0.0051 ± 0.00821

Table 7.1: Summary of $A_{fb}^{-q \cdot y_{had}}$ and $A_{fb}^{q\Delta y}$ values for MC background shapes

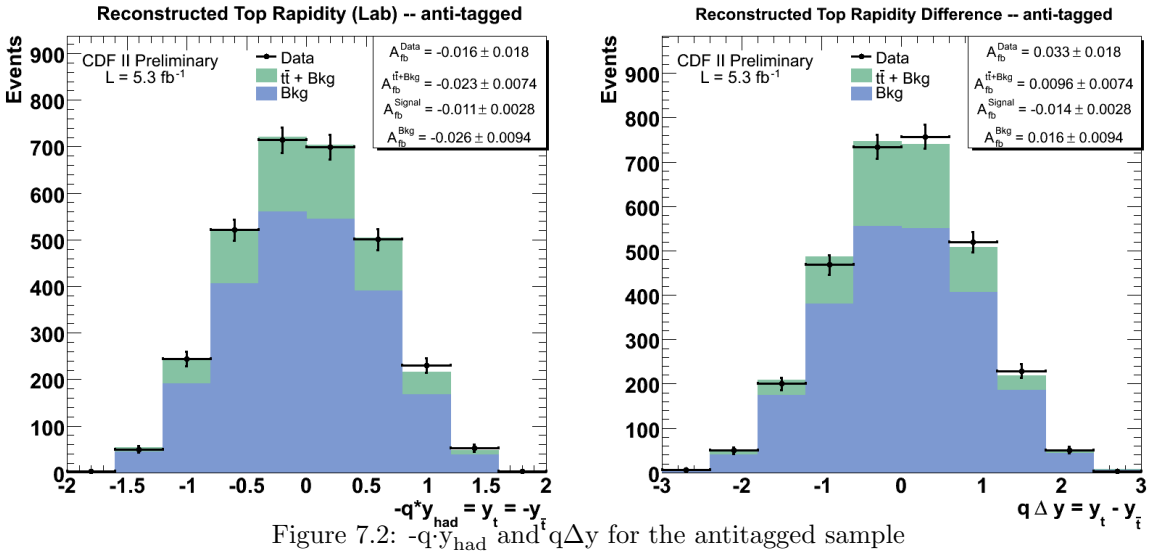

Figure 7.2: -q·y_{had} and qΔy for the antitagged sample

7.2 Smearing and Acceptance Effects

In addition to background contributions, we know of two other effects that modify the true $-q \cdot y_{had}$ and $q\Delta y$ distributions. First, the kinematic fitter is known to smear out the true rapidities of the reconstructed top quark. We can examine this effect by using our Pythia signal MC sample to generate 2d histograms of $-q \cdot y^{TRUE}$ vs $-q \cdot y^{RECON}$ for each asymmetry variable. These histograms describe the movement ("smearing") of events from one bin to another when the "true" data distribution is reconstructed when the kinematic fitter is applied. That is, an event that would fall in a particular bin in the true distribution may "smear" into a different bin in the reconstructed histogram. Thus we call $N_{-q \cdot y_{had}}$ and $N_{q\Delta y}$ "smear histograms". In Figures 7.3 and 7.4 we see 3d views of these histograms and note that most of the large values lie close to the diagonal, meaning there is little extreme smearing of far-apart bins. We note that the smear histograms are roughly symmetrical about the diagonal in the second plot, which shows that if Pythia is a good model then smearing will not cause an A_{fb} (if one did not previously exist in the true distributions). Instead, smearing only dilutes any existing true A_{fb} when the events are reconstructed in the kinematic fitter. This again shows that the correction methods used in this dissertation are not creating an asymmetry, but merely find a parton-level asymmetry value with which theorists may compare their model predictions.

In addition to reconstruction smearing effects, our true distribution is also modified by event selection itself, which cuts out some $t\bar{t}$ events. If this acceptance is biased with respect to y_t, such bias would cause a change in measured A_{fb}. We look at the truth-level distributions (that is, the MC results before the event reconstruction with the kinematic fitter) for events in the MC sample and calculate the ratio of events passed to generated number in each rapidity bin. Using these bin ratios we can then construct a matrix whose diagonal entries contain the ratio information, which describes the acceptance bias. Applying the inverse of this matrix to our data will correct our post-selection-cuts shape to the true pre-cuts shape. We describe this method in Section 7.4, but first we will explain our re-binning procedure.

7.3 Binning

In order to apply matrix-based corrections, it becomes necessary to choose a binning scheme for our $-q \cdot y_{had}$ and $q\Delta y$ distributions and corresponding un-

fold matrices. While using a large number of bins gives greater precision in our understanding of smearing, correcting to the parton-level is limited by statistics in the data. Using a too-finely binned histogram results in "bin to bin oscillation effects" [4] when applying the unsmearing correction (method explained below). However, using the minimum 2-bin scheme (that is, forward and backward bins) could lead to over- or under-correction of smearing, since information from the original smear matrix is lost. For example, if the original $-q \cdot y_{had}$ distribution has more events in the outer edges or near $y = 0$, a 2x2 matrix does not use this additional information when unfolding. From these findings, it becomes clear that we need to use more than 2 bins for our histograms, but not too many, or we encounter oscillation effects. In several of our previous publications [1, 4], it was shown that using 4 bins (two forward bins and two backward) is optimal for resolution while minimizing bin oscillation effects.

Once we have decided on using 4 bins, we then must choose the values for the bin edges. Our two distributions, $-q \cdot y_{had}$ and $q\Delta y$, each have a different range of values. The minimum and maximum values of $-q \cdot y_{had}$ are roughly $\{-2, 2\}$, so this is the range we use for our data and smearing histograms, making the first and last bins contain the overflow events. For $q\Delta y$, the inclusive range was found to be $\{-3, 3\}$. After choosing these boundaries and setting the central bin edges to $y = 0$, we are left with one tunable parameter: the bin edges at $-q \cdot y_{had} = \pm X$ (and $\pm 2X$ for $q\Delta y$). Using different values for this bin edge choice results in variations in the final corrected A_{fb} values, partly due to statistical fluctuations in the bins and changes in the smear and acceptance matrices used for our correction procedure. However, we tested the effect of changing the bin edge and found that it had little overall effect on the final unfolded A_{fb} value. We decided not to include it as a systematic uncertainty. We will describe our method for optimizing our choice of bin edge X later in Section 7.8 – for now we describe our procedure using our final choice of a bin edges at ± 0.5 for $-q \cdot y_{had}$ and ± 1.0 for $q\Delta y$.

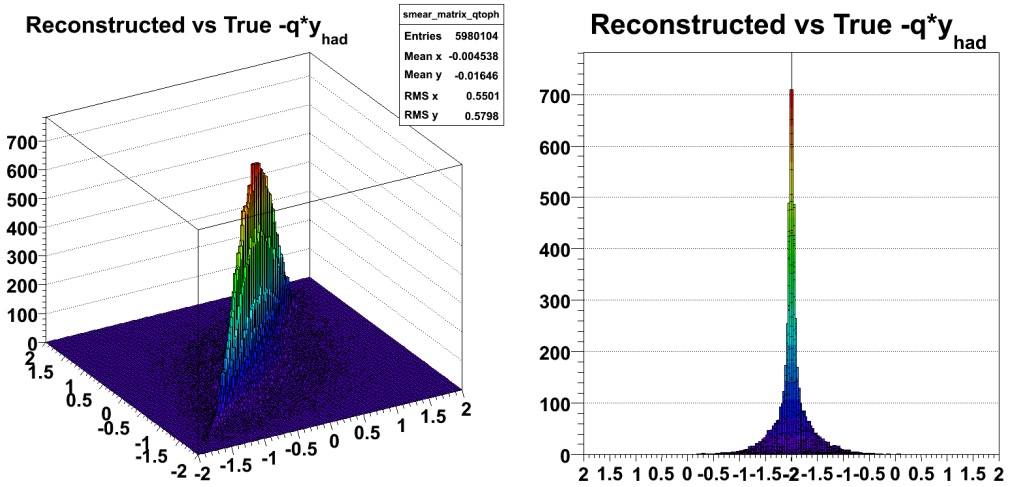

Figure 7.3: 3d plot of the -q·y_{had} 2d histogram N, and a diagonal view

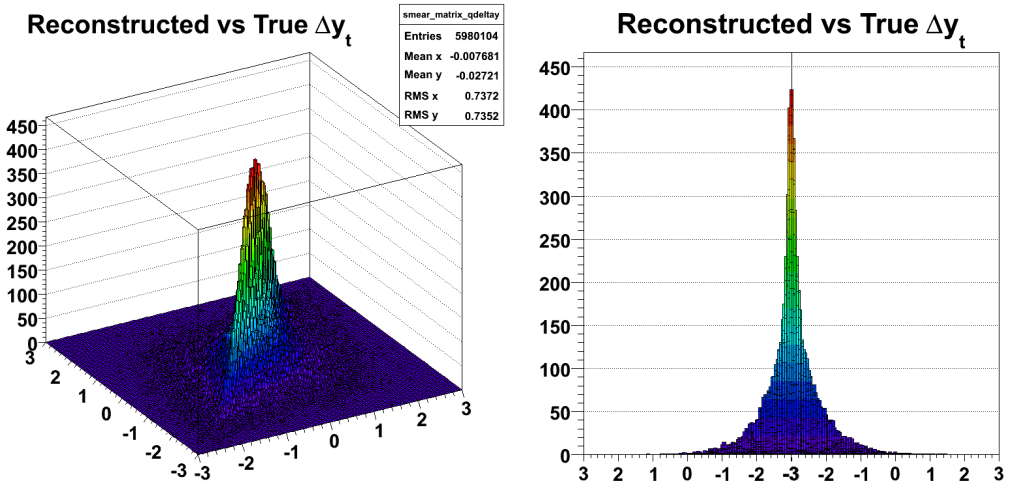

Figure 7.4: 3d plot of the qΔy 2d histogram N, and a diagonal view

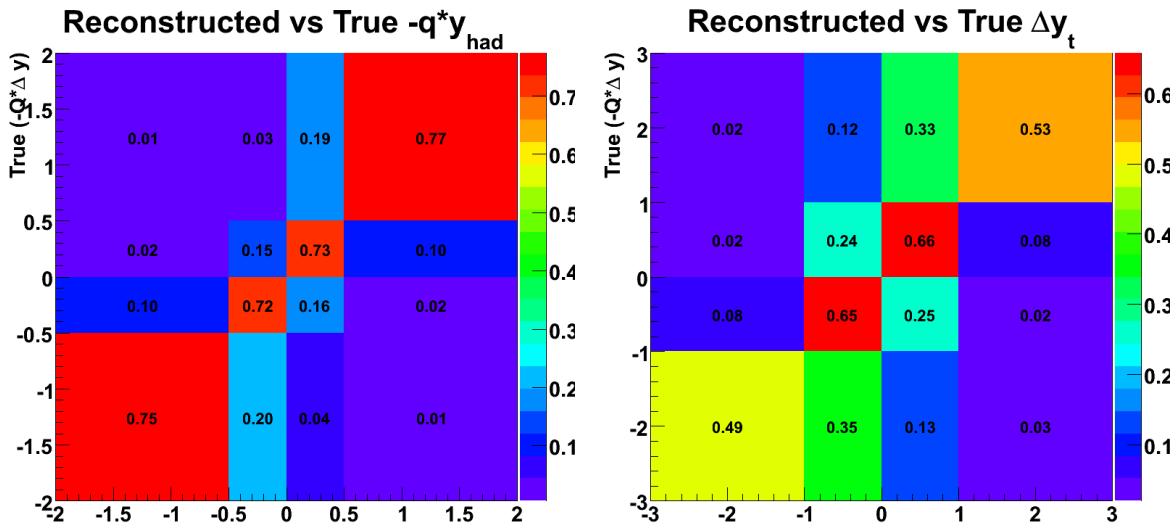

Figure 7.5: Smear matrices S for -q·y_{had} and qΔy, after rebinning according to prescription in Section 7.3

7.4 Correction for Smearing and Acceptance

In order to correct for the smearing resulting from the event reconstruction with the kinematic fitter, we construct the 4x4 smear matrices S from the truth-vs-recon histograms N and binning choice explained above in Section 7.2. The entries of S are

$$S_{ij} = N^{ij}_{recon}/N^{i}_{truth} \tag{7.1}$$

where N^{ij} is the number of events in the smear histogram N as explained above, with i being the "truth bin" index and j the "reconstructed bin" index. N^i is the value of bin i of the truth histogram, the projection of N^{ij}, used to properly normalize the matrix (so entries are in the form of a smear ratio in terms of the original number of truth entries). We note here that Figure 7.5 above is a representation of array S, not histogram N, reflecting the normalization of Equation 7.5. Similarly, Figure 7.6 is a graphical representation of the final unfold correction matrix $A^{-1} \cdot S^{-1}$, which uses S, not N.

In addition to smearing, we also know that selection cuts remove a number of $t\bar{t}$ events from our analysis. These removed events may have a different asymmetry than the remaining events, so to correct our raw asymmetry, we apply the inverse of an acceptance matrix

$$A_{ii} = N^{i}_{selection}/N^{i}_{generated} \tag{7.2}$$

where A only has diagonal terms with values equaling the ratio of number of events selected over the total number, using the same 4x4 binning scheme as the data and smear matrices.

7.5 Applying the correction method

So we see that if we start with a true distribution of -q·y_{had} or qΔy, the distribution is first modified by selection, then smearing, then background (Equation 7.3). We find our final "parton-level" A_{fb} values by correcting for these effects *in reverse order*.

$$N_{raw} = [S \cdot (A \cdot N_{true})] + N_{bkg} \quad (7.3)$$

$$N_{corrected} = A^{-1} \cdot S^{-1} \cdot N_{raw-bkg} \quad (7.4)$$

where N is a vector whose values are the number of events in each bin of our -q·y_{had} distribution. That is, N_{raw} is a column vector containing the number of bin entries for the reconstructed -q·y_{had} data, $N_{raw-bkg}$ is the vector after subtracting off the background histogram bin values, and $N_{corrected}$ is the final vector after unfolding.

The smear matrix we use is calculated from the $t\bar{t}$ Pythia signal MC and is

$$S_{\text{-q·y}_{\text{had}}} = \begin{bmatrix} 0.7455 \pm 0.0092 & 0.0988 \pm 0.0028 & 0.0189 \pm 0.0012 & 0.0055 \pm 0.0008 \\ 0.2028 \pm 0.0047 & 0.7192 \pm 0.0076 & 0.1519 \pm 0.0035 & 0.0338 \pm 0.0020 \\ 0.0437 \pm 0.0022 & 0.1603 \pm 0.0036 & 0.7329 \pm 0.0078 & 0.1869 \pm 0.0047 \\ 0.0080 \pm 0.0009 & 0.0217 \pm 0.0013 & 0.0963 \pm 0.0028 & 0.7738 \pm 0.0097 \end{bmatrix} \quad (7.5)$$

$$S_{\text{q}\Delta\text{y}} = \begin{bmatrix} 0.4890 \pm 0.0112 & 0.0775 \pm 0.0021 & 0.0223 \pm 0.0011 & 0.0206 \pm 0.0024 \\ 0.3516 \pm 0.0094 & 0.6519 \pm 0.0061 & 0.2443 \pm 0.0038 & 0.1199 \pm 0.0059 \\ 0.1336 \pm 0.0057 & 0.2465 \pm 0.0037 & 0.6576 \pm 0.0063 & 0.3274 \pm 0.0098 \\ 0.0258 \pm 0.0025 & 0.0241 \pm 0.0012 & 0.0757 \pm 0.0021 & 0.5321 \pm 0.0126 \end{bmatrix} \quad (7.6)$$

Using this same MC sample, we find from comparing the event counts before and after cuts that

$$A_{\text{-q·y}_{\text{had}}} = \begin{bmatrix} 0.9536 \pm 0.0045 & 0 \pm 0 & 0 \pm 0 & 0 \pm 0 \\ 0 \pm 0 & 1.0776 \pm 0.0043 & 0 \pm 0 & 0 \pm 0 \\ 0 \pm 0 & 0 \pm 0 & 1.0552 \pm 0.0043 & 0 \pm 0 \\ 0 \pm 0 & 0 \pm 0 & 0 \pm 0 & 0.8840 \pm 0.0044 \end{bmatrix} \tag{7.7}$$

$$A_{\text{q}\Delta\text{y}} = \begin{bmatrix} 0.8400 \pm 0.0060 & 0 \pm 0 & 0 \pm 0 & 0 \pm 0 \\ 0 \pm 0 & 1.0870 \pm 0.0037 & 0 \pm 0 & 0 \pm 0 \\ 0 \pm 0 & 0 \pm 0 & 1.0408 \pm 0.0036 & 0 \pm 0 \\ 0 \pm 0 & 0 \pm 0 & 0 \pm 0 & 0.7247 \pm 0.0056 \end{bmatrix} \tag{7.8}$$

Note that neither the S nor A matrices are expected to be unitary, therefore we are unconcerned with array values greater than 1. In fact, because the acceptance ratio (selected/generated) is actually small, we normalize the above matrices to values near 1 in order to easily analyze number trends.

Using these matrices, we find the final correction unfold matrices:

$$A^{-1} \cdot S^{-1}(\text{-q·y}_{\text{had}}) = \begin{bmatrix} 1.4614 & -0.2016 & 0.0044 & -0.0027 \\ -0.3652 & 1.4030 & -0.2826 & 0.0097 \\ 0.0037 & -0.3023 & 1.3983 & -0.3246 \\ -0.0044 & -0.0009 & -0.1981 & 1.5098 \end{bmatrix} \tag{7.9}$$

$$A^{-1} \cdot S^{-1}(\text{q}\Delta\text{y}) = \begin{bmatrix} 2.6638 & -0.3291 & 0.0378 & -0.0522 \\ -1.1096 & 1.7791 & -0.6265 & 0.0274 \\ 0.0249 & -0.6532 & 1.8146 & -0.9703 \\ -0.0791 & 0.0309 & -0.3303 & 2.7926 \end{bmatrix} \tag{7.10}$$

We drop the statistical error in the unsmearing matrix at this point, as it is negligible compared to the overall matrix entry values. In the next section, we explain how errors are propagated for the corrected distribution shape. We see that small statistical errors in the unsmearing matrix would enter only as second-order effects and therefore are negligible compared to the data-background statistical errors and first-order error effects from the correction procedure. In Figure 7.6 we see a graphical representation of the above unsmearing correction matrices. Note that these matrices have large values along the diagonal entries and much smaller values for far off-diagonal entries. This

shows us that smearing occurs mostly for events close to the bin edges in our rebinned distribution. The near-symmetry of these numbers is indicative that the correction procedure should not bias the A_{fb} value.

Again, we note that the $A^{-1} \cdot S^{-1}$ matrix is not expected to be unitary.

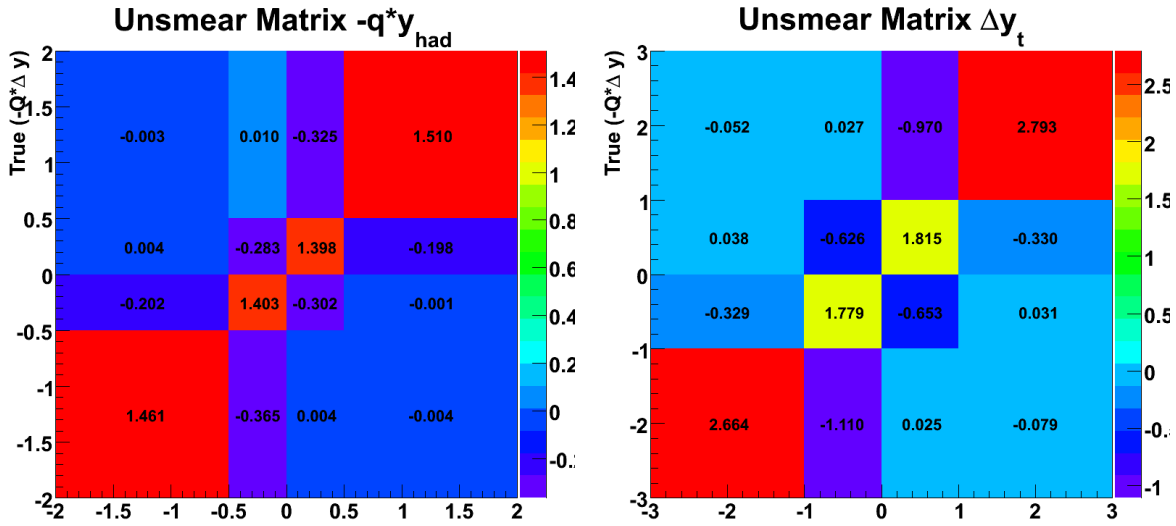

Figure 7.6: Correction Matrices $A^{-1} \cdot S^{-1}$ for -q·y_{had} and qΔy

7.6 The Asymmetry and its Uncertainty

With an understanding of acceptance and reconstruction bias in hand, we can develop an overall formalism for correcting the measured A_{fb} back to the true A_{fb} of $t\bar{t}$ production. The uncertainty is calculated using our prescription found in Reference [4]. Matrices A and S are multiplied together to create a relationship between the background corrected number of forward and backward events and the true number of forward and backward events generated in Monte Carlo. We will call the corrected values that are comparable to the number of events generated $N_{corrected}$.

$$N_{signal(raw-bkg)} = S \cdot A \cdot N_{truth} \tag{7.11}$$

The combined matrix formed by multiplication of A and S is then inverted so that we can solve for the corrected values.

$$N_{corrected} = A^{-1} \cdot S^{-1} \cdot N_{raw-bkg} \tag{7.12}$$

This technique is used to calculate the final corrected asymmetry that may be compared to theoretical prediction. The forward backward asymmetry is calculated as follows. Let,

$$\alpha = [1, 1, ..., 1, 1] \tag{7.13}$$
$$\zeta = [1, 1, ...1, -1, ..., -1, -1] \tag{7.14}$$

Then

$$\mathrm{A_{fb}} = \frac{\zeta \cdot N_{corrected}}{\alpha \cdot N_{corrected}} \tag{7.15}$$

The uncertainty on this equation is slightly more complicated. To simplify some algebra let:

$$N = N_{corr} \tag{7.16}$$
$$n = N_{bkg-sub} \tag{7.17}$$
$$M = A^{-1} \cdot S^{-1} \tag{7.18}$$

So,

$$N = M \cdot n \tag{7.19}$$

is equivalent to Equation 7.12. $\mathrm{A_{fb}}$ can then be represented as a sum:

$$\mathrm{A_{fb}} = \frac{\sum_i \zeta_i \sum_j^{nbins} M_{i,j} \cdot n_j}{\sum_i \alpha_i \sum_j^{nbins} M_{i,j} \cdot n_j} \tag{7.20}$$

Now we just perform simple error propagation:

$$\sigma^2_{\mathrm{A_{fb}}} = \sum_i \sigma^2_{n_i} \cdot \left(\frac{\delta \mathrm{A_{fb}}}{\delta n_i} \right)^2 \tag{7.21}$$

where, σ_{n_i} = the statistical uncertainty in bin "i" for background corrected data and,

$$\frac{\delta \mathrm{A_{fb}}}{\delta n_x} = \frac{(\sum_i \zeta_i \cdot M_{i,x}) \cdot (\alpha \cdot N) - (\sum_i \alpha_i \cdot M_{i,x}) \cdot (\zeta \cdot N)}{(\alpha \cdot N)^2} \tag{7.22}$$

Note that we use analogous formalism to calculate the propagated error for $\frac{\mathrm{dA_{fb}}}{\mathrm{d}(\Delta \mathrm{y})}$, described in detail in Chapter 8

7.7 Validation of the Inclusive Parton-Level Correction

Before using our correction method to find the parton-level asymmetry, we would like to test the method on samples of known asymmetry and verify that

our method correctly finds the true asymmetry. To do this, we first must generate MC samples with known asymmetries. The Pythia $t\bar{t}$ MC sample used in our unfolds has no asymmetry and can be used as one test. We use a sample independent of our unfold sample as data, unfolding it with our method explained above, and compare the unfolded value with the true value. If our procedure is unbiased then we expect to find a corrected A_{fb} value consistent with 0, according to the symmetric Pythia sample. See Figure 7.7 for our plot of a Pythia $t\bar{t}$ sample unfolded with another (independent) Pythia sample. In this figure the green lines are the signal MC (to be compared with the unfold signal, which is the green solid-filled histogram), and the red lines are the histogram after unfolding. The light blue lines are the truth-level distributions, which should be equal to the red histogram if the unfold procedure works correctly. We see that the resulting corrected A_{fb} values are indeed consistent with 0, as expected.

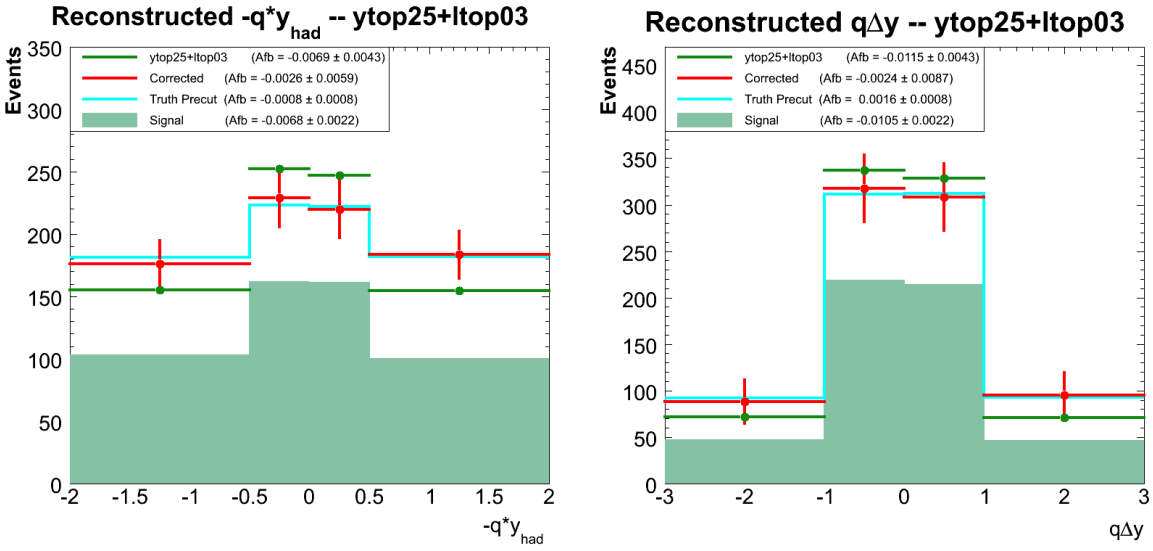

Figure 7.7: Pythia $-q \cdot y_{had}$ and $q\Delta y$ distributions, unfolded with Pythia signal MC

However, even though we do measure a corrected value consistent with 0, this only gives us *one* possible test of the unfold method – what if our collected data (or MC sample, in this case) simply had a statistical fluctuation that gave it a different asymmetry? To account for this, we perform "pseudo-experiments" using the following procedure. Taking the reconstructed events for the independent Pythia sample, we fluctuate each bin of the $-q \cdot y_{had}$ or $q\Delta y$ distributions (assuming Poisson statistics for bin counts). That is, we generate a new histogram using the original histogram as a source distribution. We then unfold this generated histogram with our method and record the corrected

A_{fb} value and A_{fb} uncertainty. These values are recorded into histograms, along with the "pull" (corrected A_{fb} - true A_{fb}, divided by the corrected A_{fb} uncertainty), and a measure of "unfold bias" (corrected A_{fb} - true A_{fb} divided by true A_{fb}). By repeating this method many times (20000 iterations in our tests), we find a distribution of corrected A_{fb} values and other statistics that show how sensitive our method is to statistical fluctuations. This method is known as "pseudo-experimentation", since we use Poisson fluctuations to simulate many experiments with pseudo-data generated by our actual data sample distribution. If our unfolded A_{fb} correctly matches the true value of sample (0 in this case), we expect the corrected A_{fb} histogram to be centered at the truth value. Furthermore, we expect the pull distribution to be a Gaussian distribution, centered at 0, and have a width of 1. This will happen if our statistical uncertainty calculations are correct, that is, if our propagation of error that resulted in Equations 7.21 and 7.22 correctly predicts the statistical uncertainty. In Figure 7.8 we have the results of our 20000 pseudoexperiments performed on an independent Pythia sample. We see that indeed the pull has a width of 1.0, indicating our errors are calculated correctly. The center is at 0 as we expect, indicating there is no bias in the unfold procedure.

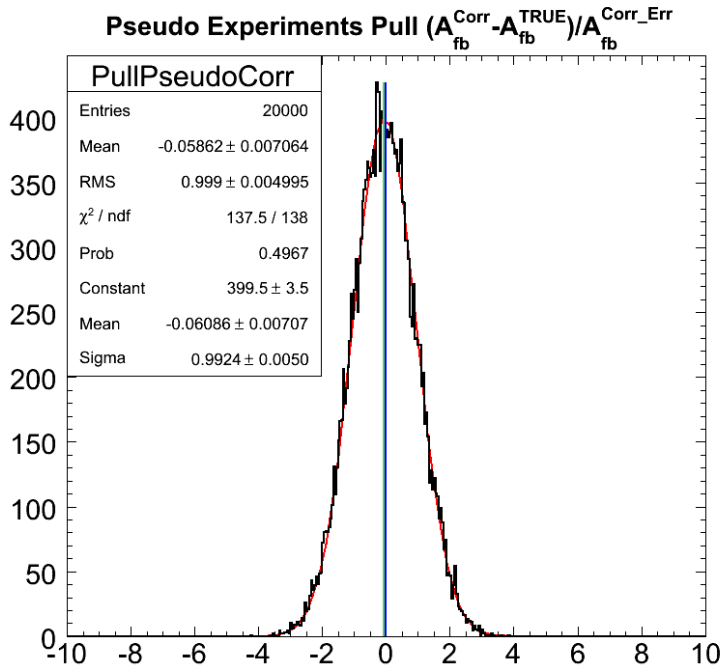

Figure 7.8: 20000 Pseudo-experiments for qΔy (inclusive) on Pythia signal MC
Note that the pull has a width near 1,
indicating that our propagated errors are correct.

Once we have confirmed that our correction method has not created an

asymmetry from data having no asymmetry, we are ready to test the method on a sample having a non-zero asymmetry. For this test, we use the $t\bar{t}$ctopoa/madgraph sample, described in Section 4.3. The ctopoa sample has true asymmetries of $A_{fb}^{lab} = 0.111 \pm 0.001$ and $A_{fb}^{t\bar{t}} = 0.157 \pm 0.001$. Again, we use the -q·$y_{had}$ and qΔy distributions reconstructed with our kinematic fitter, and fluctuate the bins according to Poisson statistics. In Figure 7.9 we have the results of our 20000 pseudoexperiments performed on ctopoa. From Figure 7.9, we see that our pull distribution is centered at 1.354 and has a width of 1.008. The fact that the width is near 1 indicates that our propagation of statistical errors has been handled correctly. The slight "bias" in the pull distributions is partially due to the fact that ctopoa is not truly representative of Standard Model top physics, and we plan to repeat these pseudoexperiments with an MC@NLO sample when one becomes available. We also note that the ctopoa sample has very large MC statistics and therefore small relative errors for bin counts, resulting in a magnification of any small bias.

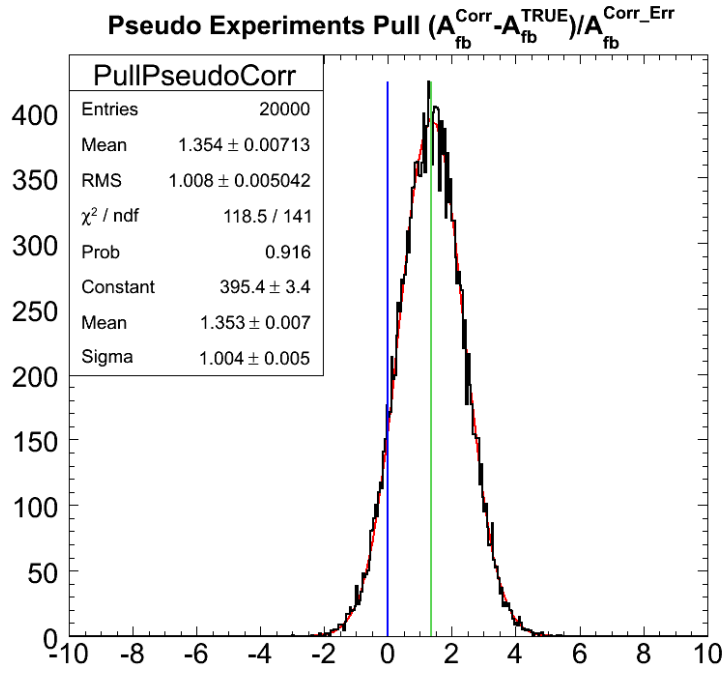

Figure 7.9: 20000 Pseudo-experiments for qΔy (inclusive) on ctopoa/madgraph MC
Note that the pull has a width near 1,
indicating that our propagated errors are correct.

From our work described above, we have shown that our unfold machinery works correctly on both a symmetric sample (Pythia) having zero A_{fb} as well as a sample with a non-zero value (Axigluons+madgraph). This suggests that the unfold machinery works in a linear fashion for a range of true A_{fb} values. In

a previous publication, we tested this linearity hypothesis on intermediate A_{fb} values, using the following method. We first created a series of distributions having fixed, known A_{fb} values in both truth and reconstructed distributions. This was accomplished by using a Pythia MC sample (independent with our unfold sample, hence uncorrelated), finding the true $-q \cdot \cos(\theta)$ distribution in the $t\bar{t}$ frame, linearly reweighting it to a non-zero A_{fb} value, and propagating the reweighted distribution to -q·y_{had} in the lab frame (the full details are described in detail in Reference [1]). These distributions were unfolded and compared with the true A_{fb} for each test. We plotted the true-vs-recon A_{fb} values on a plot, which we have reproduced here in Figure 7.10. We note that the linearity of this plot shows the validity of our method for a large range of A_{fb} values. The slope of the response is close to 1, suggesting that the unfold method has little bias.

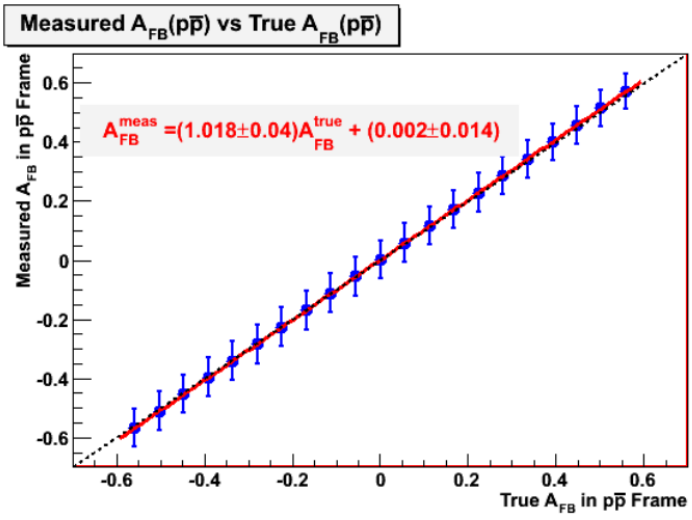

Figure 7.10: Measured (corrected) A_{fb} vs True A_{fb} for reweighted Pythia, unfolded with an independent Pythia sample. This is an example of good correspondence as a result of a bin edge at ± 0.4 Reproduced from Reference [1]

7.8 Correction Bias and Bin Edge Choices

As mentioned previously in Section 7.3, we actually find that different binning schemes result in different slopes and offsets for the linear response plot shown in Figure 7.10. Figure 7.10 shows the slope of the measured vs true A_{fb} for a choice of bin edge at $|y| = 0.4$. The linear fit returns a slope of 1.018 ± 0.040 which, which is consistent with unity. In Figure 7.11, however, we see results of this study using a bin edge at $|y| = 1.0$. Table 7.2 shows numerically

the changes in "measured vs true" slope for several values of bin parameter X. We see that the bias values closest to 0 is for bin edges near 0.2-0.4. However, choosing a bin edge at 0.2 would cause fewer statistics in the center bins of our data and smearing matrix, causing a larger final uncertainty. Thus in Reference [1], the bin edge parameter was chosen to be $|y| = 0.4$ to minimize reconstruction bias and yet maximize central-bin statistics. In this analysis, we actually use the values $|y| = 0.5$ for the $-q \cdot y_{had}$ histogram and $|y| = 1.0$ for $q\Delta y$.

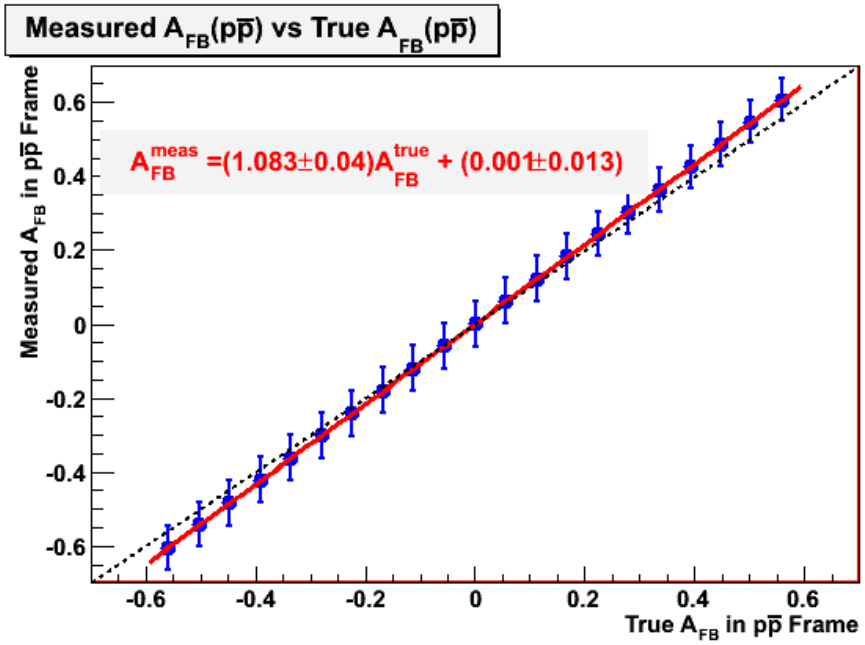

Figure 7.11: An example of poor correspondence as a result of a bin edge at ± 1.0

bin edge X	slope
0.2	0.998 ± 0.041
0.4	1.018 ± 0.041
0.6	1.045 ± 0.039
0.8	1.068 ± 0.038
1.0	1.083 ± 0.038

Table 7.2: Slope of measured-vs-true A_{fb} plot as a function of bin edge X

Confident that our correction method is reasonable and un-biased, we now apply it to our data distributions. Figures 7.12 and 7.13 show the changes in the $-q \cdot y_{had}$ and $q\Delta y$ distributions as we apply the correction steps. The black-lined histogram is the original "raw" data distribution. Subtracting off the predicted background yields the green-colored histogram, and after applying the inverse matrices $A^{-1} \cdot S^{-1}$, we arrive at the final corrected red-colored histogram. The

solid light-green histogram is the $t\bar{t}$ Pythia MC sample, normalized to have the same number of events as the background-subtracted data, so that we can compare the measured background-subtracted sample to a Standard Model prediction. We see that the data exhibit a non-zero asymmetry, whereas the signal model predicts no asymmetry. This correction process will be repeated in our final measurement section where we will present the calculated A_{fb} values for $-q\cdot y_{had}$ and $q\Delta y$.

7.9 The Inclusive Asymmetry

Having validated our data and backgrounds and checked the validity of our correction procedure, we are now ready to calculate a corrected A_{fb} from our data. The black histograms in Figures 7.12 and 7.13 show our raw distributions for $-q\cdot y_{had}$ and $q\Delta y$, which have initial asymmetries of

$$A_{fb\ raw}^{-q\cdot y_{had}} = 0.073 \pm 0.028 \tag{7.23}$$

$$A_{fb\ raw}^{q\Delta y} = 0.057 \pm 0.028 \tag{7.24}$$

We subtract off the background events, which have A_{fb} values of -0.054 ± 0.018 and -0.005 ± 0.008. This results in the green histograms in Figures 7.12 and 7.13. We calculate intermediate background-corrected data asymmetries of

$$A_{fb\ raw\text{-}bkg}^{-q\cdot y_{had}} = 0.110 \pm 0.036 \tag{7.25}$$

$$A_{fb\ raw\text{-}bkg}^{q\Delta y} = 0.075 \pm 0.036 \tag{7.26}$$

Applying our unsmearing correction procedure as explained in Section 7.2, using the $A^{-1} \cdot S^{-1}$ correction matrix in Equation 7.9, and propagating error as explained in Section 7.6, we arrive at the final corrected distributions. These are the red histograms in Figures 7.12 and 7.13. We find asymmetry measurements of

$$A_{fb\ unfolded}^{-q\cdot y_{had}} = 0.150 \pm 0.050 \tag{7.27}$$

$$A_{fb\ unfolded}^{q\Delta y} = 0.158 \pm 0.072 \tag{7.28}$$

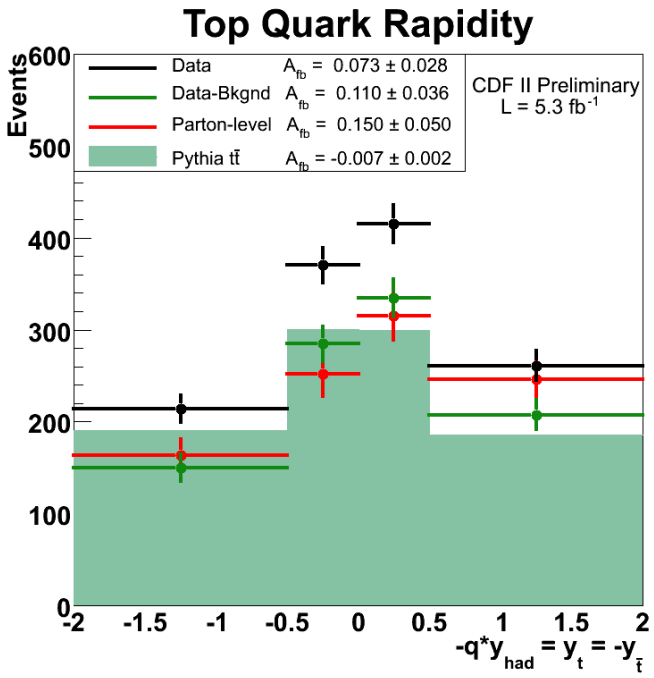

Figure 7.12: $-q \cdot y_{had}$ raw data (black), data-background (green line), corrected data (red) and the signal MC prediction (solid light-green) to compare with data-background.

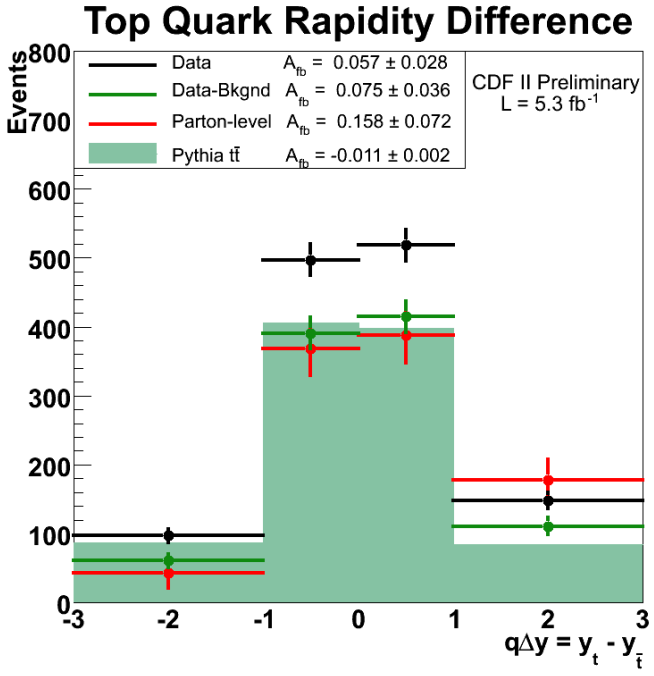

Figure 7.13: Unfold for $q\Delta y$

Chapter 8.

The Rapidity Dependence of the Asymmetry

As we discussed in the introduction, Section 1.11, A_{fb} measurements are not the only way to test the Standard Model and search for physics beyond the Standard Model. To distinguish between possible physics models, it is advantageous to investigate the dependence of A_{fb} as a function of other variables. Now that our dataset has more than 1000 $t\bar{t}$ events, we are gaining enough statistical precision to do this.

The discussion in Reference [10] indicates that the cross-section terms responsible for the asymmetry are proportional to the β of the top/antitop quarks in the center-of-mass; thus, the asymmetry is expected to increase with the rapidity separation of the two quarks. We have shown above in Section 1.8.2 that the rapidity separation is very closely related to the production angle $\cos(\theta^*)$, so we are not surprised that Reference [10] predicts that the asymmetry grows almost linearly with the production angle, as seen in Figure 8.1. In fact, Reference [10] also uses re-summation techniques to examine the stability of the asymmetry at higher orders and finds only modest corrections, as shown.

In order to reproduce these calculations for ourselves, we use the program MCFM [22], which is a fully NLO calculation with NLO PDFs (next-to-leading-order parton-distribution-functions). In Figure 8.2, we see that the predicted NLO QCD $\frac{dA_{fb}}{d(\Delta y)}$ behavior is linear, as we expect from the close relationship between Δy and $\cos(\theta^*)$.

To compare with MCFM predictions, we measure the asymmetry as a function of our Δy distribution bins, which we then write as $\frac{dA_{fb}}{d(\Delta y)}$. We use 10 bins

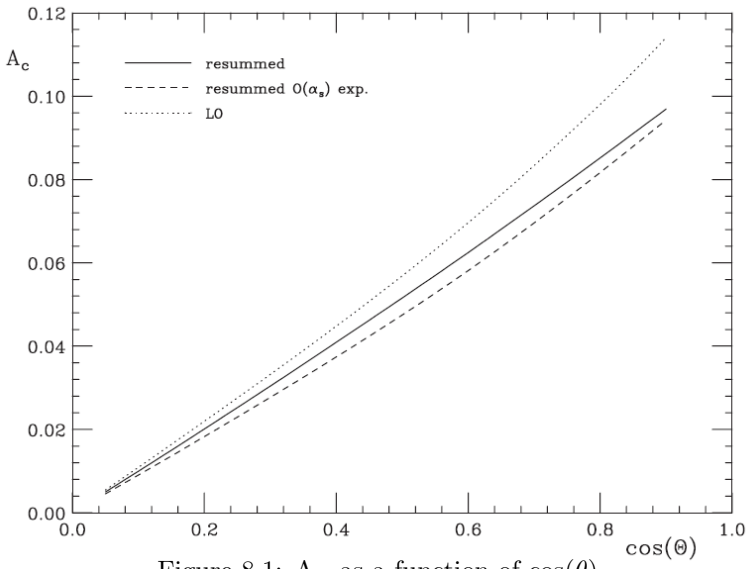

Figure 8.1: A_C as a function of $\cos(\theta)$
(Reproduced from Reference [10]) Note that A_C is equivalent to A_{fb}, as explained in Section 1.8.

for a fine-dependence measurement of raw data and the background-subtracted distribution, but in order to measure the dependence of the parton-level corrected data we use 4 bins as discussed in Section 7.3. The rapidity dependence is then measured by examining the inner and outer bin pairs of our corrected (unfolded) data distributions, using the forward and backward bin event counts in our usual formula. Statistical errors are propagated using the methods described in Sections 7.6 and 8. Thus we obtain $\frac{dA_{fb}}{d(\Delta y)}$ for background-corrected data as well as fully-corrected data.

We verify that this new measurement method works by examining Monte-Carlo (MC) samples with known asymmetries and compare our measured values with the true A_{fb} and $\frac{dA_{fb}}{d(\Delta y)}$ values. By using pseudo-experiments, we can additionally verify the error propagation techniques and test our method for possible biases. We find that our method is reasonable and reconstructs the truth-level A_{fb} and $\frac{dA_{fb}}{d(\Delta y)}$ values quite well.

8.1 The Differential Asymmetry $\frac{dA_{fb}}{d(\Delta y)}$

To measure bin pair asymmetries, we modify our usual A_{fb} formula (Equation 1.9) to the following:

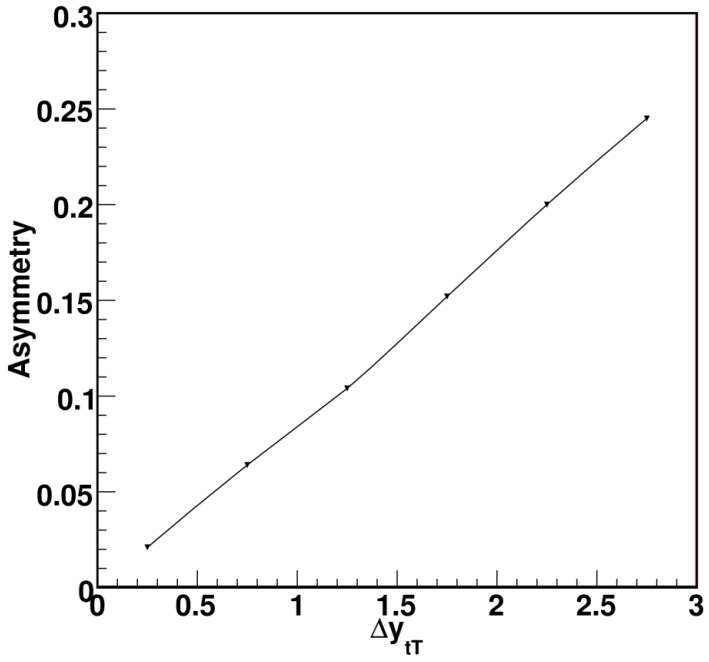

Figure 8.2: MCFM Prediction for $\frac{\mathrm{dA_{fb}}}{\mathrm{d}(\Delta \mathrm{y})}$

$$\mathrm{A_{fb}}(\Delta \mathrm{y}_i) = \frac{N(\Delta \mathrm{y}_i) - N(-\Delta \mathrm{y}_i)}{N(\Delta \mathrm{y}_i) + N(-\Delta \mathrm{y}_i)} \tag{8.1}$$

where $\Delta \mathrm{y}_i$ and $-\Delta \mathrm{y}_i$ represent the forward and backward bins of either the inner or outer bin pair. We note that this is equivalent to using equation 7.15 (or equation 7.20) after substituting a different definition of α and ζ

$$\begin{aligned} \alpha^{\mathrm{inner}} &= [0, 1, 1, 0] && (8.2)\\ \alpha^{\mathrm{outer}} &= [1, 0, 0, 1] && (8.3)\\ \zeta^{\mathrm{inner}} &= [0, 1, -1, 0] && (8.4)\\ \zeta^{\mathrm{outer}} &= [1, 0, 0, -1] && (8.5) \end{aligned}$$

$$\mathrm{A_{fb}^{k}} = \frac{\sum_i \zeta_i^k \sum_j^{nbins} M_{i,j} \cdot n_j}{\sum_i \alpha_i^k \sum_j^{nbins} M_{i,j} \cdot n_j} \tag{8.6}$$

where k is "inner" or "outer".

Using this definition we are additionally able to calculate the propagation of statistical errors. We substitute the α and ζ above into equations 7.21 and 7.22

$$\sigma^2_{\mathrm{A_{fb}}}{}^{k} = \sum_i \sigma^2_{n_i} \cdot \left(\frac{\delta \mathrm{A^k_{fb}}}{\delta n_i} \right)^2 \tag{8.7}$$

where, σ_{n_i} = the statistical uncertainty in bin "i" for background corrected data and,

$$\frac{\delta \mathrm{A^k_{fb}}}{\delta n_x} = \frac{\left(\sum_i \zeta^k_i \cdot M_{i,x}\right) \cdot \left(\alpha^k \cdot N\right) - \left(\sum_i \alpha^k_i \cdot M_{i,x}\right) \cdot \left(\zeta^k \cdot N\right)}{\left(\alpha^k \cdot N\right)^2} \tag{8.8}$$

Note that the sum in equation 8.7 is still over *all* background-subtracted bins. This is because every bin contributes to the final corrected value through the correlations recorded in the smear matrix M. By using α^k and ζ^k we correctly use the components from the smear matrix and background-subtracted data vector to find the propagated error. As a test of this new formula, we ran pseudoexperiments and recorded the $\mathrm{A_{fb}}$, error, and pull distributions for the inclusive sample and each Δy bin. The results of these experiments show that our method indeed works. See Figures 7.9, 8.3, and 8.4. Because the widths of the pull distributions are all near 1, this indicates that our propagation of statistical errors was handled correctly, even for unfolded $\mathrm{A_{fb}}$ values in the $\frac{\mathrm{dA_{fb}}}{\mathrm{d(\Delta y)}}$ measurement. The slight "bias" in the pull distributions is due to the fact that our correction procedure is built on the Pythia model and the physics in that model is different: there is no asymmetry and the $\mathrm{M_{t\bar{t}}}$ distribution is slightly softer. To prove this, we can unfold the $\mathrm{t\bar{t}}$ctopoa model with itself (that is, construct new smear and acceptance matrices based on ctopoa) and we find a much smaller bias value. We again note that the ctopoa sample has very large MC statistics and therefore small relative errors for bin counts. The fact that the means of these pull distributions are not centered at 0 is not as bad as first appears. This is because the mean of the pull distributions is in "units" of σ_{MC}. When we calculate the bias of our method, we find that it is actually smaller than the calculated error we would observe in data. In mathematical form,

$$\text{bias} = \text{Pull Mean} * \sigma_{\mathrm{MC}} \ll \sigma_{\mathrm{data}} \tag{8.9}$$

so we see that for $\mathrm{t\bar{t}}$ctopoa unfolded with Pythia, the bias is actually quite small.

Using the same style as the graphical unfold plots for the inclusive and rapidity-dependence $\mathrm{A_{fb}}$ measurements, in Figure 8.5 we see that ctopoa is

correctly unfolded in the outer rapidity bin to the truth value (the cyan histogram).

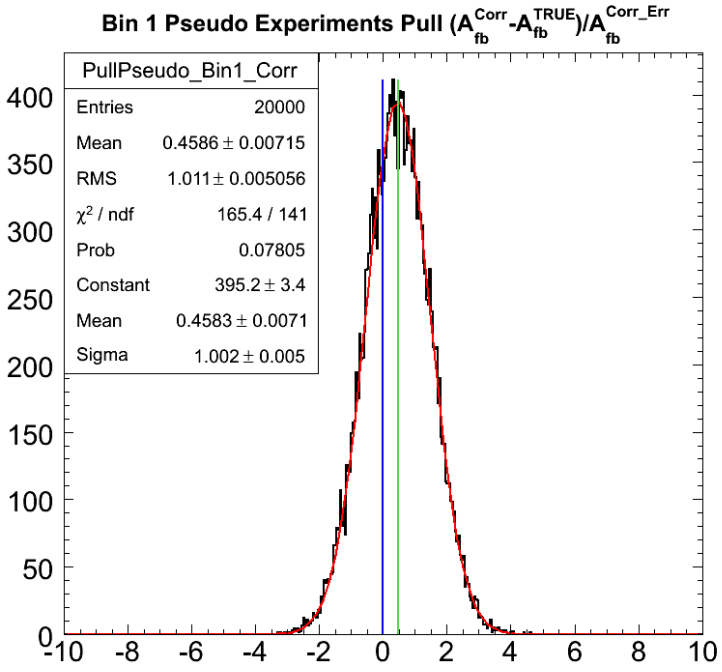

Figure 8.3: 20000 Pseudo-experiments for qΔy (inner bins) Note that the width of the pull is near 1, but it is not centered at 0. This indicates a possible slight bias in the inner bin $\frac{dA_{fb}}{d(\Delta y)}$ measurement for corrected A_{fb}.

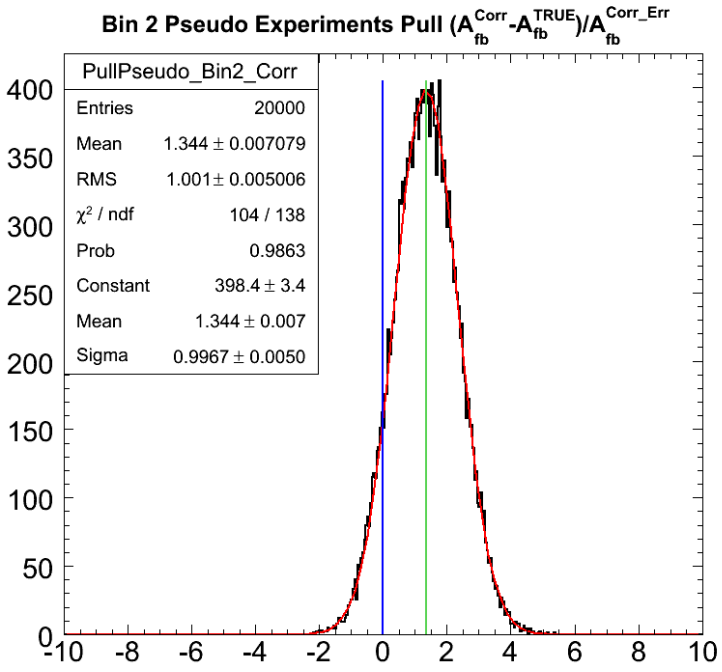

Figure 8.4: 20000 Pseudo-experiments for qΔy (outer bins) Note that the pull is centered near 0 and has a width near 1, indicating a good measurement.

8.2 Measurement of the Differential Asymmetry in Data

Looking at bin-wise A_{fb} values in the data (using values in Figure 7.13 above), we show in Figure 8.6 the raw, data-background, and corrected values for $\frac{dA_{fb}}{d(\Delta y)}$. Note that the slope of the plot shows higher A_{fb} values for the outer rapidity bins, similar to the MCFM prediction in Figure 1.8. We note that the raw $\frac{dA_{fb}}{d(\Delta y)}$ is already very high in the outer bin, that subtracting off the background contribution raises the A_{fb} value even more, and that the corrected A_{fb} value is very high in the outer bin ($> 60\%$). These corrected values are to be compared with the MCFM model predictions of 0.039 ± 0.006 and 0.123 ± 0.018 for the inner and outer rapidities, respectively.

We would like to check that our differential asymmetry is linear as predicted by MCMF (see Section 1.11), but as we discussed in Section 7.3, it is difficult to accurately unfold histograms with more than 4 bins. So we decided to calculate higher-resolution $\frac{dA_{fb}}{d(\Delta y)}$ values for the raw data and background-subtracted data. Our values are shown in Figure 8.7. We see that the behavior is indeed linear, and that both the raw and background-subtracted shapes show large asymmetries in the outer bins.

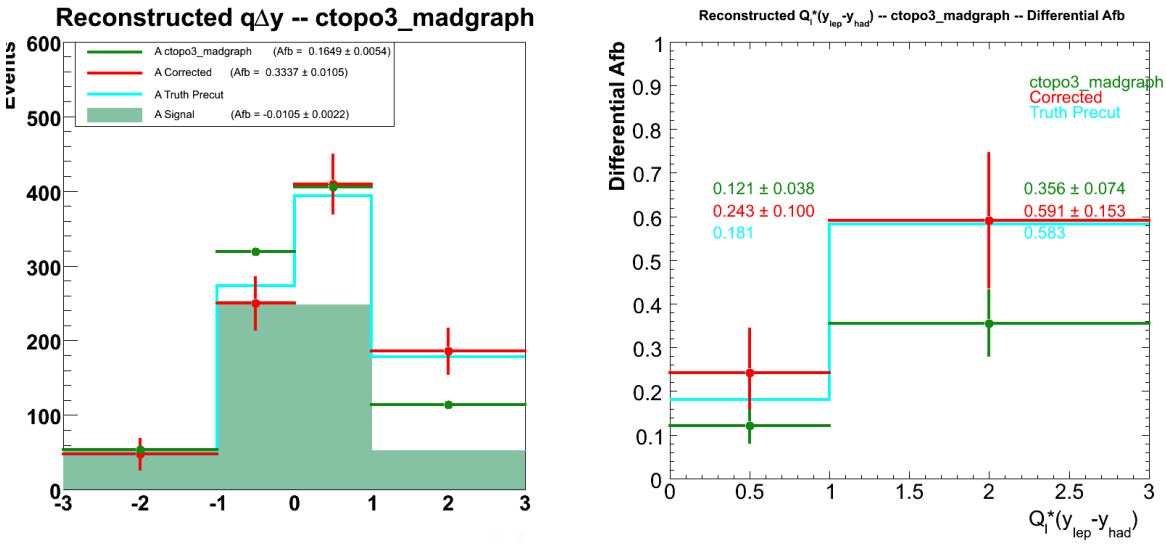

Figure 8.5: Inclusive $A_{fb}^{q\Delta y}$ and $\frac{dA_{fb}}{d(\Delta y)}$ distributions for ctopoa/madgraph

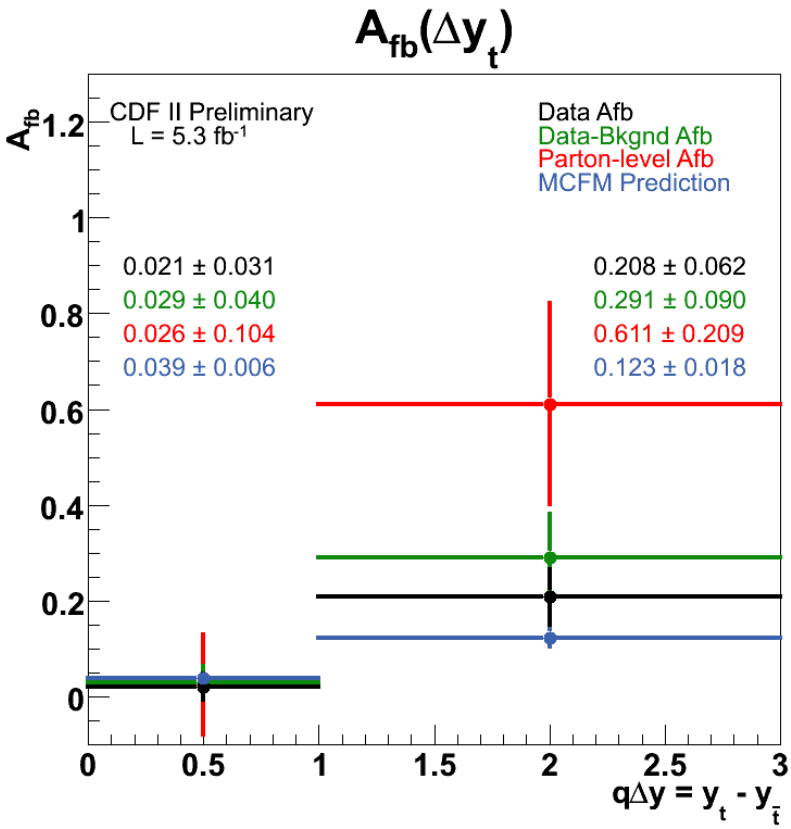

Figure 8.6: Raw, data-background, and corrected $\frac{dA_{fb}}{d(\Delta y)}$ for data

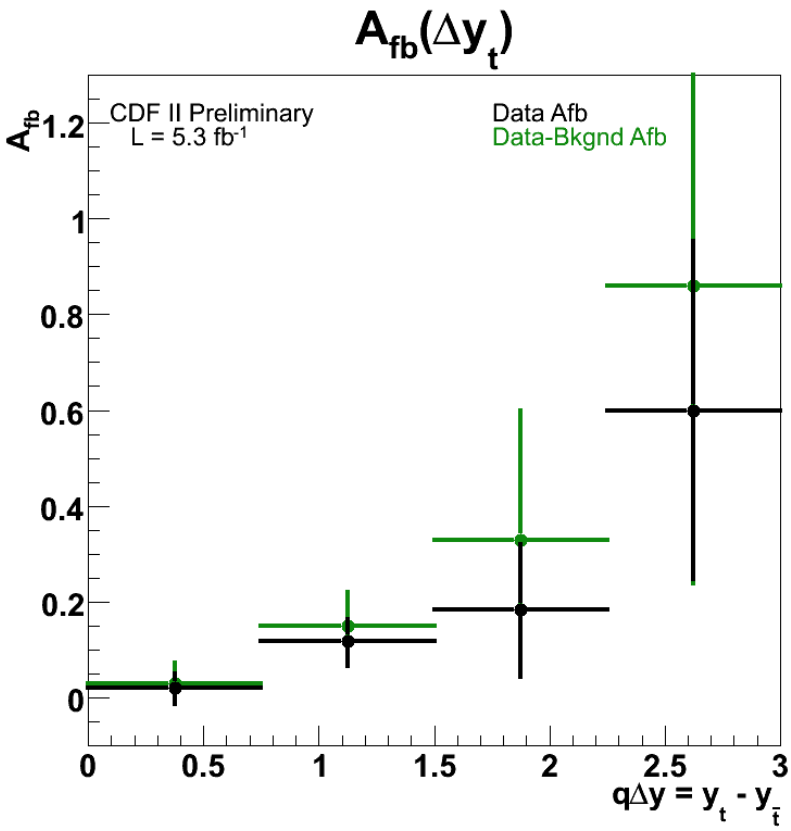

Figure 8.7: Raw and data-background $\frac{dA_{fb}}{d(\Delta y)}$, using a finer binning scheme

To summarize our results before adding systematic uncertainties, see Table 8.1.

	$A_{fb}^{-q\cdot y_{had}}$	$A_{fb}^{q\Delta y}$	Inner A_{fb} ($\|\Delta y\| < 1.0$)	Outer A_{fb} ($\|\Delta y\| > 1.0$)
Raw	0.073 ± 0.028	0.057 ± 0.028	0.021 ± 0.031	0.208 ± 0.062
Raw-Bkg	0.110 ± 0.036	0.075 ± 0.036	0.029 ± 0.040	0.291 ± 0.090
Corrected	0.150 ± 0.050	0.158 ± 0.072	0.026 ± 0.104	0.611 ± 0.210
MCFM	0.038 ± 0.006	0.058 ± 0.009	0.039 ± 0.006	0.123 ± 0.018

Table 8.1: A_{fb} values for $-q\cdot y_{had}$, $q\Delta y$, and $\frac{dA_{fb}}{d(\Delta y)}$, before calculating systematic uncertainties

Chapter 9.

Systematic Uncertainties

Our raw A_{fb} measurement is independent of any model assumptions – that is, other than assuming a semi-leptonic $t\bar{t}$ decay for the kinematic fitter event reconstruction, we do not make any other physics model assumptions. However, when we subtract off a background shape we are assuming that our model of background component shapes and sizes is correct. Similarly, our matrix unfold technique for correcting smearing and acceptance effects assumes that the Pythia $t\bar{t}$ MC is actually representing the physics of $t\bar{t}$ decays. This model has tunable parameters for masses, parton distribution functions (PDFs) for the incoming parton momenta, and other parameters that may affect the unsmear matrix values and thus affect our corrected A_{fb} values. We wish to see what impact our model assumptions have on our corrected measurement values. To do this, we vary all model parameters within $\pm\sigma$ of a parameter's uncertainty and measure the resulting A_{fb} value. These variances will be recorded as "systematic uncertainties" (also called "systematic errors") and listed in our final measurement values. The final total uncertainty of an A_{fb} value will be its statistical error and systematic uncertainty added in quadrature.

Because our correction method involves subtracting background shapes and unfolding the resulting distribution with smearing information from signal MC, our systematic uncertainties are easily organized into two categories: background uncertainties and top signal model uncertainties.

The background systematic uncertainties are handled by subtracting different shapes and cross-sections (as described in Section 7.2) from the raw data and comparing the final corrected (unfolded using Pythia) A_{fb} values. The signal model uncertainties are handled slightly differently – we use the background-subtracted data corrected using Pythia and compare this "nomi-

nal" corrected A_{fb} value to a second unfolded value made using different MC signal sample to generate the unfold matrix. We use the average values of the differences (or half of the maximum absolute difference, if both differences have the same sign) to obtain a final calculation for each systematic uncertainty. The calculated uncertainties for each component and each A_{fb} variable are summarized in Table 9.5. These components are added in quadrature to obtain a final systematic uncertainty for our measurement.

9.1 Background Uncertainties

The background subtraction influences the final corrected A_{fb} measurement through uncertainties in size and shape.

To account for the background size normalization, we use our reweighted signal MC simulation (see Section 7.2) and add on the predicted background scaled by +25% and −25%, which roughly corresponds to $\pm\sigma$ for the uncertainty in total background cross-section. We then use our correction procedure to subtract off the normal expected background and unfold. By comparing our A_{fb} measurement of these modified samples with the corrected A_{fb} for the nominal shape (with unscaled background) we record the difference as our systematic uncertainty.

The overall shape of the background is determined by adding various MC samples (Table 4.3) weighted by the predicted numbers for each cross-section (Table 4.4). However, this background shape may be incorrect, so we wish to compare results with modified background shapes. It is difficult to define a $+\sigma$ and $-\sigma$ convention, so to account for uncertainty in background shape we choose single components of the predicted background samples and reweight these shapes to have the same area as the predicted total background cross-section. We choose the largest 2 components of our backgrounds – QCD and Wbb – for this test. Because the root-mean-square (RMS) width of the QCD shape is much larger than predicted the total background shape we decided to use a linear combination of 55% QCD and 45% Wbb for the first shape and 100% Wbb for the second shape. The A_{fb} for each of these samples can be found in Table 7.1. We choose the average of the differences between corrected MC samples' A_{fb} values and the nominal corrected A_{fb} as our background shape uncertainty.

Tables 9.1 and 9.2 show the results for the background size and shape uncertainties:

	nominal A_{fb}	less	difference	more	difference	uncertainty
background size	0.1498	0.1357	0.0141	0.1662	-0.0164	0.0153
		QCD		Wbb		
background shape	0.1498	0.1336	0.0162	0.1620	-0.0122	0.0142

Table 9.1: -q·y_{had} background systematic uncertainties

	nominal A_{fb}	less	difference	more	difference	uncertainty
background size	0.1582	0.1482	0.0100	0.1698	-0.0116	0.0108
		QCD		Wbb		
background shape	0.1582	0.1337	0.0245	0.1728	-0.0146	0.0196

Table 9.2: qΔy background systematic uncertainties

9.2 Signal Uncertainties

Top signal MC is generated with a set of assumptions which we describe below. Since the top model is used only in the unfold matrix when calculating the corrected A_{fb}, it is the unfold matrix that we modify by $+\sigma$ and $-\sigma$ for each systematic uncertainty category. Essentially we unfold the background-subtracted data with matrices generated from different MC samples that have the top parameters varied by $+\sigma$ and $-\sigma$, then we compare the resulting corrected A_{fb} value with the nominal A_{fb} value calculated from the Pythia unfold. The average or largest of these differences (as per the top group conventions) is our systematic uncertainty for the varied parameter. Tables 9.3 and 9.4 show the numbers calculated for these signal uncertainties.

9.2.1 Initial and Final State Radiation (ISR/FSR)

Partons in a $t\bar{t}$ event may radiate gluons as seen in Figures 1.5a and 1.5b. These gluons may be energetic enough to produce jets, perhaps capable of being misidentified in event reconstruction as a decay quark. The branching ratios of such radiative effects is not well understood and is treated as a tunable parameter in top signal MC generation. We follow the top group's use of samples dtops1 and dtops1 to model $+1.0\sigma$ and -1.0σ shifts in the amount of radiation for both ISR and FSR.

9.2.2 Jet Energy Scale (JES)

Jet energies are determined by integrating over sections of the calorimeter hit by a jet using a jet clustering algorithm, however, this process is far from trivial and requires corrections. First, different calorimetry systems in the CDF detector have different response efficiencies for various particles. Calorimetry values often exhibit non-linear response to true particle energy. There are non-covered geometries in the detector, including spaces, or "cracks", between calorimetry towers. Additionally there are inefficiencies and uncertainties associated with the integration clustering algorithms assigning calorimetry towers to jets. These effects all contribute overall adjustments to final jet energies, for which corrections are calculated. Here is a list of individual uncertainties in JES that we take into account

- Relative Correction
  Corrections due to η dependent calorimeter response.
- Underlying Event Correction
  Correcting for energy associated with the spectator partons in the event.
- Absolute Correction
  Corrects the jet energy measured in the calorimeter for any non-linearity and energy loss in the non-instrumented regions of the detector.
- Out-of-Cone Correction
  Corrects back to the particle-level energy by accounting for leakage of radiation outside of the jet clustering cone.
- Splash-Out Correction
  Uncertainty in the energy leakage beyond the out-of-cone scope.

Accounting for these effects incorrectly would cause different parts of the detector to have more or less response to jets, leading to an incorrect asymmetry measurement. We measure the uncertainty associated with these corrections by using the Pythia top signal MC sample and vary these JES components by $+\sigma$ or $-\sigma$. We take the differences of the corrected A_{fb} values to calculate our JES systematic uncertainty.

9.2.3 Parton Distribution Function (PDF)

The momentum distribution of partons and gluons in Monte Carlo simulations is derived from empirically calculated functions, called "PDFs". The momentum distribution of particles in hard scattering process determines the "energy" spectrum of the $t\bar{t}$ system. To study the effect on our measurement

to the uncertainty in the PDF, we compare 46 different sets of PDF: CTEQ6M, CTEQ5L, MRST72, MRST75, CTEQ6L, CTEQ6L1, CTEQ6M ± 20 (orthogonal pdf sets). The differences between the ± eigenvectors are compared and added in quadrature. We separately add the difference between MRST72 and CTEQ5L. The larger of these 2 sums, added in quadrature with the differences in the MRST72 and MRST75 sets, is taken as our PDF systematic uncertainty.

9.2.4 Color Reconnection

We compare different "tunes" of color-flow parameters to each other and our nominal unfold. Sample ctopsd corresponds to the "Apro" tuning, while ctopse corresponds to "ACRpro".

9.2.5 Top MC Sample

Monte Carlo is expected to model the $t\bar{t}$ process from production to final state particles. This requires a number of effects to be simulated properly, such as top quark production, decay, and hadronization. Uncertainty in any number of these effects translates into measurement uncertainty. Fortunately, these simulations have been tested and refined over many measurements of various processes. Nonetheless, we assign an uncertainty to our measurement to account for differences between our model and the actual $t\bar{t}$ process. We calculate the systematic error by comparing our measurement for two entirely different MC simulations: Pythia and Herwig. The sample we use for Alpgen+Pythia is dtopa2, and for Alpgen+Herwig we use dtopa3. The absolute difference between these two corrected A_{fb} values is taken as our top shape systematic uncertainty.

	nominal A_{fb}	less	difference	more	difference	uncertainty
ISR/FSR	0.1498	0.1396	0.0102	0.1588	-0.0090	0.0096
JES	0.1498	0.1488	0.0010	0.1538	-0.0040	0.0025

Table 9.3: Selected $-q \cdot y_{had}$ signal systematic uncertainties

	nominal A_{fb}	less	difference	more	difference	uncertainty
ISR/FSR	0.1582	0.1562	0.0020	0.1554	0.0028	0.0014
JES	0.1582	0.1540	0.0042	0.1670	-0.0088	0.0065

Table 9.4: Selected $q\Delta y$ signal systematic uncertainties

9.3 Systematic Uncertainties for the Rapidity Dependence

We repeat the procedures above for our inner and outer rapidity bins when measuring the uncertainties in $\frac{dA_{fb}}{d(\Delta y)}$, using the nominal values found for these bins in Section 8.2. The results for each uncertainty component are listed in Table 9.5 below.

9.4 Final Measurement with Systematic Uncertainty Calculation

By adding the various systematic uncertainties listed above (background size/shape, signal parameters) in quadrature, we arrive at these final values:

Systematic Uncertainty	$A_{fb}^{-q \cdot y_{had}}$	$A_{fb}^{q\Delta y}$	$A_{fb}(\lvert\Delta y\rvert < 1.0)$	$A_{fb}(\lvert\Delta y\rvert > 1.0)$
background size	0.015	0.011	0.002	0.086
background shape	0.014	0.007	0.005	0.107
ISR/FSR	0.010	0.001	0.004	0.004
JES	0.003	0.007	0.002	0.003
PDF	0.005	0.005	0.054	0.013
Color Reconnection	0.001	0.004	0.007	0.007
MC Generator	0.005	0.005	0.004	0.033
Total Uncertainty	0.024	0.017	0.055	0.141

Table 9.5: Summary of the systematic uncertainties
CDF II Preliminary, L = 5.3 fb^{-1}

Chapter 10.

Final Measurement Values and Conclusion

Our final inclusive front-back asymmetry results are measured to be

	$A_{fb}^{-q\cdot y_{had}}$	$A_{fb}^{q\Delta y}$
Raw	0.073 ± 0.028	0.057 ± 0.028
Raw-Bkg	$0.110 \pm 0.036 \pm 0.016$	$0.075 \pm 0.036 \pm 0.007$
Corrected	$0.150 \pm 0.050 \pm 0.024$	$0.158 \pm 0.072 \pm 0.024$
MCFM	0.038 ± 0.006	0.058 ± 0.009

Table 10.1: Final inclusive A_{fb} values for $-q\cdot y_{had}$ and $q\Delta y$
CDF II Preliminary, L = 5.3 fb^{-1}

These values should be compared to the small $p\bar{p}$ frame charge asymmetry expected in QCD at NLO, $A_{fb} = 0.050 \pm 0.015$ [7, 8, 9, 10]

The rapidity dependence of A_{fb}, $\frac{dA_{fb}}{d(\Delta y)}$, is measured to be

	$A_{fb}(\lvert\Delta y\rvert < 1.0)$	$A_{fb}(\lvert\Delta y\rvert > 1.0)$
Raw	0.021 ± 0.031	0.208 ± 0.062
Raw-Bkg	$0.029 \pm 0.040 \pm 0.004$	$0.291 \pm 0.090 \pm 0.033$
Corrected	$0.026 \pm 0.104 \pm 0.012$	$0.611 \pm 0.210 \pm 0.246$
MCFM	0.039 ± 0.006	0.123 ± 0.018

Table 10.2: Final $\frac{dA_{fb}}{d(\Delta y)}$ values
CDF II Preliminary, L = 5.3 fb^{-1}

The corrected $\frac{dA_{fb}}{d(\Delta y)}$ values should be compared with the MCFM model predictions of 0.039 ± 0.006 and 0.123 ± 0.018 for the inner and outer rapidities, respectively.

We see from these results that our final corrected measured A_{fb} values are larger than the Standard Model predictions by about 3 σ. This is a tantalizing

result, as it is not yet precise enough yet to rule out the Standard Model nor prove the existence of particles beyond the Standard Model, such as axigluons. Further data taking is needed in order to gain the statistical sensitivity to make such claims. However, we have accomplished much in making this measurement. Previously, theorists had only inclusive A_{fb} values to compare with their theory predictions, whereas we now have results for the rapidity dependence. This additional level of information may prove valuable in ruling out certain BSM models and pursuing others. Additionally, we have made a more sophisticated treatment of systematic uncertainties than done previously, which should aid future A_{fb} analyses.

The $M_{t\bar{t}}$ mass dependence of A_{fb} has recently been measured at CDF, as well as the spin correlations for top quarks. Combining these analyses with a measurement of the inclusive A_{fb} and rapidity dependence is a natural next step for future work. This would be a true *tour-de-force* of top quark production in the semi-leptonic channel. There are other techniques for adding statistics to our sample as well, such as including "loose muons" and PHX electron events. It is also recommended that this measurement be performed in other top quark channels, especially the dilepton channel. An observed asymmetry in this (independent) channel would give more weight to believing our large measured asymmetry is not a statistical fluctuation. In fact, combining these channels into one analysis, or even making a combined CDF+D$\emptyset$ result would provide a huge increase in our statistical sensitivity.

The A_{fb} measurement is very interesting and offers a unique way to test the Standard Model and put constraints on BSM theories. It is hopeful that this analysis will continue and provide new insights in the future.

Appendix A.

Details of Event Selection Cuts

Event selection at CDF is accomplished in several stages, beginning with "online" triggers that filter out events that are not likely to meet criteria for passing later physics cuts. This is done in real time as collisions occur in the detector. Because leptons have charge and are more easily identified by tracks in the silicon and COT detectors, our first triggers primarily test for the presence of a high-momentum electron or muon, requiring a signal to be in the CEM, CMUP, or CMX calorimeters. Again, we note that the trigger requirements for leptons are not unique to this analysis, but used by many different analyses at CDF. Once an event passes the online triggers, data is written to tape in "streams" according to which triggers were set. Offline processing is used to further reconstruct the event, by applying calibration corrections and identifying parton jets in the calorimeters. Finally, reconstructed "physics objects" such as electrons, muons, jets, and $\not\!\!E_T$ are written. These events then must pass our final cuts as explained in Chapter 3.

A.1 Electron Identification

We identify electrons by matching an isolated deposit of energy from a single electromagnetic calorimeter tower in the CEM ($|\eta| < 1.0$) to a single isolated track.

A.1.1 CEM Triggers

Level 1

- A cluster of energy in the central EM calorimeters with $E_t \geq 8.0$ GeV.
- The ratio of energy deposited in the HAD compartment to EM compartment in the calorimeter tower is small [(HAD/EM) ≤ 0.125] as expected

for an electromagnetic shower.

- One or more tracks in the COT with $P_t \geq 8$ GeV.

Level 2

- A cluster of energy in the central EM calorimeters with $E_t \geq 16.0$ GeV, and (HAD/EM) ≤ 0.125.
- A track in the COT at level 1 must point to the cluster.
- Matching track $P_t \geq 8$ GeV.

Level 3

- A cluster of energy in the central EM calorimeters with $E_t \geq 18.0$ GeV, and (HAD/EM) ≤ 0.125.
- Matching track $P_t \geq 8$ GeV.
- $L_{shr} < 0.4$
  The lateral shower profile compares the small sharing of the shower energy across neighboring towers with expectations based on test beam data. The L_{shr} cut is on the χ^2 of the comparison.

A.1.2 Offline Selection

Offline selection is applied to events that have passed through the trigger levels. The cuts can be more stringent because the offline information is more detailed. Electrons that pass the offline selection criteria are referred to as "tight" electrons. The offline selection criteria for electrons is detailed below.

- $E_t \geq 20$ GeV
  Electrons in $t\bar{t}$ events are expected to have high energy.
- $P_t \geq 10$ GeV
  For an ideal electron $P_t = E_t$.
- $P_t \geq 50$ GeV (if $E_t > 100$ GeV)
  This cut filters out high momentum hadrons that fake electrons.
- $E_{HAD}/E_{EM} < 0.055 + 0.00045 \cdot E$
  Since the electromagnetic shower of an electron is mostly contained in the electromagnetic compartment, we can reduce the number of jets misidentified as an electron by requiring that the ratio of hadronic energy to electromagnetic energy is small.
  The requirement is linearly scaled with energy because very high energy electrons will deposit a larger fraction of energy into the hadronic compartment.

- $E/p < 2.0$ (if $E_t < 100$ GeV)
  The energy an electron deposits in the calorimeter should be approximately be the same as the momentum of the matching track.
- # COT Axial Segments ≥ 3 and # COT Stereo Segments ≥ 2
  This is a quality cut on the electron track found in the COT.
- $Track|z_0| < 60$ cm
  z_0 is the z intercept of the electron track. This is done to guarantee the track originates from optimal regions in the COT.
- -3.0 cm $< Q \cdot \Delta x < 1.5$ cm
  Δx is the distance in the x-coordinate between the COT track position extrapolated to the CES and the actual hits in the CES chamber. Matching tracks between CES and the COT is charge dependent and, therefore, this cut is different depending on the charge of the electron track.
- $|\Delta z| < 3.0$ cm
  Δz is the distance in the z-coordinate between the COT track position extrapolated to the CES and the actual hits in the CES chamber. A minimum window is applied to this distance to match the COT track to the CES hits.
- $\chi^2_{strip} < 10$
  A χ^2 test is performed between the profile of hits in the CES and the expected profile of electrons.
- $L_{shr} < 0.2$
  A tighter requirement on the lateral shower profile.
- $Isolation < 0.1$
  The energy deposited in a calorimeter by an electron is very collimated. An "isolation" requirement examines the energy nearby the electron. Jets that fake electrons are filtered out by requiring that energy deposited in a cone around the electron is small. This is quantified by the variable I_l.

$$I_l = \frac{\sum E_t^{\Delta R<0.4} - E_t^{electron}}{E_t^{electron}}$$

  The ratio of energy in a cone $\Delta R = \sqrt{(\Delta\phi)^2 + (\Delta\eta)^2}$ around the electron to the energy of the electron must be smaller then 0.1.
- No Conversions
  High energy photons interacting with material in the detector can convert into electron-positron pairs. Electrons from conversions are backgrounds

to our electron selection. High energy conversions appear as oppositely charged tracks traveling in the same direction and having a pair mass of zero. An electron identified with a conversion partner is rejected.

A.2 Muon Identification

A high momentum muon detected at the trigger level is used as a source for a possible $t\bar{t}$ lepton plus jets event. Muons are identified as tracks in the COT matched to stubs in the muon chambers.

A.2.1 CMUP Triggers

Level 1

- A muon stub in the CMU detector with $P_t \geq 6.0$ GeV.
- Track with $P_t \geq 4$ GeV in the COT extrapolates to the muon stub.
- An additional stub required in the CMP detector.

Level 2

- COT track with $P_t \geq 8$ GeV

Level 3

- Tracks in the COT are extrapolated to stubs in both the inner CMU and outer CMP
- COT track with $P_t \geq 18$ GeV

A.2.2 CMX Triggers

Level 1

- A muon stub in the CMX detector with $P_t \geq 6.0$ GeV
- $P_t \geq 8$ GeV COT track with hits in at least four superlayers

Level 2

- No Level 2 Trigger Selections

Level 3

- COT track extrapolates to CMX stub
- COT Track with $P_t \geq 18$ GeV

A.2.3 Offline Selection

- $P_t \geq 20$ GeV
  Muons originating from W-bosons are expected to have large momentum.
- E_{EM} <Maximum of 2.0 GeV or $2.0 + 0.0115 \cdot (p - 100.0)$ GeV
  Muons are minimum ionizing particles and therefore should leave little energy in the electromagnetic calorimeters. A linear correction term is added because the deposited energy increases slightly with the momentum of the muon.
- E_{HAD} <Maximum of 6.0 GeV or $6.0 + 0.0115 \cdot (p - 100.0)$ GeV
  Muons should leave little energy in the hadronic calorimeters as well, though slightly more energy then the EM calorimeters because of the increased amount of material.
- $\Delta x_{CMU} < 3.0$ cm
  For an event with CMU hits, the extrapolated COT track must be within a small window of the hits in the CMU chamber.
- $\Delta x_{CMP} < 5.0$ cm
  For an event with CMP hits, the extrapolated COT track must be within a small window of the hits in the CMP chamber.
- $\Delta x_{CMX} < 6.0$ cm
  For an event with CMX hits, the extrapolated COT track must be within a small window of the hits in the CMX chamber.
- $|d_0| < 0.02$ cm with hits in silicon
  The impact parameter, d_0, is the distance of closest approach from the track to the z-axis. This rejects cosmic rays and mis-reconstructed tracks that do not apparently originate from the primary vertex.
- $|d_0| < 0.2$ cm without any hits in silicon
  This requirement is made less stringent if the track cannot be matched to a corresponding one in silicon or if the silicon detector is not in operation.
- $Track|z_0| < 60$ cm
  z_0 is the z intercept of the muon track. This is done to guarantee the track originates from optimal regions in the COT.
- # COT Axial Segments ≥ 3 and # COT Stereo Segments ≥ 2
  This is a quality cut on the muon track found in the COT.
- COT exit radius < 140 cm (CMX Only)
  This is done for muons detected in the CMX chambers only. It imposes a requirement that the track from the muon left in the COT had passed

through a minimum number of COT layers before matching to the CMX chamber.

- Isolation $I_l < 0.1$
  As in the case of the electron, the "isolation" requirement examines the energy nearby the muon. Jets with muon "punch-through" or decays in flight are rejected by requiring that energy deposited in the calorimeters in a cone around the muon is small. The isolation of the muon is the ratio of the energy in a cone around the muon to the momentum of the muon.

$$I_l = \frac{\sum E_t^{\Delta R<0.4}}{P_t^{muon}}$$

- Cosmic Veto
  Cosmic rays detected by CDF are characterized by two back-to-back tracks separated with a $\Delta\phi$ very close to 180 degrees and timing of the hits such that the track appears to be going "backward in time" across half of the COT diameter. These characteristics can be flagged and such muons are rejected.

A.3 Jet Identification And Corrections

Partons produced in the $p\bar{p}$ collision will hadronize into a shower of neutral and charged particles. This shower of particles is referred to as a jet. The signature of a jet is multiple COT tracks from the charged particles and a large amount of energy deposited in a limited region in both hadronic and electromagnetic calorimeters. Jets are identified as isolated deposits of energy in the calorimeters. The energy and direction of the jets are found by associating energies deposited in neighboring calorimeter towers into a single calorimeter "cluster".

The clustering is performed around any tower with $E_t > 3.0$ GeV. For any such tower, the algorithm begins by adding the energy of all towers within a cone of some ΔR around the highest energy tower in the group. The center of the cluster is calculated as the energy weighted centroid of the tower coordinates. A re-clustering is then performed around this new center and then the process repeated until it converges. The energy of the jets used in this analysis is the sum of the energy in a cone $\Delta R < 0.4$ around the center. Once a tower is included inside a clustered jet, it is no longer allowed to be included in the clustering of any other jet.

Several corrections to calculated jet energies account for known issues with the calorimeter response and other sources of deposited energy. Corrections are applied to jets in "levels", each of which is described below.

- Level 1 (η Dependence): Applied to the raw energy deposited in the calorimeter to correct for differences in calorimeter response as a function of η.
- Level 2 and 3 are no longer in use.
- Level 4 (Multiple Interactions): Energy from an overlapping $p\bar{p}$ interaction during the same bunch crossing will be detected inside jet clusters, increasing the energy of the measured jet. This correction subtracts that contribution on average.
- Level 5 (Absolute): Corrects the jet energy measured in the calorimeter for any non-linearity and energy loss in the un-instrumented regions of each calorimeter.
- Level 6 (Underlying Event): The underlying event is defined as the energy associated with the spectator partons in a hard collision event. These are the partons that do not contribute to the hard scattering, but whose peripheral interaction produces low energy particles in the event. Depending on the details of the particular analysis, this energy needs to be subtracted from the particle-level jet energy.
- Level 7 (Out Of Cone): The choice of $\Delta R < 0.4$ for clustering is arbitrary. Some of the jet energy will be outside of this cone. This correction uses Monte Carlo models of jets to correct for the out-of-cone energy, taking the jet energy back to the parent parton energy.

For this analysis, all jets are corrected to level 4 for selection purposes and to level 5 for all other purposes.

For the purpose of $t\bar{t}$ identification, we classify valid jets into one of two categories: "tight" and "loose". Any jet with level 4 corrected $E_t \geq 15.0$ GeV and $|\eta| < 2.0$ is a tight jet, and any jet with level 4 corrected $E_t \geq 8.0$ GeV and $|\eta| < 2.0$ is considered a loose jet. Note that tight jets are a subset of loose jets.

A.4 Missing Transverse Energy $\not\!\!E_T$

At the Tevatron, the protons and antiprotons in the beam have zero transverse momentum and therefore, the four-vector sum of the transverse energy

in the detector should be zero. In a lepton plus jets event, a large amount of momentum is carried away by the undetected neutrino. This produces a transverse momentum imbalance in the detector, which is called missing transverse energy ($\not\!\!E_T$), and it is closely related to the neutrino transverse momentum.

The calculation of $\not\!\!E_T$ begins as the negative of the vector sum of the raw (uncorrected) transverse energy in the calorimeter towers broken into x,y components.

$$\not\!\!E_{T,x}^{raw} = -\sum_{towers} E^{tower} \cdot \cos(\phi_{tower})$$

$$\not\!\!E_{T,y}^{raw} = -\sum_{towers} E^{tower} \cdot \sin(\phi_{tower})$$

In the case that the event contains a muon, which leaves minimal energy in the calorimeter, the sum is corrected by subtracting the associated calorimeter energy and adding the muon track momentum (for events without a muon, this step is skipped).

$$\not\!\!E_{T,x}^{muon-corr} = \not\!\!E_{T,x}^{raw} - P_t^{muon} \cdot \cos(\phi_{muon})$$

$$\not\!\!E_{T,y}^{muon-corr} = \not\!\!E_{T,y}^{raw} - P_t^{muon} \cdot \sin(\phi_{muon})$$

Finally the effect of the jet corrections is incorporated by removing the raw jets and adding the corrected jets to the sum.

$$\not\!\!E_{T,x}^{L4-corr} = \not\!\!E_{T,x}^{muon-corr} + \sum_{loose\ jets} E_{raw}^{jet} \cdot \cos(\phi_{jet}) - \sum_{loose\ jets} E_{L4Corrected}^{jet} \cdot \cos(\phi_{jet})$$

$$\not\!\!E_{T,y}^{L4-corr} = \not\!\!E_{T,y}^{muon-corr} + \sum_{loose\ jets} E_{raw}^{jet} \cdot \sin(\phi_{jet}) - \sum_{loose\ jets} E_{L4Corrected}^{jet} \cdot \sin(\phi_{jet})$$

The final corrected $\not\!\!E_T$ vector has magnitude equal to the quadrature sum of the x-y components and angular direction calculated from the x-y components.

$$\not\!\!E_T = \sqrt{(\not\!\!E_{T,x}^{L4-corr})^2 + (\not\!\!E_{T,y}^{L4-corr})^2}$$

$$\phi_{\not\!\!E_T} = Tan^{-1}(\not\!\!E_{T,y}^{L4-corr} / \not\!\!E_{T,x}^{L4-corr})$$

A.5 Secondary Vertex b-Tagging

Because top quarks decay to Wb and most background processes to $t\bar{t}$ do not contain heavy flavor quarks in the final state, requiring a b-quark to be present in our event is a good cut for improving the signal-to-background ratio. The bottom quark is long lived, and the typical b from top decay, with $p = 65$ GeV, travels a distance $\gamma\beta c\tau = \sim 500$ μm. This can be observed in the silicon detector as tracks within a jet forming a secondary vertex that is displaced from the primary vertex. An algorithm, called SecVtx, identifies events displaced secondary vertices in jets, and these vertices are used in selection to reduce background processes [23]. A jet identified with a secondary vertex by SecVtx is said to be "b-tagged".

Tagging is performed for each jet in an event by selecting quality tracks inside the jet and searching for vertices formed by those tracks. The quality of a track is determined by the number of hits in silicon tracking, the χ^2 of the track, and the momentum of the track. Good tracks with a large impact parameter are tested to see if they form a common vertex. For each vertex found, the length of the vector pointing from the primary vertex to the secondary vertex in the $r-\phi$ plane (L_{xy}), is calculated along with its error ($\sigma_{L_{xy}}$). If $L_{xy}/\sigma_{L_{xy}} > 3.0$ the jet is "tagged".

A.6 Dilepton Veto

To separate the $t\bar{t}$ lepton plus jets channel from the dilepton channel, any event with a second tight lepton is removed.

A.7 Z veto

Events are removed if a tight lepton and a second object form an invariant mass consistent with a Z-boson ($76 < M_{ll} < 106$ GeV). If the tight lepton is an electron, the second object must be an isolated electromagnetic object, a re-clustered jet with 95% of energy deposited in the electromagnetic calorimeter, or an opposite-signed isolated track. If the tight lepton is a muon, the second object must be an isolated muon or an opposite-signed isolated track.

A.8 Primary Vertex Reconstruction

The origin of the event is the primary vertex. The z-position of the primary vertex is used to cluster jets and to ensure that leptons and jets belong to the

same interaction. The z-position of the primary vertex is estimated by the error weighted average of the z-intercept of all tracks within a common point of origin.

$$z_{PrimVertex} = \frac{\sum_{tracks} z_0^{track}/\Delta_{track}^2}{\sum 1/\Delta_{track}^2}$$

To ensure the lepton originates from the primary vertex events are rejected if the lepton z-intercept is not within 5 cm of the primary vertex z-position. This reduces the number of events in the sample where jets and the lepton are part of different interactions.

Bibliography

[1] T. Aaltonen *et al.*, CDF Collaboration, "Measurement of the Forward-Backward Asymmetry in $t\bar{t}$ Production in 3.2 fb^{-1} of Tevatron Data", CDF-9724, Mar. 2009.
http://www-cdf.fnal.gov/physics/new/top/2009/tprop/Afb/
http://www-cdf.fnal.gov/physics/new/top/2009/tprop/Afb/cdfnote_9724_public_v01.pdf

[2] T. Aaltonen *et al.*, CDF Collaboration, "Forward-Backward Asymmetry in Top-Quark Production in $p\bar{p}$ Collisions at $\sqrt{s}$=1.96 TeV", Phys. Rev. Lett. 101, 202001 (2008).

[3] T. Aaltonen *et al.*, CDF Collaboration, "Measurement of the Charge Asymmetry in Top Pair Production using 1.9 fb^{-1}", CDF-9156, Jan. 2008.
http://www-cdf.fnal.gov/physics/new/top/2007/topProp/KA_Afb/
http://www-cdf.fnal.gov/physics/new/top/2007/topProp/KA_Afb/TopAsymmetry_1_9fb_public.pdf
http://www-cdf.fnal.gov/physics/new/top/2007/topProp/KA_Afb/TopAsymmetry_1_9fb_public.ps

[4] T. Aaltonen *et al.*, CDF Collaboration, "Measurement Of The Front Back Asymmetry In Top-Antitop Quark Pairs In 1.9 fb^{-1}", CDF-9169, Jan. 2008.
http://www-cdf.fnal.gov/physics/new/top/2007/topProp/Afb/
http://www-cdf.fnal.gov/physics/new/top/confNotes/cdf9169_cdf9169_topafb_19.pdf
http://arxiv.org/abs/0806.2472

[5] V. M. Abazov *et al.*, DØ Collaboration, "Measurement of the Forward-Backward Charge Asymmetry in Top-Quark Pair Production", Phys. Rev. Lett. 100, 142002 (2008).

[6] V. M. Abazov *et al.*, DØ Collaboration, "Measurement of the forward-backward production asymmetry of t and $\bar{t}$ quarks in $p\bar{p} \to t\bar{t}$ events", DØ Note 6062-CONF, July 2010.

[7] O. Antunano, J. H. Kuhn, and G. Rodrigo, Phys. Rev. D 77, 014003 (2008).

[8] M. T. Bowen, S. Ellis, and D. Rainwater, Phys. Rev. D 73, 014008 (2006).

[9] S. Dittmaier, P. Uwer, and S. Weinzierl, Phys. Rev. Lett. 98, 262002 (2007).

[10] L. G. Almeida, G. Sterman, and W. Vogelsang, Phys. Rev. D 78, 014008 (2008).

[11] Paola Ferrario and Germán Rodrigo, Phys. Rev. D 80, 051701(R) (2009), hep-ph/0906.5541.

[12] Harald Fritzsch, *Elementary Particles : Building Blocks of Matter*, translated by Karin Heusch (World Scientific, Singapore, 2005).

[13] Andrew Pickering, *Constructing Quarks : a Sociological History of Particle Physics*, (Univ. of Chicago Press, Chicago, 1984).

[14] F. Abe *et al.*, CDF Collaboration, "Observation of Top Quark Production in $\bar{p}p$ Collisions with the Collider Detector at Fermilab", Phys. Rev. Lett. 74, 2626 (1995).

[15] S. W. Herb *et al.*, "Observation of a Dimuon Resonance at 9.5 GeV in 400-GeV Proton-Nucleus Collisions", Phys. Rev. Lett. 39, 252 (1977).

[16] K. Kodamaa *et al.*, DONUT Collaboration, "Observation of tau neutrino interactions", Physics Lett. B 504, 218 (2001).

[17] T. Aalton *et al.*, CDF Collaboration, "Observation of the Ω_b^- baryon and measurement of the properties of the Ξ_b^- and Ω_b^- baryons", Phys. Rev. D 80, 072003 (2009).

[18] T. Aalton *et al.*, CDF Collaboration, "First Observation of Electroweak Single Top Quark Production", Phys. Rev. Lett. 103, 092002 (2009).

[19] Tevatron Electroweak Working Group, CDF, D0 Collaborations, "Combination of CDF and D0 Results on the Mass of the Top Quark", arXiv:1007.3178v1 [hep-ex].

[20] M. L. Mangano, M. Moretti, F. Piccinini, R. Pittau, A. Polosa, "ALPGEN, a generator for hard multiparton processes in hadronic collisions", JHEP 0307:001 (2003), hep-ph/0206293.

[21] G. Mahlon and S. Parke, "Angular correlations in top quark pair production and decay at hadron colliders", Phys. Rev. D 53, 4886 (1996).

[22] J. M. Campbell, R. K. Ellis, Phys. Rev. D 62, 114012 (2000), hep-ph/0006304. `http://mcfm.fnal.gov/`

[23] T. Affolder *et al.*, Phys Rev D 64, 032002 (2001).

[24] J. Adelman *et al.*, "Method II For You", CDF-9185, May 2008. `http://www-cdf.fnal.gov/internal/physics/top/RunIITopProp/m2-4u/methodII.html`

[25] `http://www-cdf.fnal.gov/internal/physics/top/RunIITopProp/tools/fitter.html`

[26] Erik Brubaker *et al.*, "Updated Measurement of the Top Quark Mass in the Lepton+Jets Channel", CDF-6845, May 2004.

[27] A. Bridgeman, L. Cerrito *et al.*, "Study of Charge Asymmetry in W+jets", CDF-9323, May 2008.

[28] Y. C. Chen *et al.* "Final Report of the B-Tag Task Force", CDF-10069, Feb. 2010.

[29] T. Aaltonen *et al.*, CDF Collaboration, "Measurement of the Ratio $\sigma_{t\bar{t}}/\sigma_{Z_{l\gamma^*}\to ll}$ and Precise Extraction of the $t\bar{t}$ Cross Section", Phys. Rev. Lett. 105, 012001 (2010) `http://link.aps.org/doi/10.1103/PhysRevLett.105.012001` `http://prl.aps.org/abstract/PRL/v105/i1/e012001`